THE INTERACTION BETWEEN LIGHT HEAVY-IONS AND WHAT IT TELLS US

M.E. BRANDAN[a], G.R. SATCHLER[b,c]

[a] *Instituto de Física, Universidad Nacional Autónoma de México, A.P. 20-364, México 01000 DF, Mexico*

[b] *Department of Physics & Astronomy, University of Tennessee, Knoxville, TN 37996, USA*

[c] *Physics Division, Oak Ridge National Laboratory, Oak Ridge, TN 37831-6373, USA*

ELSEVIER

AMSTERDAM – LAUSANNE – NEW YORK – OXFORD – SHANNON – TOKYO

ELSEVIER

Physics Reports 285 (1997) 143–243

PHYSICS REPORTS

The interaction between light heavy-ions and what it tells us

M.E. Brandan[a], G.R. Satchler[b,c]

[a] *Instituto de Física, Universidad Nacional Autónoma de México, A.P. 20-364, México 01000 DF, Mexico*
[b] *Department of Physics & Astronomy, University of Tennessee, Knoxville, TN 37996, USA*
[c] *Physics Division, Oak Ridge National Laboratory, Oak Ridge, TN 37831-6373, USA*

Received October 1996; editor. G.E. Brown

Contents

PII S0370-1573(96)00048-8

Abstract

Significant progress has been achieved during the last decade in our knowledge and understanding of the optical potential between two light heavy-ions. This has mostly been a consequence of the measurement of accurate and extensive elastic differential cross sections. Some of these data, covering over eight orders of magnitude in cross section, extend to sufficiently large scattering angles that they show remarkable refractive effects which remind one of features of the scattering of alpha particles by nuclei that have been known since the work of Goldberg some twenty years ago. Refractive effects, particularly nuclear rainbows, are evident in $^{12}C + ^{12}C$ and $^{16}O + ^{16}O$ angular distributions at bombarding energies between 6 and 100 MeV per nucleon. Their angular location and cross section have led to the determination of the gross features of the local optical potentials and in many cases have removed ambiguities in the depths of the real parts of the potentials. The resulting phenomenological potentials are strongly attractive ("deep"), with relatively weak absorption, and depend upon the bombarding energy. The optical model potential for such heavy-ions is no longer simply a way to parameterize scattering data (or perhaps just one of many ways). Ambiguities have been resolved, and a good understanding of the theoretical basis of its features has been attained. The folding model is central to this understanding, coupled with increased insight into the nature of realistic effective nucleon–nucleon interactions. This Report reviews the experimental evidence, its interpretation, and what we have learnt from it. Much of the interpretation becomes especially transparent when couched in the language of semiclassical scattering theory. We summarize this language, as well as the basic features of the theory of the optical model.

PACS: 25.70.Bc; 24.10.Ht; 21.65.tf; 25.60.Bx

Keywords: Elastic scattering; Heavy ions; Interaction potentials; Absorption; Nuclear equation of state; Rainbows

1. Introduction

Elastic scattering is the simplest nuclear reaction between a projectile and a target that can be induced by a hadronic interaction. Yet, despite this simplicity, elastic scattering has been an important source of information on nuclear properties. This information has been gleaned primarily through studies of the potential of interaction ("optical potential") that is found to reproduce measurements of the elastic scattering cross sections.

Usually, the first step in the description of the collision of two nuclei is the introduction of a simple one-body potential (*mean field* or optical potential) that describes some average features of the collision, namely, the elastic scattering and the gross *absorption* of the incident flux into other, nonelastic channels (the *reaction cross section*). This provides a basis upon which a more detailed description of the collision may be built. The distorted waves Born approximation (DWBA) approach to nonelastic transitions, which treats them as perturbations on the elastic scattering, is a well-known example, as is the coupled-channels (CC) approach to more strongly coupled reactions where feedback on the elastic channel needs to be considered explicitly [182]. Another example is that almost all models of the *fusion* of two nuclei into a compound system introduce an interaction potential which, together with the repulsive Coulomb field, provides a potential barrier which must be at least partially penetrated [187]. In these various ways elastic scattering is treated as a doorway through which the system must go before other processes are manifest. Nucleus–nucleus potentials play important roles in other phenomena also, such as *quasi-molecular resonances* [86, 92, 115].

As it is common with other complicated many-body problems, it is seldom possible to construct such potentials from first principles, so we proceed by introducing models which become more sophisticated and more microscopic as our understanding advances. Naturally, we try to incorporate into such model potentials as much of the known physics as is possible. This includes choosing them to reflect the overall sizes of the colliding nuclei, and making them complex so that they accommodate the loss of flux (absorption) into other, nonelastic channels. A very convenient way of incorporating (and identifying) gross nuclear properties is through the use of the *folding models* discussed below. In this approach the potential is generated by folding an effective nucleon–nucleon interaction over the ground-state density distributions of the two nuclei [181, 182]. In addition, there are complex contributions to the potential, sometimes referred to as constituting the *dynamical polarization potential* (DPP), which arise from the couplings to the nonelastic channels, both open and closed. In particular, the open channels furnish the absorptive, imaginary part of the potential, while both can contribute to the real part. Virtual excitations to the closed channels are an important source of the *threshold anomaly* [187].

The theoretical understanding of the general properties and microscopic basis of the optical potential for nucleon–nucleus scattering has advanced considerably in recent years [136, 138, 45]. No truly microscopic theory of the mean field for nucleus–nucleus collisions is available. Rather, one usually appeals to the coupled reaction channels theory of Feshbach [68]. Despite difficulties with antisymmetrization under exchange of nucleons between the two nuclei, this approach often facilitates transparent physical interpretations.

The theoretical understanding of phenomena encountered in measurements of elastic scattering has also developed considerably over the last two decades. This understanding is often phrased in semiclassical language so that we encounter terms like *refractive* and *diffractive*, or *rainbows* and

nearside, farside scattering [88]. Such an approach plays an important role in the work we report here, and has enabled us to clarify questions about the optical potentials such as "Are they deep or shallow?", or "Are they strongly or weakly absorbent?"

In this paper we review the progress made in understanding the elastic scattering of heavy-ions, especially of light heavy-ion systems such as $^{12}C+^{12}C$, $^{12}C+^{16}O$ and $^{16}O+^{16}O$, and what this has revealed about general nuclear properties. Much of this understanding has been obtained by building upon the concepts introduced [76] to elucidate the scattering of the alpha particle (which, despite the official definition, might be regarded as the lightest of the heavy-ions!). While a review of this nature involves a large number of references, we have not tried to make the list exhaustive but rather aimed to present papers and reviews which themselves behave as guides to further reading if it is desired.

2. Why *light* heavy-ions?

2.1. Strong absorption

In a general sense, collisions between two complex nuclei are associated with strong absorption; i.e., intimate contact almost inevitably leads to nonelastic events and loss from the elastic channel. Consequently, the scattering is dominated by conditions at the surface and this information is carried by systems traveling on peripheral trajectories. Here, "surface" means the region where the nuclear forces begin to act strongly. The location of this region can be represented by a *strong absorption radius*, R_{SA}, defined in various but similar ways. One such is to identify it with the apsidal distance on a Rutherford orbit with the same angular momentum as that for which the optical model transmission coefficient is one-half.

The values of R_{SA} that are found in practice can be parameterized as

$$R_{SA} = r_0(A_1^{1/3} + A_2^{1/3}) + \Delta\,, \tag{2.1}$$

where R_{SA} is the distance between the centres of two nuclei with mass numbers A_1 and A_2. Since $r_0 \approx 1.1$ fm, the first term represents the sum of the radii of the density distributions of the two nuclei and the second term Δ is the separation of their surfaces. Values of Δ between 2 and 3 fm are typical separations at bombarding energies with $E/A \approx 10$–20 MeV; see Fig. 2.1 for an example. The radius R_{SA}, and hence the separation Δ, decreases slowly as the energy increases [176, 177]; Δ has reduced to between 1 and 2 fm by $E/A = 100$ MeV.

Thus strong absorption has become established before there is any substantial overlap of the two nuclear matter distributions (Fig. 2.1). This apparently paradoxical statement is possible because the nucleon–nucleon forces have a finite range which bridges the gap between the two ions. The interaction potential between the two nuclei at $r = R_{SA}$, obtained for example by folding the nucleon–nucleon interaction over the two matter distributions, receives contributions from the whole surface region of both nuclei [181]. Nonetheless, the presence of the strong absorption makes it difficult or impossible to gain any knowledge of the potential at closer distances where the nuclei do begin to overlap appreciably. It is well known that under these circumstances about all we can hope to learn from elastic measurements is the (complex) value of the potential in the vicinity of R_{SA} and perhaps

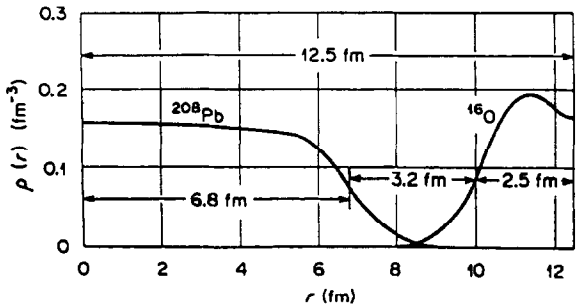

Fig. 2.1. The density distributions of the nuclei ^{16}O and ^{208}Pb when their centres are separated by the strong absorption radius appropriate for scattering at energies between about 100 and 200 MeV (from [181]).

some information about its slope [182]. This is the situation pertaining to much of heavy-ion elastic scattering, especially that involving medium to heavy nuclei.

The magnitudes of the partial-wave S-matrix elements, $|S_l|$, provide a measure of the degree of absorption. Of course, $|S_l| = 1$ for large l, but it decreases rapidly for l around the value l_g for grazing trajectories. When we approach, say, $|S_l| \leq 10^{-4}$ for small $l < l_g$, we are justified in speaking of "strong absorption". Then the transmission coefficient $T_l = 1 - |S_l|^2$ is unity, representing complete absorption, to within one part in 10^8.

2.2. *"Incomplete" absorption*

Fortunately, one does not require much penetration into the inner regions (small $l < l_g$) of the potential in order to see some signal of the conditions there, provided one is prepared to measure very small cross sections. A scattered amplitude from this region of a few per cent or less is sufficient to carry this signal to large scattering angles, although in other respects this would still represent strong absorption. For example, a partial-wave S-matrix element with magnitude $|S_l| = 0.03$ corresponds to a transmission coefficient $T_l = 0.999$, or a departure from total absorption of this partial wave of only one-tenth of one percent. Yet this can be enough to produce recognizable rainbow phenomena.

The possibility of seeing such refractive effects was first realized in the scattering of alpha particles [76]; a more recent example is illustrated in Fig. 2.2. A few years later hints were emerging that similar, but weaker, effects were being seen in the scattering of the light heavy-ions ^{6}Li [58, 192] and ^{12}C [17, 23, 41]. By now, many examples of refractive phenomena in light heavy-ion systems have been collected, culminating in the most spectacular example of an Airy pattern exhibited in ^{16}O + ^{16}O scattering at $E = 350$ MeV [198] shown in Fig. 2.3.

As our experience with heavy-ion scattering has broadened, it has become clear that the conditions, especially the degree of absorption present, that will allow these refractive effects to be seen are met by some light systems but are not satisfied by heavy systems. That is the short answer to the question posed in the title to this section.

Before exploring these questions further and examining actual experimental results, we summarize briefly the semiclassical concepts that provide considerable insights into the phenomena seen in potential scattering and act as unifying principles. Next we turn to the theoretical basis of the

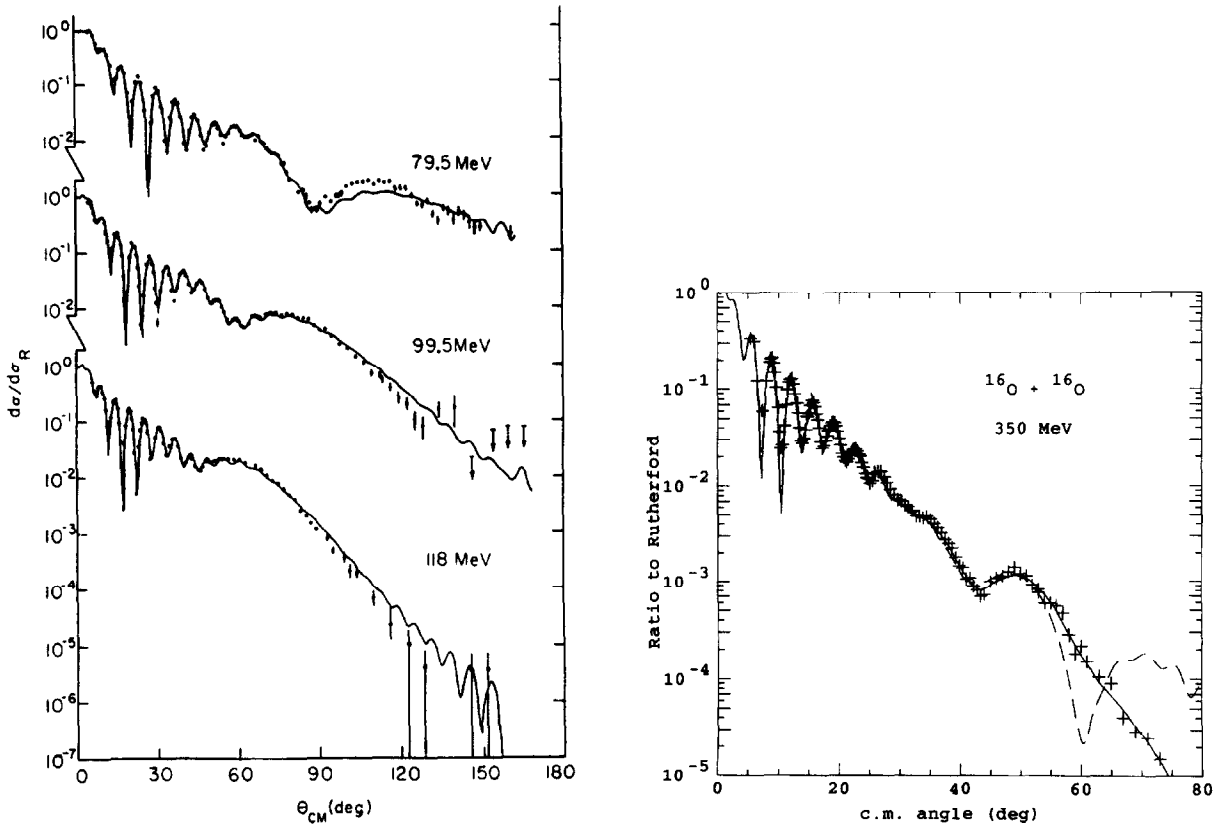

Fig. 2.2. Refractive effects in the scattering of α-particles by ^{90}Zr nuclei at several energies (from [167]).

Fig. 2.3. Striking Airy pattern exhibited in the angular distribution of the elastic scattering of ^{16}O by ^{16}O at a bombarding energy of 350 MeV [198, 199]. The solid line represents an optical potential fit [33] which indicates that the minimum near 40° is the first Airy minimum forward of the primary rainbow. The dashed line is the result of an attempted fit with a deeper potential which would interpret that dip as the *second* Airy minimum. It would also predict the first to be near 60°, where none is observed.

optical model potential so as to better understand the origin of the properties we infer from the measurements.

3. Semiclassical interpretation of potential scattering: A brief summary

3.1. Classical trajectories

The wavelengths associated with heavy-ion scattering are usually short enough, and consequently the number of partial waves involved is sufficiently large, that use of the language of semiclassical trajectories becomes meaningful and very useful for understanding the characteristics of the scattering. The presence of absorption plays a very important role in determining the outcome of the collision

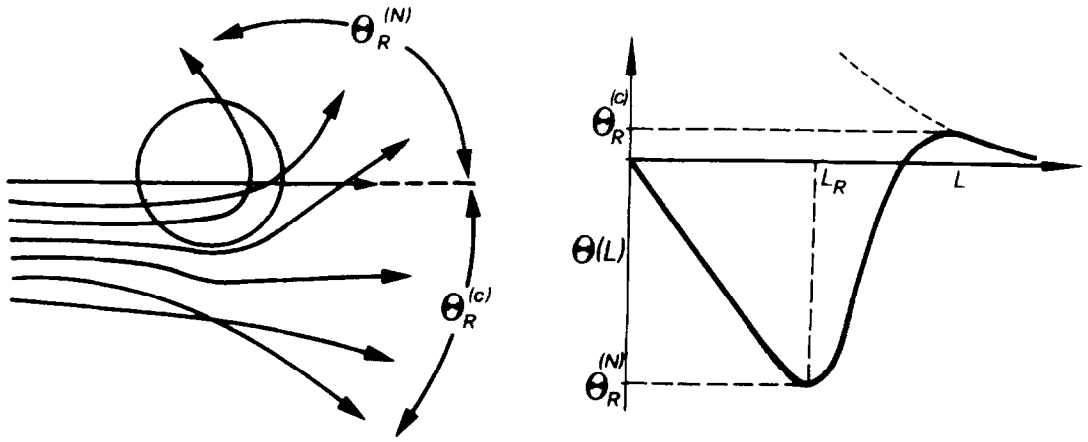

Fig. 3.1. Left: classical trajectories that lead to Coulomb (C) and nuclear (N) rainbows. Right: the corresponding deflection function (from [184]).

but in practice does not destroy the underlying trajectory picture. Qualitatively, absorption can be thought of as simply damping the flux as the system traverses the classical path. This approach is discussed elsewhere in more detail [88, 143], while a more sophisticated treatment fully accounts for the complex nature of the potential from the outset [108, 107].

Fig. 3.1 illustrates some typical trajectories for scattering from an attractive, real hadronic potential plus a repulsive Coulomb potential. The scattering angle as a function of impact parameter b, or angular momentum $(l+\frac{1}{2})\hbar = kb$, is called the *deflection function* $\Theta(l)$ and is shown on the right of Fig. 3.1. Trajectories with positive Θ, in this case the peripheral ones that are dominated by the Coulomb repulsion, constitute nearside scattering, while those drawn to negative Θ by the attractive nuclear potential represent farside scattering.

3.2. Nearside and farside scattering

The significance of the terms nearside and farside is perhaps more obvious if one looks at the trajectories that can contribute to a given scattering angle, as indicated in Fig. 3.2. (The inset to the right is to remind us that these trajectories are classical constructs and are attended by wave diffraction in a quantal treatment.) The quantal scattering amplitude $f(\theta)$ can always be decomposed into two parts by using the partial-wave expansion [182]

$$f(\theta) = (2ik)^{-1}\sum_l (2l+1)a_l P_l(\cos\theta)\,, \tag{3.1}$$

where the partial wave amplitude is

$$a_l = e^{2i\sigma_l}(S_l - 1)\,. \tag{3.2}$$

Here S_l is the elastic partial wave S-matrix element and σ_l the Coulomb phase. We may then express the standing wave Legendre function $P_l(\cos\theta)$ as a sum of travelling waves running in

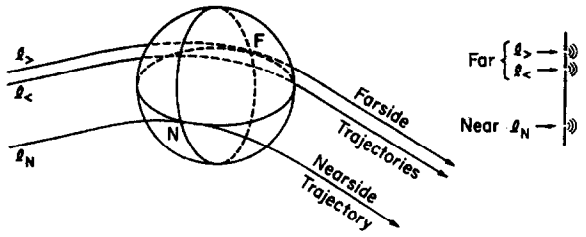

Fig. 3.2. Schematic representation of three semiclassical trajectories that result in the same scattering angle. The right-hand section suggests how the resulting angular distribution is analogous to a three-slit interference pattern.

opposite directions around the scattering centre [74],

$$P_l(\cos\theta) = \tilde{Q}_l^{(+)}(\cos\theta) + \tilde{Q}_l^{(-)}(\cos\theta)\,, \tag{3.3}$$

where

$$\tilde{Q}_l^{(\pm)}(\cos\theta) = \frac{1}{2}\left[P_l(\cos\theta) \mp \mathrm{i}\frac{2}{\pi}Q_l(\cos\theta)\right], \tag{3.4}$$

and Q_l is the Legendre function of the second kind. For *large* l, the $\tilde{Q}_l^{(\pm)}$ behave like the travelling waves $\exp[\pm\mathrm{i}(l+\frac{1}{2})\theta]$. Then it is easy to see that the $(\pm)$ components of (3.3) represent scattered waves emanating from opposite sides of the scattering centre. Thus we have from (3.1)

$$f(\theta) = f_{\mathrm{N}}(\theta) + f_{\mathrm{F}}(\theta)\,, \tag{3.5}$$

where

$$\underset{\mathrm{F}}{f_{\mathrm{N}}}(\theta) = (2\mathrm{i}k)^{-1}\sum_l (2l+1)a_l\tilde{Q}_l^{(\mp)}(\cos\theta)\,. \tag{3.6}$$

The interpretation of a nearside–farside decomposition is especially transparent when there is strong absorption accompanied by an attractive real potential. Systems following the trajectories with small impact parameters are absorbed, but those on peripheral paths are affected by the attraction. These peripheral paths are associated with a window of angular momenta close to the grazing value $l = l_{\mathrm{g}}$. Each l-window, nearside and farside, produces a scattering amplitude with a single-slit diffraction pattern (see Fig. 3.3) and a magnitude that decreases exponentially as the scattering angle moves away from the classically allowed path. In many cases of physical interest, and for angles not too close to the grazing angle θ_{g}, these amplitudes may be written for $\theta > \theta_{\mathrm{g}}$ as [143, 88]

$$(\sin\theta)^{1/2}\underset{\mathrm{F}}{f_{\mathrm{N}}}(\theta) \sim \mathrm{e}^{\mp\mathrm{i}l_{\mathrm{g}}\theta}\mathrm{e}^{-\alpha_{\mathrm{N}}(\theta\mp\theta_{\mathrm{g}})}_{\mathrm{F}}\,. \tag{3.7}$$

The two patterns, $f_{\mathrm{N}}(\theta)$ and $f_{\mathrm{F}}(\theta)$, are similar but separated in angle by $2\theta_{\mathrm{g}}$, because of the Coulomb repulsion (Fig. 3.3). In the absence of a nuclear field, we have $\alpha_{\mathrm{N}} = \alpha_{\mathrm{F}}$. A short-ranged nuclear attraction at the surface enhances the waves diffracted from the farside and (for $\theta > \theta_{\mathrm{g}}$) reduces those from the nearside, so $\alpha_{\mathrm{N}} > \alpha_{\mathrm{F}}$. Consequently, while $f_{\mathrm{F}}(\theta) < f_{\mathrm{N}}(\theta)$ at small θ, there is a crossover angle $\bar{\theta}$ at which $f_{\mathrm{F}} = f_{\mathrm{N}}$ and beyond which the farside scattering dominates. This is illustrated in Fig. 3.4 which shows the individual cross sections $\sin\theta|\underset{\mathrm{F}}{f_{\mathrm{N}}}(\theta)|^2$, as well as their coherent sum.

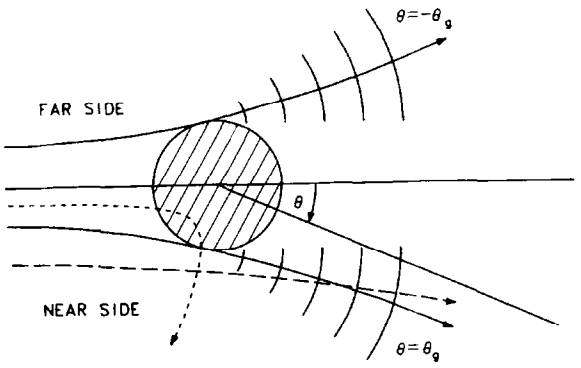

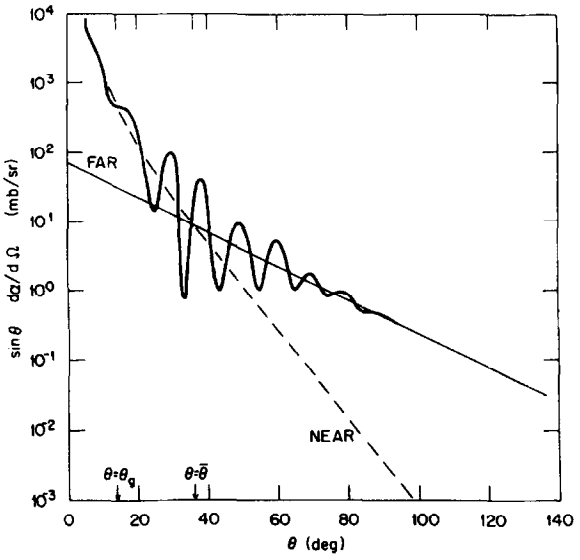

Fig. 3.3. Illustrating classical trajectories and waves diffracted from the near and far sides of a strongly absorbing region. The solid curves represent grazing trajectories which suffer diffraction at the edges of the "black" sphere. The long-dashed curve is a Rutherford trajectory for a larger impact parameter which suffers little diffraction. The short-dashed curve is a Rutherford trajectory for a small impact parameter, which in practice is strongly absorbed (from [143]).

Fig. 3.4. Example of the nearside/farside decomposition of the angular distribution (expressed as $\ln(d\sigma/d\theta)$) for scattering by a strongly absorbing sphere plus refraction at the surface (from [184]).

(The presence of the $(\sin\theta)^{1/2}$ factor in (3.7) often makes it more convenient to examine the cross section $d\sigma/d\theta = 2\pi \sin\theta \, d\sigma/d\Omega$, rather than the more usual $d\sigma/d\Omega$.) The farside–nearside interference pattern seen in Fig. 3.4 corresponds to Fraunhofer two-slit diffraction and is most pronounced near the crossover angle $\bar{\theta}$. It results from the phase factors in (3.7) so that the maxima are spaced by $\Delta\theta \approx \pi/l_g$. Beyond this interference pattern we are left with the farside exponential tail that is characteristic of farside dominance. When observed, the position of this, and any associated Airy structure (see below), allows one to place constraints on the strength of the real potential in the surface at distances somewhat inside the strong absorption radius.

3.3. *More general decompositions*

The decomposition (3.3) and (3.4) has been used to generate the nearside–farside decompositions shown in this paper. Although this is mathematically exact, the physical interpretation in terms of travelling waves is unambiguous only for large l, that is for peripheral collisions. A more general semiclassical technique for scattering from complex potentials has been introduced [73], based upon the work of [108, 107] (see also [25]). We quote from [73]: "Long usage has conferred an aura of 'physical reality' on the rays of geometrical optics, and it is this accumulated experience with the way rays describe wave propagation that provides the 'physical interpretation' of the analogous decomposition of $f(\theta)$ into its 'semiclassical trajectory' components

$$f(\theta) = f_1(\theta) + f_2(\theta) + \cdots." \tag{3.8}$$

This applies particularly to decomposing the farside amplitude itself into semiclassical subamplitudes, such as those associated with the *two* farside trajectories shown in Fig. 3.2. These two, in particular, play an essential role in our analysis of rainbow phenomena. The farside trajectory with the larger impact parameter is the one discussed earlier and represented by the amplitude $f_F(\theta)$ in Eq. (3.5). When the absorption at smaller radii is not complete, systems following another trajectory with a smaller impact parameter may survive, emerging at the same scattering angle and interfering with the first one. This is the origin of rainbow phenomena and is most simply discussed at our present level in terms of the deflection function.

3.4. Deflection functions

The deflection function for scattering by a real potential is related to the real scattering phase shifts δ_l in the WKB approximation by

$$\Theta(l) = 2d\delta_l/\mathrm{d}l\,, \tag{3.9}$$

where the elastic scattering S-matrix element is

$$S_l = \mathrm{e}^{2\mathrm{i}\delta_l}. \tag{3.10}$$

In practice, the potentials that we shall encounter are complex and the corresponding phase shifts become complex. One may then consider the deflection function for scattering by the real part of the potential alone. Alternatively, we may use in Eq. (3.9) just the real part of the phase shift by writing

$$S_l = |S_l|\mathrm{e}^{2\mathrm{i}\delta_l}, \tag{3.11}$$

where $|S_l| \leq 1$. There is no strict justification for either procedure but fortunately examination of realistic cases of light heavy-ion scattering shows that the two approaches frequently give very similar results. This supports our assumption that the spatial motion of these systems is primarily determined by the real potential while the imaginary potential primarily reduces the flux as it travels along these paths, and hence reduces the magnitude of the outgoing scattering amplitude. (This view also underlies the semiclassical treatments of [32].)

The structure of the typical deflection function shown in Figs. 3.1 and 3.5 can be easily understood. The positive segment for large l (large impact parameters) is due to the repulsive Coulomb field. We may write Θ as a sum of nuclear and Coulomb components

$$\Theta(l) = \Theta^{\mathrm{N}}(l) + \Theta^{\mathrm{C}}(l)\,, \tag{3.12}$$

where

$$\Theta^{\mathrm{C}}(l) = 2\arctan\left(\eta/l + \tfrac{1}{2}\right), \tag{3.13}$$

and η is the Sommerfeld parameter for a relative velocity v

$$\eta = Z_1 Z_2 e^2/\hbar v\,. \tag{3.14}$$

The positive angle (nearside) segment is relatively small because the repulsive Coulomb interaction is weak for the light systems of interest here. As the impact parameter decreases, the attractive

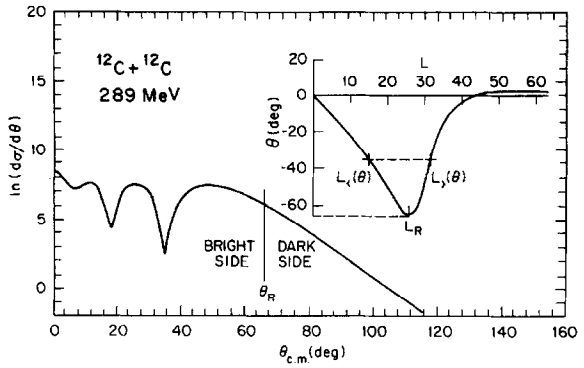

Fig. 3.5. Deflection function and farside differential cross section for (unsymmetrized) $^{12}C + ^{12}C$ scattering at 289 MeV, calculated using a potential that reproduces the observed scattering for this system. The nuclear rainbow occurs at $\Theta_R = -66°$ with $L_R \simeq 26$. The Airy maxima and minima on the bright side result from interference between the $L_>$ and $L_<$ contributions (from [143]).

nuclear potential, which empirically is found to be quite deep (for example, ~ 200 MeV for the case shown in Fig. 3.5, so that the attractive *force* is $\sim$ a few tens of MeV/fm), overwhelms the Coulomb repulsion ($\sim$few MeV/fm) and induces farside scattering to negative angles. However, the magnitude of the negative angle cannot increase without limit, provided the energy is above the range that allows orbiting. An extremum is reached and then Θ decreases to zero for head-on collisions.

3.5. Rainbows

Classically, the differential cross section at the scattering angle $\theta = |\Theta|$ is given by

$$\frac{d\sigma}{d\Omega}(\theta) = \sum \frac{(l + 1/2)\hbar^2}{k^2 \sin\theta |d\Theta/dl|} . \tag{3.15}$$

where the sum allows for the possibility that more than one l value results in the same scattering angle θ. This expression diverges whenever $d\Theta/dl = 0$. This is called a rainbow, since the corresponding phenomenon in the scattering of light from water droplets is responsible for atmospheric rainbows. The deflection functions of Figs. 3.1 and 3.5 show two such extrema. The outer, for large l, results in a *Coulomb rainbow*, seen at small scattering angles. (The name is a little misleading because the outer maximum in Θ results from a balance of Coulomb *and* nuclear forces.) The inner minimum in Θ gives rise to a nuclear rainbow at $\theta = |\Theta_R|$.

3.6. Supernumerary rainbows and the Airy pattern

Of course, there is no longer a divergence at a rainbow angle in a quantal description, and the sum over cross sections in (3.15) becomes a coherent sum over amplitudes. The latter fact is vital for understanding the behaviour of the cross section at angles $\theta < |\Theta_R|$ where there are farside contributions from two angular momenta l at each angle θ, as indicated by the trajectories in Fig. 3.2. These are denoted $l_<(\theta)$ and $l_>(\theta)$ in Figs. 3.2 and 3.5, and their interference results in a

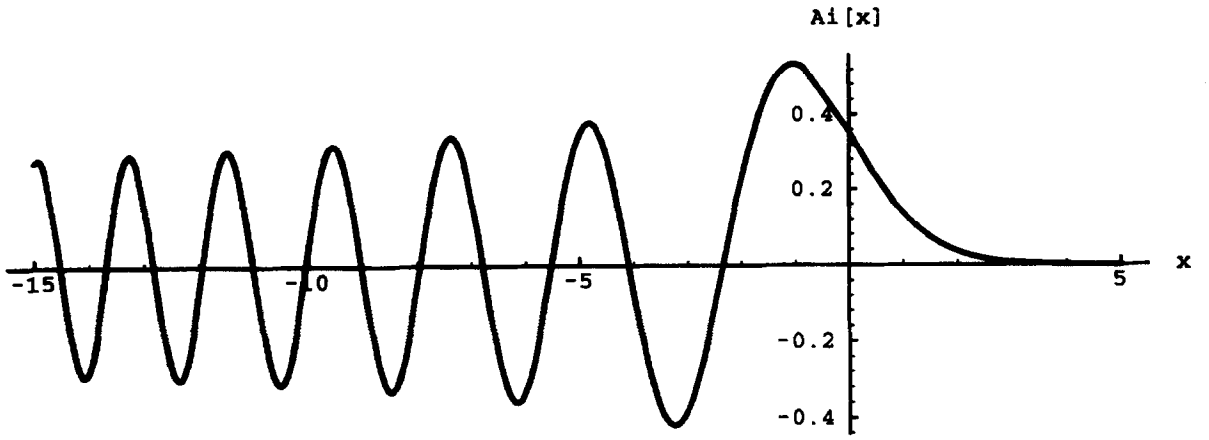

Fig. 3.6. Graph of the Airy integral $Ai(x)$. In our context, x is proportional to $\theta - |\Theta_R|$, so that $x=0$ corresponds to $\theta = |\Theta_R|$ and positive x is on the (classically forbidden) dark side of the rainbow.

series of maxima and minima in the farside cross section shown in Fig. 3.5. This has become known as an Airy pattern after the 19th century Astronomer Royal of England, Sir George Airy, who provided the first mathematical model of the atmospheric rainbow. By using a parabolic approximation for the minimum in the deflection function, he was able to express the scattering amplitude as the well-known Airy function $Ai(x)$ shown in Fig. 3.6. In our context, the argument x is proportional to $\theta - |\Theta_R|$: see [158] for example. Then $x=0$ represents the primary rainbow and $x>0$ corresponds to the classically forbidden darkside of the rainbow where the amplitude decreases exponentially with angle. The extrema for $x<0$ represent *supernumerary rainbows*, and it is their observation that gives the most unambiguous signal of rainbow phenomena; at least the first Airy minimum can be discerned clearly in the examples shown in Figs. 2.2 and 2.3. These Airy oscillations have widths $\delta\theta = \pi/(l_> - l_<)$, much broader than the widths of the nearside/farside oscillations at the more forward angles.

The imaginary part of the optical potential plays a very important role at this juncture in determining the relative magnitudes of the $l_<$ and $l_>$ contributions to the scattering amplitude, and thus how distinctive their interference pattern can be. The $l_<$ trajectories experience deeper penetration of the potential, and hence more absorption, than the $l_>$ ones; consequently, they interfere less effectively than if the potential were real. If the absorption along the $l_<$ trajectory is increased so that the interference with the $l_>$ amplitude becomes negligible, we are left with a featureless farside amplitude that falls off exponentially with increasing angle. Fig. 3.5 shows the cross section for farside scattering from the *real part alone* of an otherwise realistic $^{12}C + ^{12}C$ potential. We see a primary rainbow and two well-developed higher-order Airy maxima or supernumerary rainbows. On the other hand, Figs. 3.7 and 3.8 show examples of the scattering induced by *complex* potentials that are not unrealistic. Fig. 3.7 illustrates the nearside, farside decomposition for a potential (CC1) needed to fit measurements of $^{12}C + ^{12}C$ scattering at 159 MeV [29]. Despite the absorption present, a distinctive Airy minimum near 70°, the first preceding the primary rainbow near 120°, is clearly visible, and even a hint of the second one can be seen in the farside amplitude. By way of contrast, Fig. 3.8 shows the same case except that the absorptive potential at small radii has been

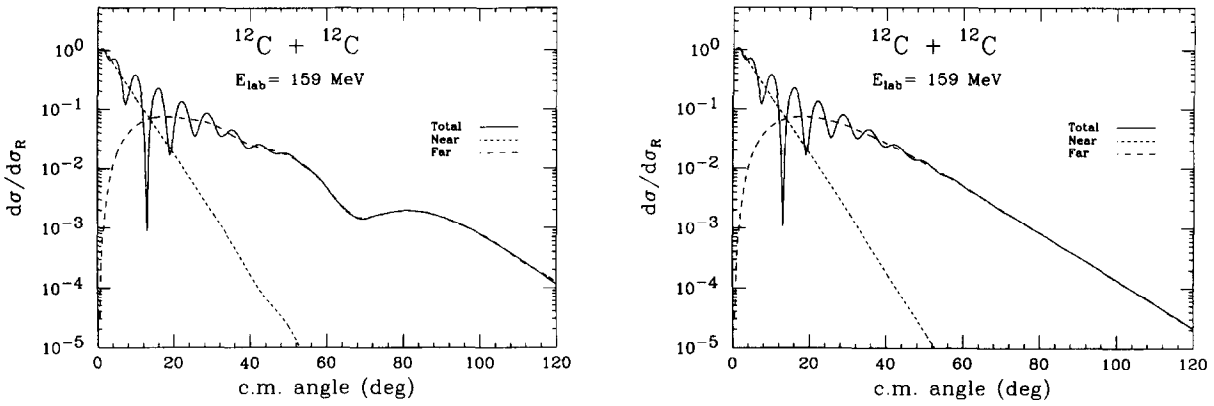

Fig. 3.7. Decomposition into nearside and farside contributions of the scattering by a complex potential (CC1) found to fit measurements of $^{12}C + {}^{12}C$ scattering at 159 MeV. The solid curve denotes the coherent sum of the two amplitudes. An Airy minimum in the farside scattering is seen near 70°, preceding the primary rainbow near 120°. (From [BR88c]. For clarity, the two ions have been treated as nonidentical.)

Fig. 3.8. As for Fig. 3.7, except that the absorptive potential has been artificially increased at small radii[a]. The Airy pattern in the farside contribution seen in Fig. 3.7 no longer appears because the additional absorption has dampened the $l_<$ part of the farside amplitude.

increased artificially.[1] Now the additional absorption has dampened the $l_<$ contribution so much that no perceptible Airy pattern remains in the farside amplitude, and the cross section exhibits a smooth exponential-like falloff at angles beyond the farside–nearside interference region. Although inappropriate for this particular case of $^{12}C + {}^{12}C$ at 159 MeV, such patterns have been observed for other systems or energies. ($^{12}C + {}^{16}O$ at 608 MeV is one such case, discussed in [29].) At one time this was regarded [58] as "characteristic of a nuclear rainbow", but in the light of our present understanding, we believe the term "rainbow" should be reserved for those cases where some remnant of the Airy pattern can be identified. A structureless exponential-like falloff might be better referred to simply as farside dominance or a farside tail.

It is instructive to compare in Fig. 3.9 the magnitudes $|S_l|$ of the S-matrix elements for the two cases shown in Figs. 3.7 and 3.8. (The plot of $|S_l|$ vs. l may be called the *absorption profile* for scattering by that potential.) The $|S_l|$ for $l \geq 23$ are almost identical for the two potentials, and as a consequence, the differential cross sections are almost exactly the same out to $\theta \approx 40°$. However, those for small l have been reduced by more than two orders of magnitude by the additional absorption. The angular momentum $l_<$ associated with the inner farside trajectory falls in this region, thus contributions from this trajectory have been essentially eliminated and no Airy interference is seen in Fig. 3.8. It is also worth noting that the original potential, which does reveal in Fig. 3.7 a pronounced first Airy minimum, does so with $|S_l|$ for small l that are only a few times 10^{-3}.

A more detailed analysis [29, 73] of the scattering shown in Fig. 3.7, as well as similar cases, will be discussed later.

[1] By adding to potential CC1 of [29] an imaginary term with a shape that is the derivative of the Woods–Saxon shape, strength $W_D = 80$ MeV, radius $R_D = 1.7$ fm and diffuseness $a_D = 0.5$ fm.

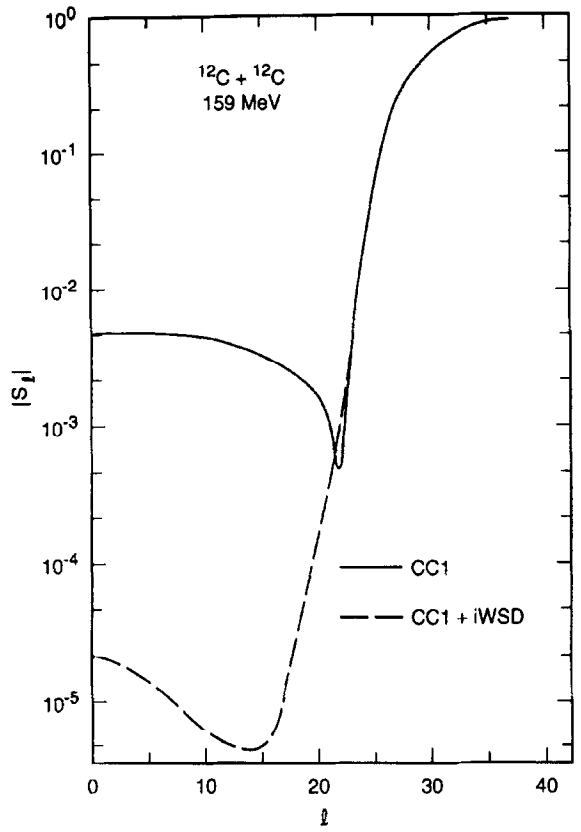

Fig. 3.9. The magnitudes of the S-matrix elements for the cases shown in Figs. 3.7 and 3.8, showing the very different degrees of absorption occurring for the partial waves with small impact parameters, although the grazing waves with $l \geq 23$ are almost identical.

4. Meaning and theoretical basis of the optical model potential

4.1. Optical model potential as an effective interaction

An optical model potential is an effective interaction $U_E(r)$ between two particles whose centres of mass are separated by the distance r, which can be used in a one-body Schrödinger equation

$$\left[-\frac{\hbar^2}{2\mu}\nabla^2 + U_E(r)\right]\chi(\boldsymbol{r}) = E\chi(\boldsymbol{r}) \tag{4.1}$$

such that the asymptotic behaviour of its solutions $\chi(\boldsymbol{r})$ (with appropriate boundary conditions) describe their elastic scattering, at least in an energy-averaged way. (We ignore any dependence on the spins of the particles for simplicity.) In Eq. (4.1), E is the energy of relative motion in the centre-of-mass system, while $\mu = M_p M_t/(M_p + M_t)$ is the reduced mass of the system when the projectile and target are well separated. The two nuclei remain in their ground states in this scenario. No attempt is made to describe explicitly any excitation or distortion of the nuclei during

the collision. Any effects due to such polarization are assumed to be taken into account by the characteristics of the potential U_E; in particular $U_E = V_E + iW_E$ has an imaginary part which describes the loss of flux (*absorption*) into nonelastic channels.

The availability of accurate data covering a wide range of angles for α-particle elastic scattering has made it possible to determine phenomenological optical potentials without discrete ambiguity for many target nuclei. We are approaching a similar situation for the scattering of light heavy-ion systems. The significance of this and the interpretation of the potentials is the main subject of the present review.

4.2. Energy dependence and nonlocality

The potential U_E is written in Eq. (4.1) as though it is local, although it may vary with the energy E. Model potentials are almost invariably assumed to be local, although, in principle, theoretically derived potentials are nonlocal,

$$U_E\chi(\boldsymbol{r}) = \int U_E(\boldsymbol{r},\boldsymbol{r}')\chi(\boldsymbol{r}')\,d\boldsymbol{r}' . \tag{4.2}$$

Consequently, it is customary to derive equivalent (but generally approximate) local forms in order to compare with more phenomenological local potentials obtained by analysis of measured elastic scattering. The energy dependence implied in Eq. (4.2) is *intrinsic* (which may be interpreted as a nonlocality in *time* [138–140]). A transformation of the spatial nonlocality (momentum dependence) to give an equivalent local potential results in an additional energy dependence. The two types of energy dependence cannot be distinguished in phenomenological potentials.

4.3. Microscopic theories of the optical potential

4.3.1. Introduction

Many ways of calculating a nucleus–nucleus optical potential have been proposed. Frequently a total energy curve is calculated as a function of the distance separating the centres of mass of the two nuclei. (Care has to be taken over the definition of this distance when the two nuclei overlap!) After subtraction of the energy of the two noninteracting nuclei, this energy curve is then interpreted as an optical potential and used in Eq. (4.1) to calculate the elastic scattering. This is incorrect. Such approaches attempt to follow explicitly, to a greater or lesser degree, the readjustments that the two nuclei make as they begin to interact and overlap: distortion of the nuclear shapes, reaction to the Pauli principle, effects due to the saturating nature of nuclear forces, etc. Such an interaction energy function does not determine just the relative motion while the nuclei remain in their ground states but is related to the motion of a wavepacket which can include a wide range of excited states of the individual nuclei. Such a wavepacket may be appropriate for describing the evolution of a process like fusion, but the ground-state component must be projected out asymptotically before it can describe elastic scattering. Even when the calculation is performed in an adiabatic approximation so that the system does return finally to the elastic channel, corrections to the kinetic energy term in Eq. (4.1) are required (see [150] for an early discussion).

A detailed criticism of the identification of the optical potential with such an energy curve has been presented by Horiuchi [84,86] (see also [69]), with particular emphasis on the inadequacy of

the adiabatic assumption. One practical point that has been stressed is that a "potential" of this kind has properties that conflict with those now known to hold for the real parts of phenomenological optical potentials that reproduce measured elastic scattering: namely that the interaction energy curves are shallow at low bombarding energy and become deeper as the bombarding energy increases and the repulsive effects of the Pauli principle decrease. Empirically, as documented in this review, the real parts of the optical potentials are found to be deep (several hundreds of MeV) and to become less deep as the incident energy increases.

The folding model, to be discussed in more detail in chapter 5, does result in real potentials that satisfy the empirical constraints. It can be regarded as a first approximation to the real part of the effective interaction which is derived within Feshbach's reaction formalism [68] (see Section 4.4) and which controls the relative motion of that part of the total wavefunction in which the two nuclei remain in their ground states. Thus it is appropriate for use in the optical model (Eq. (4.1)). Feshbach's theory also provides guidance as to the corrections to the folded potential that may be expected, and a framework within which they may be estimated.

4.3.2. Antisymmetrization, exchange and the resonating group method

Even if we use internal wavefunctions for the two nuclei, each of which is antisymmetric, the Pauli principle requires the total wavefunction also to be antisymmetric under the interchange of nucleons *between* the two nuclei. Some insight into the effects of this requirement is provided by the results of studies using the resonating group method (RGM) [39, 124, 125, 84, 86].

In its usual one-channel form, the RGM freezes the two nuclei in their ground states but takes full account of the exchange of nucleons between them. It uses the trial wavefunction

$$\mathscr{A}\{\chi(\boldsymbol{r})\phi_{p0}(\xi_p)\phi_{t0}(\xi_t)\}\,, \tag{4.3}$$

where ϕ_{p0} and ϕ_{t0} are the individually antisymmetrized internal ground-state wavefunctions for the projectile and target respectively, $\chi(\boldsymbol{r})$ is the wavefunction of relative motion and the antisymmetrizer $\mathscr{A}$ exchanges nucleons between them. A one-body wave equation for the relative motion function $\chi(\boldsymbol{r})$ is then constructed which includes a highly nonlocal RGM "potential". Besides a local direct term which is just a folded potential, the antisymmetrizer results in a hierarchy of nonlocal exchange terms, according to the number of nucleons exchanged. An accurate localization procedure has been devised which yields local potentials equivalent to these exchange terms [84, 86].

After localization, the RGM approach results in deep (real) potentials, comparable to the empirical ones, which become less deep as the bombarding energy increases and as the attractive exchange terms become weaker. These studies also indicate that the one-nucleon exchange contribution is the largest of the exchange terms, and dominates for peripheral collisions because it has the longest range. They also caution us that significant corrections may arise from the other terms at smaller distances, especially for near-symmetric systems ($A_p \approx A_t$). At the same time, it should be kept in mind that the RGM equation for $\chi(\boldsymbol{r})$ cannot immediately be identified with the optical model Schrödinger equation (4.1) (see [39] for a helpful discussion, also [69]), although the main conclusions reached about the RGM potential can be expected to be characteristic also of the optical model potential.

4.3.3. The absorptive, imaginary potential

The number of realistic attempts to calculate the imaginary (absorptive) part of the optical potential is quite limited. (But see [205], whose approach is based upon Feshbach's theory. Also, [32] consider

the imaginary potential for peripheral collisions using a semiclassical approach.) In practice, the imaginary potential is usually treated in a phenomenological way, either by multiplying the real folded potential by a complex strength or by assuming a form such as the Woods–Saxon one, and adjusting parameters to fit elastic data. The origin of the imaginary potential, and the associated contributions to the real part, is seen most transparently within the framework of Feshbach's reaction theory, to which we now turn.

4.4. Reaction theory of Feshbach

4.4.1. Introduction

There is no truly microscopic theory of the optical potential for the scattering of two composite nuclei in the sense that there is for nucleon–nucleus scattering [136, 137]. However, it is useful to appeal to the theoretical framework provided by the reaction theory of Feshbach [68]. Despite some difficulties with the exchanges of nucleons between the two nuclei which arise because of antisymmetrization, this approach often facilitates physical interpretations in a transparent way. Furthermore, the mean field defined in this way for a given heavy-ion system also sustains bound states which can be tentatively associated with actual ("quasi-molecular") states of the compound system. Indeed, evidence has been adduced in some cases for either bound states or quasi-bound resonances which seem to have the corresponding cluster structure, provided some account is taken of the Pauli principle (see, e.g., [92, 117]).

Our presentation here of Feshbach's theory is didactic and ignores many subtleties. We refer the reader to [68] for an authoritative discussion.

4.4.2. Outline of the theory

Let us initially ignore the exchange of nucleons due to antisymmetrization. Then the total wavefunction for the colliding projectile plus target system, $p + t$, may be expanded in terms of the complete set of internal eigenstates of the individual nuclei

$$\Psi = \sum_{ij} \chi_{ij}(\boldsymbol{r})\phi_{pi}(\xi_p)\phi_{tj}(\xi_t)\,, \tag{4.4}$$

where $\chi_{ij}(\boldsymbol{r})$ describes the relative motion when the nuclei are in their internal states labelled i and j. Then χ_{00} gives the elastic scattering if $i,j = 0$ denotes the ground states. We want an effective interaction, or optical potential, that will generate $\chi_{00}(\boldsymbol{r})$ when used in the one-body Schrödinger Eq. (4.1). Inserting the expansion (4.4) into the many-body Schrödinger equation and integrating over the internal coordinates results in an infinite set of coupled equations for the $\chi_{ij}(\boldsymbol{r})$. If we use Feshbach's projection operator formalism to eliminate explicit reference to the nonelastic channels [68, 182], we obtain an exact expression for the equivalent effective interaction which acts in the elastic channel alone and determines $\chi_{00}(\boldsymbol{r})$. This we may write

$$U_E = V_{00} + \lim_{\varepsilon\to 0} {\sum_{\alpha\alpha'}}' V_{0\alpha}\left(\frac{1}{E - H + \mathrm{i}\varepsilon}\right)_{\alpha\alpha'} V_{\alpha'0}\,. \tag{4.5}$$

Here V is the (real) interaction between the two nuclei, while α stands for a pair of internal state labels i,j. The prime reminds us that the sum runs over all states α in which at least one nucleus

is excited. The first term of (4.5) is real and is simply the folded potential

$$V_{00} = V_F(r) \equiv (\phi_{p0}\phi_{t0}|V|\phi_{p0}\phi_{t0}), \tag{4.6}$$

where the round brackets denote integration over the internal coordinates ξ_p and ξ_t of the two nuclei. Then we may rewrite (4.5) as

$$U_E = V_F(r) + \Delta U_E . \tag{4.7}$$

The second term ΔU_E is often referred to as the *dynamic polarization potential* (DPP) and arises from couplings to the nonelastic channels.

We should reemphasize that the potential U_E (and by implication an equivalent model potential), defined in this way, is designed, when used in the Schrödinger equation (4.1), to generate the relative motion $\chi_{00}(\boldsymbol{r})$ of the two nuclei while they both remain in their ground states. This may be a very small component of the total wavefunction in that region where the two nuclei overlap appreciably; in that case, the strong absorption into other channels manifests itself through $\chi_{00}(\boldsymbol{r})$ becoming small there.

4.4.3. Polarization effects

The physical processes associated with the DPP are easy to understand from Eq. (4.5). The interaction V excites one or both nuclei to the state α. The system then propagates under the influence of the mutual interaction according to the Green function

$$G = \lim_{\varepsilon \to 0}(E - H + i\varepsilon)^{-1} . \tag{4.8}$$

Because the Hamiltonian H contains the interaction V, the system may make a transition to a different inelastic channel, $\alpha' \neq \alpha$, during this propagation. Finally, V induces a transition back to the elastic channel.

Several properties of the DPP contribution ΔU_E to the effective interaction U_E are clear from Eq. (4.5) [182]. First, it depends explicitly upon the energy E. Second, it is complex. The imaginary part arises from energy-conserving transitions to open nonelastic channels in which flux is lost from the elastic channel. The real part comes from virtual excitations, corresponding to readjustments the two nuclei make as they begin to interact but which are reversed and they return to their ground states. Energetically closed channels can contribute to the real part of ΔU_E.

Lastly, the DPP is nonlocal; a system that is excited into a nonelastic channel at position $\boldsymbol{r}$ will, in general, return to the elastic channel at another position $\boldsymbol{r}' \neq \boldsymbol{r}$. Some procedure must be devised for obtaining an equivalent local potential before theoretically constructed effective interactions can be compared with local phenomenological ones.

4.4.4. Antisymmetrization and exchange

The individual internal nuclear wavefunctions $\phi_i(\xi)$ in (4.4) and (4.6) are each taken to be antisymmetrized, but the Pauli principle requires the total wavefunction (4.4) also to be antisymmetric under interchange of nucleons between the two nuclei. This introduces formal complications [68] that we shall not go into here. In practice, the only concession to antisymmetry that is made in the folding model (chapter 5) is to consider interchange of the two interacting nucleons. This process has been called *knock-on exchange* because in nucleon scattering from nuclei it results in a target

nucleon being ejected and replaced by the projectile nucleon following their mutual interaction. If the interaction V is comprised of two-body interactions

$$V = \sum_{pt} v_{pt}\,, \tag{4.9}$$

with p labelling a nucleon in the projectile and t one in the target, including this knock-on exchange is equivalent formally to replacing

$$v_{pt} \rightarrow v_{pt}(1 - P_{pt})\,, \tag{4.10}$$

where P_{pt} is the operator that exchanges all coordinates of these two nucleons. Then the first term (4.6) of the potential (4.5) is replaced in this approximation by

$$\begin{aligned} V_{00} = V_{\rm F}(r) &\equiv \left(\phi_{p0}\phi_{t0} \left| \sum_{pt} v_{pt}(1 - P_{pt}) \right| \phi_{p0}\phi_{t0} \right) \\ &= V_{\rm F}^{\rm D} + V_{\rm F}^{\rm E},\ \text{say}\,. \end{aligned} \tag{4.11}$$

Interchanging the spatial positions of the two nucleons affects the positions of the centres of mass of the two nuclei, and their separation changes to $\boldsymbol{r}' \neq \boldsymbol{r}$. The corresponding exchange contribution $V_{\rm F}^{\rm E}$ to the potential (4.11) becomes nonlocal. The range of nonlocality is not large because it arises from recoil effects $\sim A_p^{-1}$ and A_t^{-1} [78, 162], and is further limited by the finite range of v_{pt}. (A v_{pt} with zero range would result in a local potential.) In practical calculations, the nonlocal exchange contribution becomes replaced by an approximately equivalent local term [78, 181, 99] (see chapter 5).

The knock-on exchange contribution $V_{\rm F}^{\rm E}$ to the potential (4.11) is found to be far from negligible when realistic nucleon–nucleon interactions are used. The relative sizes of the direct $V_{\rm F}^{\rm D}$ and exchange $V_{\rm F}^{\rm E}$ terms are sensitive to the effective interaction chosen between two nucleons in odd states of relative motion [178, 20], although their sum $V_{\rm F}^{\rm D} + V_{\rm F}^{\rm E}$ is much less sensitive [178, 181]. This occurs because the "oddness" of the odd-state interaction yields direct and exchange terms of opposite sign which thus tend to cancel. A recent example [102] compares folded potentials calculated for α+^{40}Ca using G-matrix effective interactions based upon the Reid and the Paris nucleon–nucleon potentials. The older Reid-based interaction results in an attractive direct component, and an attractive exchange component of similar magnitude. On the other hand, the more realistic Paris-based interaction results in a *repulsive* direct potential. This is compensated for by a much more attractive exchange term, such that the summed direct plus exchange potentials from the two interactions are almost identical.

Finally, we should note again that the single-nucleon knock-on exchange potential discussed here cannot be compared directly with the one-nucleon exchange contribution to the RGM "potential" discussed in Section 4.3.2. The latter is an effective potential which contains contributions from the kinetic energy operators and orthogonality requirements, as well as from the interchange of nucleons that are not actively interacting with each other [69, 84, 87, 125].

4.4.5. The imaginary potential

Feshbach's formalism provides a convenient and transparent starting point for models of the absorptive processes that result in the imaginary part of the optical potential. Using Plemelje's

operator relation

$$\lim_{\varepsilon\to 0}\frac{1}{\alpha+i\varepsilon}=\mathscr{P}\left(\frac{1}{\alpha}\right)-i\pi\delta(\alpha)\,, \tag{4.12}$$

where $\mathscr{P}$ denotes the Cauchy principal value, we may formally separate ΔU of Eqs. (4.5) and (4.7) into its real and imaginary parts. A particularly simple expression for $\mathrm{Im}\,\Delta U$ emerges if we neglect the elements of V, and hence of the propagator G of (4.8), that are off-diagonal in the representation (4.4). Then

$$\mathrm{Im}\,\Delta U\equiv \mathrm{Im}\,U_E=-\pi\sum_{\chi}{}'V_{0\alpha}(\boldsymbol{r})\chi_\alpha(\boldsymbol{r})V_{\chi 0}(\boldsymbol{r}')\chi^*_\chi(\boldsymbol{r}')\delta(E-E_\chi)\,, \tag{4.13}$$

where again the prime on the sum reminds us that the ground state α with $i=j=0$ is excluded and where the energy-conserving delta function ensures that only open channels contribute. Actual calculations tend not to use the separation (4.12) but evaluate the full ΔU. With the same approximation of neglecting off-diagonal parts of G, we have

$$\Delta U(\boldsymbol{r},\boldsymbol{r}')=\sum_{\alpha\chi}{}'V_{0\alpha}(\boldsymbol{r})G_{\alpha\chi}(\boldsymbol{r},\boldsymbol{r}')V_{\chi 0}(\boldsymbol{r}')\,. \tag{4.14}$$

A model for the nonelastic processes determines the coupling terms $V_{0\alpha}$, while various approximations for the Green function $G_{\alpha\chi}$ have been used. In principle, the sum over intermediate states α is infinite (including continuum states of the two nuclei), but in practice, of course, a very truncated set of states is used. The expression (4.14) has been applied to the scattering of nucleons (for examples, see [168,49]), of alpha particles (for example, [172,203,60,123]) and of heavy ions [205] (see also [160] and other references there). An important simplification was introduced by Vinh Mau [123,205]; the important contributions to the sum over the intermediate states α in (4.14) were assumed to come from limited regions of excitation energy, so that the Green functions $G_{\alpha\chi}$ could be replaced by averages and taken out of the α sums, $G_{\alpha\chi}(\boldsymbol{r},\boldsymbol{r}')\to\bar{G}(\boldsymbol{r},\boldsymbol{r}')$. Closure could then be used to perform the α sum,

$$\sum_{\alpha}{}'|\alpha\rangle\langle\alpha|=1-|0,0\rangle\langle 0,0|\,, \tag{4.15}$$

where the last term corrects for the ground-state term being excluded from the primed sum. The final expression then depends only upon ground-state properties, with no explicit reference to the excited states except for the choice of an average excitation energy. A WKB approximation is used to simplify the Green function $\bar{G}(\boldsymbol{r},\boldsymbol{r}')$ and a Wigner transform is introduced to reduce the nonlocal potential to an approximately equivalent local one.

Despite the sequence of approximations involved, this approach has been quite successful in reproducing the main features of the imaginary potentials found empirically (see [160] and other references there), at least for peripheral collisions. The only application to a *light* heavy-ion system seems to be to $^{12}C+^{12}C$ [205]. While the predicted $\mathrm{Im}\,U$ is in agreement with phenomenological ones in the surface, it does appear to be too absorptive at small radii. It is not clear whether this is due to the approximations made in the theory or whether it is due to the particular model input used.

4.5. Dispersion relations and "threshold anomalies"

4.5.1. Dispersion relations

The first term of the potential (4.5) is independent of the energy E, while according to (4.12) the remaining DPP term is complex

$$\Delta U_E(\boldsymbol{r},\boldsymbol{r}') = \Delta V_E(\boldsymbol{r},\boldsymbol{r}') + \mathrm{i}W_E(\boldsymbol{r},\boldsymbol{r}')\,. \tag{4.16}$$

Feshbach [67, 68] seems to have been the first to point out that there is a dispersion relation between the real and imaginary parts

$$\Delta V_E(\boldsymbol{r},\boldsymbol{r}') = \frac{\mathscr{P}}{\pi}\int \frac{W_{E'}(\boldsymbol{r},\boldsymbol{r}')}{E'-E}\,\mathrm{d}E', \tag{4.17}$$

together with the complementary relation

$$W_E(\boldsymbol{r},\boldsymbol{r}') = -\frac{\mathscr{P}}{\pi}\int \frac{\Delta V_{E'}(\boldsymbol{r},\boldsymbol{r}')}{E'-E}\,\mathrm{d}E'. \tag{4.18}$$

These are analogues of the Kramers–Kronig relations for a complex refractive index in optics [93], and can also be interpreted as an expression of causality, namely that a scattered wave is never emitted before the arrival of the incident wave [48, 138].

Eqs. (4.17) and (4.18) explicitly refer to the property that the potential is nonlocal in coordinate space; the relations hold for any given pair $\boldsymbol{r}$ and $\boldsymbol{r}'$, as well as any weighted integral over them. As discussed elsewhere, this nonlocality (as well as that in V_{00} arising from exchange) is equivalent to a momentum dependence rather than a dependence on energy E, but phenomenological local potentials cannot distinguish between these dependences. Consequently, some of the energy dependence found for phenomenological optical model potentials is "spurious" and reflects an underlying nonlocality. Only the true, or "intrinsic", E-dependence is relevant to the dispersion relations (4.17) or (4.18). Some discussion has been given elsewhere [135] on how to account for the spurious part. Fortunately, there is some evidence that the spurious E-dependence is smooth and slow, whereas in the next section we are concerned with the consequences of a more rapid intrinsic variation with E. In practice [187] the relations (4.17) and (4.18) are usually assumed to hold for the phenomenological local potentials, but the possibility of some spurious effects due to nonlocality should always be kept in mind.

The dispersion integral (4.17) for ΔV_E involves $W_{E'}$ at all energies E'. In general, we will not know this, particularly the behaviour at high energy. Different hypothetical extrapolations may provide very different values for ΔV_E. However, our concern here is with the influence on ΔV_E of a rapid variation of W_E within a limited E range, rather than the absolute value of ΔV_E. A subtracted version of the relation is useful for this; effectively we normalize ΔV_E to its empirical value at some reference energy E_s and study the dispersive effects relative to that. This greatly reduces the sensitivity to the behaviour assumed for W_E at energies far from the ones of interest. We immediately get the subtracted form from (4.17)

$$\Delta V_E - \Delta V_{E_s} = (E-E_s)\frac{\mathscr{P}}{\pi}\int \frac{W_{E'}}{(E'-E)(E'-E_s)}\,\mathrm{d}E'. \tag{4.19}$$

The first point we note about the dispersion relations is that a potential that is real ($W = 0$) at all energies may be nonlocal but has no intrinsic E-dependence. Further, an absorptive potential that varies slowly with E, such as those constructed to represent the effects of Coulomb excitation or of the breakup of ions like ^{6}Li, is associated with only a weak real polarization potential. On the other hand, any rapid and localized variation of W_E *must* be accompanied by a variation in ΔV_E that is similarly localized in the energy E.

4.5.2. *Threshold anomalies*

As just remarked, a rapid intrinsic variation with E of the imaginary potential implies a corresponding variation of the real potential. In particular, the denominator in Eq. (4.17) ensures that if $|W_E|$ (where $W_E \leq 0$) increases rapidly over some small range of E, the associated contribution to ΔV_E will be attractive ($\Delta V_E < 0$) in that same E region. Since we expect that W_E will always vary in the way just described when nonelastic channels become open (hence the term "threshold"), the effect on the real potential (initially unexpected and so-called an "anomaly") should be a universal phenomenon, although the size and hence observability will depend upon the specific behaviour of W_E.

A very closely related "anomaly" for a nucleon traversing nuclear matter has been known for a long time (see [136] for example). In that case the Fermi surface plays the role of "threshold". The Coulomb barrier provides a threshold for heavy-ion collisions. Nonelastic channels begin to be effectively closed by the Coulomb repulsion at energies below and in the vicinity of the top of the barrier; consequently, the absorptive strength W_E decreases. This, and the associated increase in the attractive real potential, has been observed in a number of cases (see [187] for a summary of examples prior to 1991). The scattering of ^{16}O by ^{208}Pb (where the top of the Coulomb barrier occurs at $E/A \approx 5$ MeV) has become the classic, and most dramatic, example: see Fig. 4.1, which shows the strengths of the real and imaginary potentials near the strong absorption radius as a function of bombarding energy. The upper solid line shows the behaviour of the real potential predicted by the dispersion relation when the lower linear segments are used to represent W_E [187].

The Coulomb barrier is of much less importance for light heavy-ion systems (small Z_pZ_t), but the number of open nonelastic channels increases as the energy rises above the lowest threshold. This leads to $|W_E|$ increasing also, until eventually kinematic matching conditions become the controlling feature and W_E tends to level off or even decrease with further increase in E. It seems likely that this threshold behaviour of W_E will be less rapid than that caused by the Coulomb barrier in heavy systems; consequently, the associated anomaly in the real potential would be expected to be less strongly localized in energy. This is the case for the ^{12}C + ^{12}C system that is examined later [30].

Another manifestation of the threshold anomaly for heavy-ion collisions is the enhancement of fusion cross sections at near- and sub-barrier energies. All models of the fusion process involve a potential barrier which has to be at least partially penetrated before fusion occurs. Any increase in the attractive nuclear component of this barrier will lower it and tend to increase the fusion cross section [187].

4.6. *Deep or shallow potentials: Uniqueness*

One of the early questions raised concerning heavy-ion scattering was "Deep or shallow potentials?" (e.g., [179]). The predominance of strong absorption made the question somewhat academic,

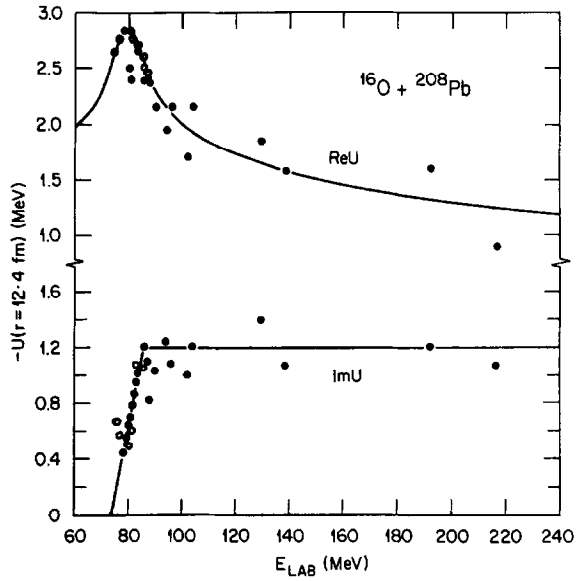

Fig. 4.1. Illustrating the "threshold anomaly" in the strengths of the real and imaginary parts of the optical potential for the scattering of $^{16}O + ^{208}Pb$ which occurs for energies in the vicinity of the top of the Coulomb barrier (about 80 MeV in this case). Plotted are the values of the potential at $r = 12.4$ fm, near the strong absorption radius. The curve for the real potential was obtained from the dispersion relation (4.17) using the straight line-segment representation shown for the imaginary potential (adapted from [153]).

but now one of our contentions is that careful studies of light heavy-ion systems have determined unambiguously that the physically realistic real potentials are indeed "deep". This follows the earlier conclusion, based upon the same arguments, that α-particle–nucleus real potentials are deep; that is, have depths ~100–200 MeV in the target interior [76].

For completeness, we should discuss briefly how unique these conclusions are. For example, it is known that many potentials may give the same scattering phase shifts, so presumably some implicit constraints accompany our conclusions. All the work reported here makes the basic assumption that the optical potential can be represented in a local form, is essentially independent of angular momentum l, and varies only slowly and smoothly with energy E. Within this context, we find the real potentials have depths and radial shapes consistent with the folding model when "realistic" nucleon–nucleon effective interactions are used. This gives us some confidence in the interpretation of these potentials as physically meaningful.

Recently, there have been interesting studies of the construction of *shallow* potentials that give the same scattering phase shifts as the deep ones (see [87] for a review). In particular, Baye [10, 11] applied supersymmetry arguments to construct shallow real potentials that are rigorously phase-equivalent to energy-independent, l-independent deep real potentials. At the same time, unphysical (e.g. Pauli-forbidden) bound states in the deep potential are eliminated. The resulting shallow potentials remain independent of energy, but exhibit a $1/r^2$ singularity at small radii and a strong dependence on angular momentum l. These operationally unpleasant properties, combined with the simple and intuitively pleasing interpretation of the deep potentials, seem to make the use of the deep potentials much more preferable and useful.

The fact that much heavy-ion scattering data can be fitted using shallow, nonsingular and l-independent potentials is due to the scattering, because of strong absorption, providing insufficient information to determine the potential unambiguously (or sometimes because of limited data). In particular, such data can only yield information on a relatively small "window" of partial waves for peripheral collisions.

5. Folded potential models

5.1. Introduction

As the reader will have surmised by now, we regard folded real potentials as central to our understanding of nucleus–nucleus interactions. They comprise the first-order term of the optical potential according to Feshbach's theory. In practice, they are modified by a renormalization factor N that is allowed to deviate from unity when experimental data are being fitted. It is assumed that this effectively takes into account higher-order corrections to the real potential from the real part of the DPP ΔU_E and perhaps additional corrections from nucleon exchanges. Of course, the needed deviation of N from unity should be small ($\lesssim 10\%$ or so) if the model is to remain meaningful. (Often adjustments of this order can hardly be distinguished from those due to uncertainties in the ingredients of the folding model itself.)

It is now time to turn to a more specific discussion of folding [162, 181, 182]. Most important is the choice of a realistic effective nucleon–nucleon interaction, but first we review the overall structure of the model. It is generally assumed that the interaction V is a sum of local two-body potentials v_{pt}, as in Eq. (4.9), although many-body aspects may be represented by a dependence of v_{pt} on the density of the nuclear matter in which the two interacting nucleons are embedded. Then the folded potential (4.6) may be written

$$V_F(\boldsymbol{r}) = (\phi_{p0}\phi_{t0}\,|V|\,\phi_{p0}\phi_{t0}) = \int \mathrm{d}\boldsymbol{r}_p \int \mathrm{d}\boldsymbol{r}_t\, \rho_p(\boldsymbol{r}_p)\rho_t(\boldsymbol{r}_t) v_{pt}(r_{pt}, \rho_p, \rho_t)\,, \tag{5.1}$$

where, for simplicity, we have ignored spin and isospin. Here ρ_p and ρ_t are the density distributions of the projectile and target ground states normalized so that

$$\int \rho_i(\boldsymbol{r}_i)\,\mathrm{d}\boldsymbol{r}_i = A_i\,. \tag{5.2}$$

The coordinates are defined in Fig. 5.1. We have allowed for a possible density dependence of v_{pt}. Because there is integration over two densities, expression (5.1) is often called *double folding*. Although involving a six-dimensional integral, it is very simple to evaluate if v_{pt} does *not* depend upon the densities. Then we use Fourier transforms to work in momentum space [181], thereby reducing the integral to a product of three one-dimensional integrals. When v_{pt} does depend upon the densities (see below), equally simple forms can be obtained if the density-dependence is chosen to factorize in certain ways, as in (5.20) below, for example. The power law (5.25) does not separate in the same way but results in a sum of a relatively few terms if the power β is integer and small and the prescription (5.21) is used. (Fortunately, $\beta = 1$ seems to be the favoured choice!) Evaluation of the exchange term is equally simple if the pseudo-potential approach (5.7), below, is taken. The more realistic treatment of Khoa et al. [98, 101] requires a little more effort.

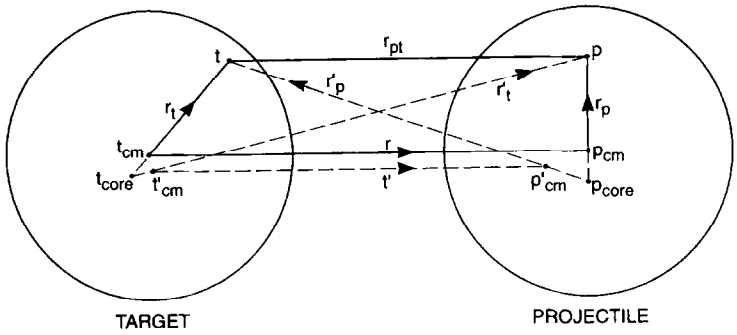

Fig. 5.1. The coordinates used in the double-folding integral (5.1). The primed coordinates and the dashed lines result after the nucleons p and t have been interchanged because of antisymmetrization. This illustrates how the centres of mass of the two nuclei are moved by the exchange, thus making the exchange part of the potential nonlocal.

The folding formula (5.1) satisfies some simple relations if v_{pt} does *not* depend upon the densities. If the density distributions are spherically symmetric and v_{pt} is scalar, we have

$$J(V_F) = J(v_{pt})J(\rho_p)J(\rho_t) = A_p A_t J(v_{pt}), \tag{5.3}$$

where $J(f)$ is the "volume integral" of the function f

$$J(f) = 4\pi \int f(r) r^2 \, dr. \tag{5.4}$$

Furthermore, the mean-square radii are related by

$$\langle r^2 \rangle_{V_F} = \langle r^2 \rangle_p + \langle r^2 \rangle_t + \langle r^2 \rangle_{v_{pt}}, \tag{5.5}$$

where

$$\langle r^2 \rangle_f = \int f(r) r^4 \, dr \Big/ \int f(r) r^2 \, dr. \tag{5.6}$$

The relations (5.3) and (5.5) do not hold if the interaction v_{pt} depends upon the densities ρ_p and ρ_t. Estimates of the corrections introduced by density dependence have been presented [195].

5.2. Knock-on exchange

As discussed in Section 4.4.4, the only effect of antisymmetrization under exchange of nucleons between the two nuclei that is normally included in the folding model is the single nucleon knock-on exchange in which the two nucleons that are interacting via v_{pt} are interchanged as in Eq. (4.11). This makes the exchange term in the potential nonlocal, as indicated in Fig. 5.1.

At least two groups [161, 162, 129] calculated this knock-on exchange potential and concluded that it could be estimated quite accurately by adding a zero-range pseudo-potential to the interaction v_{pt} in the matrix element (5.1). Namely, replace v_{pt} by

$$v'_{pt} = v_{pt}(1 - P_{tp}) \rightarrow v_{pt} + \hat{J}(E)\delta(\boldsymbol{r}_{pt}). \tag{5.7}$$

The zero-range immediately makes the exchange term local. The strength $\hat{J}(E)$ depends only weakly on the energy E. It has been obtained by calibrating against "exact" calculations for nucleon–nucleus scattering [129], or approximate calculations for heavy-ion scattering [78, 162, 53]. These two estimates may lead to considerably different results [189].

Instead of the simple but semiphenomenological approach of (5.7), a more consistent microscopic approximation to the exchange potential has been proposed (see [98, 101] and other references there). This takes explicit account of the finite range of v_{pt}, yet still results in a local potential through the use of local WKB approximations for the change in relative motion and for the off-diagonal elements of the one-body density matrices. The local momentum needed involves the potential that is being calculated, thereby posing a self-consistency problem. This may be solved iteratively. Despite these complications compared to the ansatz (5.7), the exchange potential is readily evaluated. No semiphenomenological adjustment is required, as was needed for the value of $\hat{J}(E)$ in Eq. (5.7); everything follows directly from the v_{pt} chosen. This approach has been applied successfully to the scattering of α-particles [102] and light heavy-ions [101, 103].

5.3. *The effective nucleon–nucleon interaction*

The success or failure of a folding model can only be judged meaningfully if the effective interaction employed is truly "realistic". Although much progress has been made, there are still many questions to be answered before we can be sure that the goal of realism has been reached [133, 134]. In our present brief review, we merely summarize some of the approaches now in use. As usual, an important criterion of realism is addressed by feedback from success or failure when a given approximation is confronted by experimental data.

The bare nucleon–nucleon potential, obtained from analysis of nucleon–nucleon scattering measurements, is too strong to be used directly (i.e. in Born approximation), but it is now widely recognized that the main features of the optical potential for nucleon–nucleus scattering can be understood by using the lowest-order Brueckner reaction matrix as an effective nucleon–nucleon interaction [136, 134, 133, 95]. Deriving this effective interaction for a finite nucleus is a formidable task, so the usual approach is to do so for infinite nuclear matter as a function of density. Then a local density approximation (LDA) is invoked. The LDA assumes that the interaction of a nucleon pair at a position $\boldsymbol{r}$ in a finite nucleus where the density is $\rho(\boldsymbol{r})$, is the same as in uniform nuclear matter with the same density. (Of course, this neglects any dependence on density gradients.)

The problem for heavy-ion scattering is further complicated because the two interacting nucleons are immersed in two pieces of nuclear matter moving relative to each other, which implies a quite different Pauli operator in the Bethe–Goldstone equation [13]. At least two attempts have been made to overcome this problem by solving the Bethe–Goldstone equation in this environment [180, 65]. The first attempt appears to result in real potentials that are too shallow and imaginary potentials that are too absorptive, although this could be due to the choice of nucleon–nucleon interaction and the approximations used. The second attempt identifies the optical potential with the energy-density curve, an approach that was criticized earlier (Section 4.3). As a consequence, the calculated real potential increases in depth as the energy increases (up to $E/A \approx 1$ GeV) instead of decreasing as found empirically [180, 65]. More frequently, however, the approach has been to use the LDA just described, replacing the single target density by the sum of the two colliding density distributions. Thus we neglect any dynamic consequences of their relative motion on the effective nucleon–nucleon

interaction, but this simple approach has had some remarkable success (documented in the remainder of this review).[2]

Before discussing some specific effective interactions that are in use, we examine the role of spin and isospin.

5.4. Spin and isospin structure

The central part of the effective nucleon–nucleon interaction v_{pt} may be written

$$v_{pt} = v_{00}(r_{pt}) + v_{01}(r_{pt})\tau_p \cdot \tau_t + v_{10}(r_{pt})\sigma_p \cdot \sigma_t + v_{11}(r_{pt})\sigma_p \cdot \sigma_t \tau_p \cdot \tau_t \,, \tag{5.8}$$

where σ, τ are the Pauli matrices for spin and isospin, respectively. In general, there will be spin–orbit and tensor terms also (for example, see [182, p. 638]). When either target or projectile has zero spin, the v_{ST} terms in (5.8) with $S = 1$ do not contribute. Similarly, the v_{ST} with $T = 1$ do not contribute if either nucleus has zero isospin ($N = Z$). Usually, the spin terms are relatively unimportant for determining cross sections (but, of course, can become important for polarization measurements). For one thing, only one or a few unpaired nucleons in each nucleus contribute to the $S=1$ potential whereas all nucleons contribute to the $S=0$ part.

Similarly, the $T = 1$ interactions tend to make either no contributions or only small ones. For example, the integrand of Eq. (5.1) for two spinless nuclei (so $S = 0$ only) may be written

$$\rho_p \rho_t v_{00} + (\rho_p^n - \rho_p^p)(\rho_t^n - \rho_t^p) v_{01} \,, \tag{5.9}$$

where ρ_i^n, ρ_i^p are the neutron, proton distributions, respectively, in nucleus i. For illustration, we may assume $\rho_i^n = (N_i/A_i)\rho_i$ and $\rho_i^p = (Z_i/A_i)\rho_i$, then (5.9) becomes

$$\rho_p \rho_t \left[v_{00} + v_{01} \frac{(N_p - Z_p)}{A_p} \frac{(N_t - Z_t)}{A_t} \right]. \tag{5.10}$$

Now v_{01} and v_{00} are comparable in magnitude for realistic interactions (typically $v_{01}/v_{00} \sim -0.5$), whereas the product of asymmetries $(N_i - Z_i)/A_i$ is usually either zero or very small, even for light systems involving an "exotic" neutron-rich nucleus like ^{11}Li [106].

Consequently, almost all calculations of folded potentials have utilized only the spin-, isospin-independent interaction v_{00}.

Frequently, instead of the representation (5.8), the nucleon–nucleon interaction is expressed in terms of the total spin (singlet S or triplet T) of the two-nucleon system and the parity of its relative orbital angular momentum (even E or odd O). In these terms, for example, the spin-, isospin-independent component v_{00} becomes [14, 182]

$$v_{00} = \tfrac{1}{16}(3v_{SE} + 3v_{TE} + v_{SO} + 9v_{TO}) \,. \tag{5.11}$$

This representation is particularly convenient when considering exchange, for the effect of the exchange operator P_{pt} is to change the sign of the odd-state components and leave the even-state ones unchanged. Thus the interaction $\hat{v}_{00}$ appropriate for the knock-on exchange term becomes

$$\hat{v}_{00} = \tfrac{1}{16}(3v_{SE} + 3v_{TE} - v_{SO} - 9v_{TO}) \,. \tag{5.12}$$

[2] However, as Mahaux [134] remarks, we must beware of confusing a successful comparison to experimental data with a theoretical justification. It is necessary but not sufficient.

This change of sign also implies some cancellation of the odd-state contributions when the direct and exchange potentials are added, making the results less sensitive to the choice of odd-state interaction. However, this cancellation can never be complete, as we now see.

Both even and odd terms contain a long-ranged (≈ 1.4 fm) piece from the one-pion exchange potential (OPEP). The OPEP is proportional to $(\sigma_p \cdot \sigma_t)(\tau_p \cdot \tau_t)$, so can only contribute to the v_{11} component in Eq. (5.8). Thus we find the sum of its contributions to Eq. (5.11) vanishes; the even-state pieces are cancelled by the odd-state ones. However, the change of sign for the latter in the exchange interaction $\hat{v}_{00}$ of (5.12) means the OPEP *does* contribute there.

5.5. *Density-independent M3Y interactions*

A variety of effective nucleon–nucleon interactions have been introduced into the folding model, but that which became known as M3Y is probably the most widely used and certainly is representative of "realistic interactions".

Details are given by Bertsch et al. [14]. The derivation proceeded in two steps. First the Bethe–Goldstone equation was solved in an harmonic oscillator basis, using the Reid [171] soft-core interaction, to yield the Brueckner reaction- or G-matrix. An oscillator parameter $\hbar\omega = 14$ MeV was chosen, appropriate for nuclei near ^{16}O. Then a sum of Yukawa terms was found whose oscillator matrix elements most closely reproduced the G-matrix ones. The central components were fitted using three Yukawa terms with ranges of 0.25, 0.40 and 1.414 fm (hence the notation M3Y, with M standing for Michigan to distinguish it from some other, similar, interaction models being investigated at that time). The term with the longest range was fixed to be the OPEP, leaving the other two strength parameters to be adjusted for each central component. The odd-state components of the central interaction are the most poorly determined parts. Instead of using the Reid results for them, it was proposed to use pure OPEP for the triplet-odd interaction and a three-Yukawa fit to the oscillator matrix elements of Elliott et al. [63] for the singlet-odd interaction.

This work was later extended to use the more modern and more fundamental Paris nucleon–nucleon potential [122]. This potential was used to generate *all* (odd as well as even) components of the effective interaction [5]. To distinguish these variants, one should refer to the M3Y-Reid and M3Y-Paris effective interactions.

Results were given for all spin, isospin components of the interaction, including spin–orbit and tensor, but our primary interest here is in the $S = T = 0$ spin- and isospin-independent central term. Explicit forms for this term follow:

$$\text{M3Y-Reid:} \quad v_{00}(r) = \left[7999\frac{e^{-4r}}{4r} - 2134\frac{e^{-2.5r}}{2.5r}\right] \text{MeV}, \tag{5.13}$$

$$\text{M3Y-Paris:} \quad v_{00}(r) = \left[11062\frac{e^{-4r}}{4r} - 2538\frac{e^{-2.5r}}{2.5r}\right] \text{MeV}. \tag{5.14}$$

Both versions consist of a short-ranged repulsion and a longer-ranged attraction, passing through zero near $r \approx 0.5$ fm. In momentum space this implies a change of sign near $q \approx 2\,\text{fm}^{-1}$. These are common characteristics of realistic effective interactions.

The interactions (5.13) and (5.14) have volume integrals (5.4) of $J_{00}(\text{Reid}) = -146\,\text{MeV fm}^3$ and $J_{00}(\text{Paris}) = +131\,\text{MeV fm}^3$. They are not as short-ranged as their component Yukawas might

suggest. The mean-square radius (5.6) for the Reid version is 7.26 fm^2 (the same as a single Yukawa with a range 1.10 fm), while for the Paris version it is 8.73 fm^2 (as for a single Yukawa with a range 1.21 fm).

As discussed earlier, the knock-on exchange matrix element involves interactions $\hat{v}$ in which the odd-state contributions have changed sign. This allows the OPEP, absent from (5.13) and (5.14), to contribute to $\hat{v}_{00}$:

$$\text{M3Y-Reid:} \quad \hat{v}_{00}(r) = \left[4631\frac{e^{-4r}}{4r} - 1787\frac{e^{-2.5r}}{2.5r} - 7.847\frac{e^{-0.7072r}}{0.7072r}\right] \text{MeV}, \tag{5.15}$$

$$\text{M3Y-Paris:} \quad \hat{v}_{00}(r) = \left[-1524\frac{e^{-4r}}{4r} - 518.8\frac{e^{-2.5r}}{2.5r} - 7.847\frac{e^{-0.7072r}}{0.7072r}\right] \text{MeV}. \tag{5.16}$$

These forms have been used in recent calculations of the exchange potential for α-particle–nucleus and heavy-ion scattering [101–103] in which the finite range was accounted for explicitly as described in Section 5.2. However, many other calculations use the zero-range pseudo-potential of Eq. (5.7) to represent the knock-on exchange. The magnitude of $\hat{J}_{00}(E)$ has been determined empirically [129] by comparing cross sections for protons scattering from various targets, and at various energies up to 80 MeV, calculated using (5.7) with those in which the exchange was calculated exactly. The results using the Reid interaction can be expressed as

$$\text{M3Y-Reid:} \quad \hat{J}_{00}(E) \approx -276\,[1 - 0.005(E/A)]\ \text{MeV fm}^3, \tag{5.17}$$

while use of the Paris form gives

$$\text{M3Y-Paris:} \quad \hat{J}_{00}(E) \approx -590\,[1 - 0.002(E/A)]\ \text{MeV fm}^3, \tag{5.18}$$

where E/A is the bombarding energy per projectile nucleon in MeV. (An alternate approach [78,53] to the estimation of $\hat{J}_{00}$ can lead to a significantly different energy dependence [189].)

A notable difference between the Reid-based and Paris-based *direct* interactions (5.13) and (5.14) is that the latter is repulsive. Its volume integral is comparable in magnitude to the Reid one, but of opposite sign. On the other hand, the Paris *exchange* term is roughly twice as attractive as the Reid one; this is made particularly evident in the pseudo-potential strengths (5.17) and (5.18). However, when direct and exchange potentials are combined, their sums are very similar [102]. This emphasizes the importance of including the knock-on exchange when calculating the folded potentials. The magnitudes of the exchange terms compared to the direct ones also emphasize the need to treat the exchange as accurately as possible.

Finally, two more general comments on these M3Y interactions must be made. First, they are purely real, so that the imaginary part of the optical potential either has to be constructed independently (Section 4.4.5) or, most frequently, treated phenomenologically.

Secondly, they are independent of the density of nuclear matter in which the two nucleons are embedded, and are also independent of energy except for the weak dependence of the knock-on exchange. Indeed, from their origin as fits to oscillator matrix elements, one sees that they concern the effective interaction of two nucleons within a nucleus like ^{16}O, and hence represent some average over a certain range of energies and over a range of densities from zero to normal nuclear matter.

It is now appropriate to turn to a more careful consideration of how the effective interaction varies with the density of the medium.

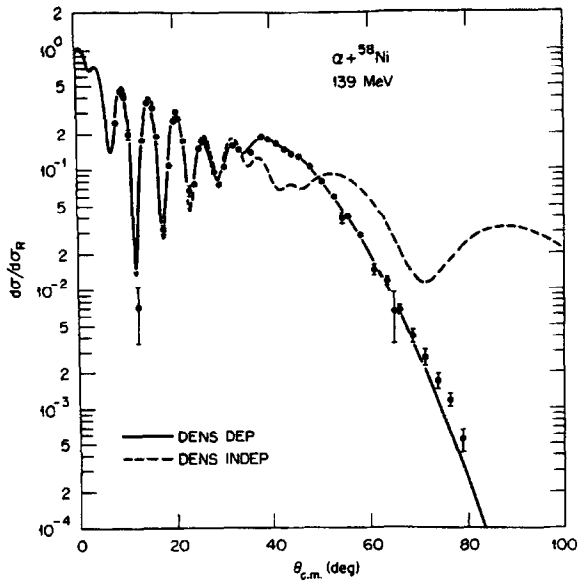

Fig. 5.2. Illustrating the importance in the folding model for alpha particle scattering of a density dependence of the interaction. The potentials for peripheral collisions are almost the same in the two cases, hence give the same scattering at small angles, but the density dependence makes the potential much less deep in the interior and gives very different scattering at large angles (from [182]).

5.6. *Density-dependent M3Y interactions*

It has long been recognized that the effective interaction between two nucleons in a nucleus depends upon the density of the surrounding medium (for example, see [13] and references there); indeed, this density dependence is required for nuclear matter to saturate rather than collapse. Saturation requires that the attraction weakens as the density increases.

Perhaps the first clear indication that this plays an important role in the folded potential arose from studies of α-particle scattering. Folded potentials based upon density-independent interactions like the M3Y could reproduce the data at forward angles or low energies; that is, they correctly predicted the potential experienced in peripheral collisions. However, the rainbow-like features seen at higher energies and larger angles were not reproduced because these features are sensitive to the real potential at smaller radii. The folded potential was too deep there by almost a factor of two. This is a clear indication that the effective interaction must depend upon the position within the nucleus of the two interacting nucleons. A dependence upon density is a simple way to represent this and has a sound physical basis. Fig. 5.2 illustrates the effect, and provides another example of how the observation of refractive phenomena, discussed in chapter 3, can be an important source of physical information.

(One might wonder if the additional contribution to the folded potential from the real part of the DPP (Section 4.4.3) would provide an alternative explanation. However, estimates of this contribution [204] indicate that it is small and, besides, is attractive, not repulsive.)

5.6.1. The DDM3Y interaction

A variety of density-dependent interactions have been introduced. Here we discuss some based upon the M3Y interaction of the preceding section. It was assumed that the radial dependence is independent of the density and energy so we can use a factored form

$$v^{\mathrm{DD}}(\rho,E,r) = f(\rho,E)v'(r)\,, \tag{5.19}$$

where $v'(r)$ is the original M3Y interaction (including the knock-on pseudo-potential) described in the preceding section. There is no theoretical justification for this factorization, but it does not seem to be an unreasonable approximation that the shape of $v(r)$ does not vary *strongly* with density (or energy over the range of main concern here, $E/A \sim 10$–100 MeV). Furthermore, as already stressed, the original M3Y interaction itself already represents some average over density and energy.

The first version [109, 110] took $v'(r)$ to be the M3Y (Reid) interaction (5.13) together with the knock-on exchange pseudo-potential as in (5.7) and (5.17). The density dependence adopted was

$$f(\rho,E) = C(E)[1 + \alpha(E)\mathrm{e}^{-\beta(E)\rho}]\,, \tag{5.20}$$

with

$$\rho = \rho_p(r_p) + \rho_t(r_t)\,. \tag{5.21}$$

This choice allows for a simple factorization of the integrand of the folding integral (5.1) which allows one to easily perform the integration in momentum space [181]. In the density-dependent term one simply replaces each $\rho_i(r_i)$ by

$$\tilde{\rho}_i(r_i) = \rho_i(r_i)\mathrm{e}^{-\beta\rho_i(r_i)}\,. \tag{5.22}$$

(Possible changes due to a choice of coordinates other than those chosen in (5.21) were examined by Goldfarb and Nagel [79].) The parameters $C(E), \alpha(E)$ and $\beta(E)$ were chosen at each energy so as to make the variation with density of the volume integral of v^{DD} match as well as possible the results of the Brueckner-type calculations of Jeukenne et al. (JLM) [95] for a nucleon scattering from nuclear matter of various densities ρ ranging from about 5% to 100% of "normal" nuclear matter ρ_0, and at nucleon energies from 10 to 140 MeV.

The volume integral $J_{00}^{\mathrm{DD}}(\rho,E)$ of the spin- and isospin-independent interaction v_{00}^{DD} is to be identified with the quantity $V_0(\rho,E)/\rho$ of JLM. The behaviour with energy and density is illustrated in Fig. 5.3 taken from JLM, and the parameter values obtained are indicated in Fig. 5.4 [110, 64, 29]. The JLM calculations implicitly include the knock-on exchange. We also note that adopting the form (5.19) assumes the same density dependence for the direct and exchange terms. The JLM calculations give both the real and imaginary parts of the G-matrix interaction, but the imaginary parts, while moderately successful in describing nucleon–nucleus scattering, are not thought to be appropriate for heavy-ion collisions. The spectrum of open channels for two heavy ions is quite different, and excitation of surface collective modes, absent from uniform nuclear matter, is known to be important [97, 205, 160].

Thus, in summary, the spin- and isospin-independent part of the DDM3Y interaction is

$$v_{00}^{\mathrm{DDM3Y}}(\rho,E,r;\mathrm{Reid}) = f(\rho,E)[v_{00}(r;\mathrm{Reid}) + \hat{J}_{00}(E;\mathrm{Reid})]\,, \tag{5.23}$$

where f is given by (5.20), v_{00} by (5.13) and $\hat{J}_{00}$ by (5.17).

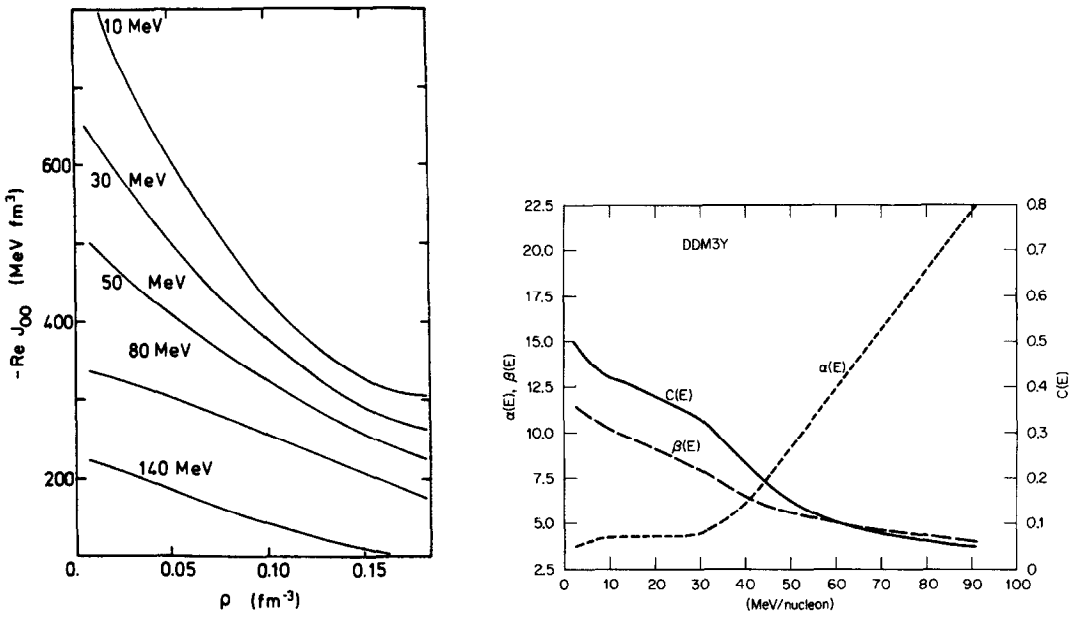

Fig. 5.3. The volume integral of the spin- and isospin-independent real part of the G-matrix interaction calculated by Jeukenne et al. [95] for a nucleon of various energies scattering from uniform nuclear matter of density ρ. These results implicitly include the knock-on exchange (from [95]).

Fig. 5.4. The parameter values adopted for the density- and energy-dependence (5.20) of the effective interaction DDM3Y [110, 64, 29], obtained by matching the G-matrix results of [95].

One difficulty with the form (5.20) for $f(\rho)$ is that densities roughly twice that of normal matter, $\rho \approx 2\rho_0$, are encountered when strong overlap of the two ions occurs, whereas the normalization to JLM is only possible up to $\rho \approx \rho_0$. Extrapolation beyond that using the exponential form in (5.20) is questionable. More reliable, perhaps, is a power-law dependence, even though it does not enjoy the factorization property that led to the simplification (5.22). We now turn to a development that uses such a dependence, and also invokes the saturation of nuclear matter as a constraint, as well as employing a more careful and less phenomenological treatment of the knock-on exchange.

5.6.2. Saturation as a constraint on the interaction

One motivation for originally introducing density dependence into the effective nucleon–nucleon interaction was that it was needed to ensure the saturation of nuclear matter [13]. This implies an important constraint [162] if we are to take seriously the idea that the effective interaction required to generate optical potentials for scattering is essentially the same as that needed for nuclear structure problems such as the shell-model (Hartree–Fock) potential for bound nucleons. This idea has a firm theoretical basis for nucleon–nucleus systems [133, 134, 136], but unfortunately there is no similar truly microscopic theory supporting the idea for nucleus–nucleus systems. Nonetheless, it provides a reasonable *ansatz* to be tested, tests which it appears to have survived, at least for the light heavy-ion systems reviewed here.

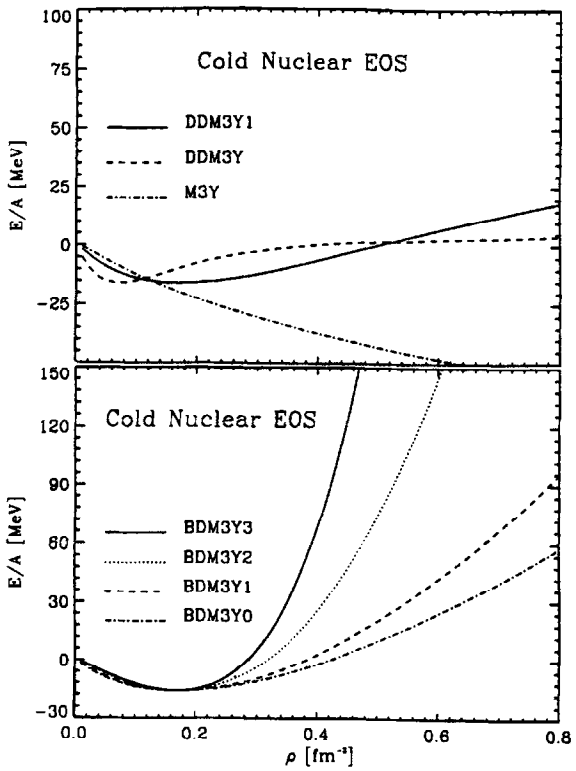

Fig. 5.5. The equation of state (EOS) for symmetric cold nuclear matter, calculated for various effective nucleon–nucleon interactions. The M3Y interaction does not give saturation, while the original DDM3Y interaction saturates with the observed binding energy per nucleon (here denoted E/A) but at much too small a density. The various interactions of Khoa et al. were adjusted to give the observed binding energy of 16 MeV at the density of 0.17 fm^{-3}. Shown are the EOS for the interactions based upon the Reid nucleon–nucleon force (from [100]).

The binding energy of nuclear matter is given (in Hartree–Fock approximation) by the sum of the kinetic and (one-half of) the potential energies of the individual nucleons. The binding energy per nucleon, B, should saturate, i.e. have a minimum as a function of ρ, with $B_0 \approx 16$ MeV at $\rho = \rho_0 \approx 0.17$ fm^{-3}. The curvature of $B(\rho)$ at $\rho = \rho_0$ gives the incompressibility of normal nuclear matter

$$K = 9\rho^2(\partial^2 B/\partial\rho^2)|_{\rho=\rho_0}\,, \tag{5.24}$$

an important quantity about which considerable uncertainty still remains.

The M3Y interaction itself does not saturate; $-B(\rho)$ continues to increase as the density ρ grows (Fig. 5.5). However, the introduction of a density dependence $f(\rho)$, as in (5.19), which weakens the attractive interaction as ρ increases, allows saturation to occur. The exponential parameterization (5.20), with the parameter values (Fig. 5.4) for $E/A = 5$ MeV, together with the M3Y(Reid) interactions (5.13) and (5.15), gives a minimum at $\rho_0 \approx 0.07$ fm^{-3} with $B_0 \approx 15.9$ MeV [100]. Consequently, the conventional DDM3Y form does not satisfy the criterion; it saturates with the appropriate energy but at much too low a density (Fig. 5.5).

Khoa et al. [100–103] have addressed this problem recently. For simplicity, the parameters in the density dependence $f(\rho)$ are assumed to be independent of energy, in contrast to the original DDM3Y of the preceding section (Fig. 5.4). Initially, the C, α and β of the exponential form (5.20), in conjunction with the M3Y-Reid or M3Y-Paris interactions of Eqs. (5.13)–(5.16), were adjusted so as to give $B_0 = 16\,\text{MeV}$ at $\rho_0 = 0.17\,\text{fm}^{-3}$. These versions were denoted DDM3Y1 and the parameter values given in [102]. They correspond to rather soft equations of state (EOS) for nuclear matter with $K = 171$(Reid) and 176(Paris) MeV. The exponential dependence on ρ in (5.20) is restrictive and the parameters cannot be adjusted to satisfy the saturation properties with a larger value of K. (Note that if C and α are positive, as required, $f(\rho)$ cannot change sign as ρ increases.)

Consequently, a more realistic power-law dependence on ρ [13] was adopted

$$f(\rho) = C(1 - \alpha\rho^{\beta}), \tag{5.25}$$

which can change sign at large ρ. The power β is taken to be one-third of an integer, corresponding to dependence upon an integer power of the Fermi momentum. Various β were chosen ($\beta = \frac{2}{3}$, 1, 2 and 3) in combination with M3Y-Reid or M3Y-Paris, and values for C and α found which satisfy the saturation conditions $B_0 = 16$ MeV and $\rho_0 = 0.17\,\text{fm}^{-3}$; these are given in [102], together with the corresponding K values which range from 170 to 566 MeV. These interactions were denoted BDM3Yn, $n = 0$–3, respectively, and the resulting EOS are illustrated in the lower part of Fig. 5.5.

The folding model for the scattering of two nuclei as used here takes ρ to be a simple superposition of the target and projectile densities.[3] Thus the total density ρ approaches $2\rho_0$ when the two nuclei overlap strongly (even more for α-particle–nucleus systems [102]). This makes the folded potential at small radii sensitive to the kind of density dependence assumed. The interaction in this region weakens as n (or the power β) increases, thereby offering the opportunity to determine the appropriate n (or β) whenever the scattering is sensitive to the depth of the potential in the interior. In this way we can obtain a measure of the incompressibility K. With this in mind, the DDM3Y1 and BDM3Yn interactions have been applied to the scattering of nucleons [100] and alpha particles [102] from nuclei, and the scattering of light heavy-ion systems [101, 103]. The latter analyses are described in more detail below; here we only remark that they consistently favour the DDM3Y1 or BDM3Y1 interactions. The parameters that describe the corresponding density dependencies of these interactions are given in Table 1, together with the incompressibilities K. For example, for complete overlap, $\rho = 2\rho_0$, the BDM3Y1(Paris) interaction is reduced in strength by a factor of $f(2\rho_0)/f(0) = 0.407$. This factor becomes 0.433 for the DDM3Y1(Paris) interaction. In other words, the interaction between two ions is roughly halved by the density dependence when they completely overlap.

If we give maximum weight to the power-law (5.25) and the M3Y-Paris interaction (5.14) and (5.16) as being the most realistic, these analyses imply $K \sim 270$ MeV. Use of the M3Y-Reid form gives a somewhat smaller $K \sim 230$ MeV, while employing the less realistic exponential form (5.20) results in an even lower value of $K \sim 175$ MeV.

[3] The density superposition (5.21) is used for the direct interaction, while for the exchange terms the coordinates are chosen so that the density is evaluated at a position midway between the positions of the two nucleons before and after they are exchanged.

Table 1
Parameters of the density dependencies of the favoured DDM3Y1 and BDM3Y1 interactions, and the corresponding nuclear matter incompressibilities κ (from [102])

Interaction	C	α	β	κ (MeV)
BDM3Y1-Paris[a]	1.2521	1.7452 fm^3	1.0	270
BDM3Y1-Reid[a]	1.2253	1.5124 fm^3	1.0	232
DDM3Y1-Paris[b]	0.2963	3.7231	3.7384 fm^3	176
DDM3Y1-Reid[b]	0.2845	3.6391	2.9605 fm^3	171

[a]Density dependence as in Eq. (5.25).
[b]Density dependence as in Eq. (5.20).

In the course of these applications to scattering data, it was found necessary [100] to introduce an additional mild energy dependence over that provided by localizing the exchange potential. This was parameterized as a linear function

$$g(E) = [1 - \gamma(E/A)], \tag{5.26}$$

with $\gamma = 0.002\ \mathrm{MeV}^{-1}$ (Reid) or $0.003\ \mathrm{MeV}^{-1}$ (Paris). The direct part of the full interaction now has the form

$$v_{00}^{\mathrm{DD}}(\rho, E, r) = g(E) f(\rho) v_{00}(r); \tag{5.27}$$

where v_{00} is given by (5.13) (Reid) or (5.14) (Paris). Likewise the exchange part becomes

$$\hat{v}_{00}^{\mathrm{DD}}(\rho, E, r) = g(E) f(\rho) \hat{v}_{00}(r), \tag{5.28}$$

where $\hat{v}_{00}$ is given by (5.15) (Reid) or (5.16) (Paris).

It was mentioned earlier (Section 5.5) that the M3Y-Paris direct interaction (5.14) was repulsive, in contrast to the attractive M3Y-Reid of (5.13), but that this difference was compensated for by the greater attraction of the Paris exchange term. This is illustrated in Fig. 5.6 for the folded potential for $\alpha + {}^{40}\mathrm{Ca}$, based upon the BDM3Y1 density-dependent version. The decompositions into direct and exchange components are very different, but their sums are almost indistinguishable.

The philosophy behind the work described in this section has been extended recently to asymmetric nuclear matter [106]. In this the isovector, spin-scalar components $v_{01}(r)$ and $\hat{v}_{01}(r)$ of the M3Y interactions [14, 5] were used together with the same forms of density dependence with parameters adjusted so as to reproduce the symmetry energy of nuclear matter, as well as the saturation properties previously discussed. Unfortunately, the symmetry (isospin-dependent) part of the central nucleus–nucleus potential is found to be only a few percent of the isoscalar term and does not have measurable effects on the elastic scattering cross sections, even for exotic neutron-rich systems like ${}^{11}\mathrm{Li} + {}^{14}\mathrm{C}$. It appears that one must appeal to charge-exchange reactions, which isolate the isovector part of the interaction from the isoscalar part, in order to test the validity of any model of the isovector interaction.

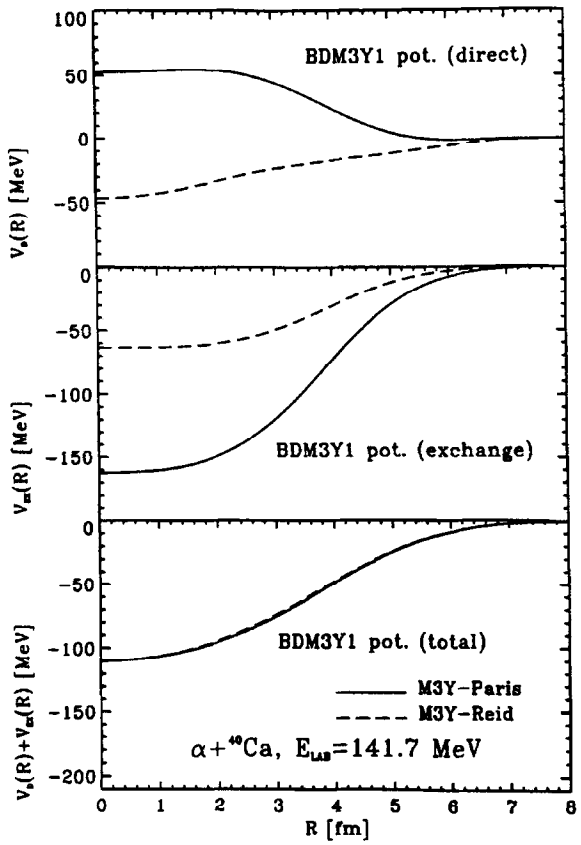

Fig. 5.6. Comparing the direct and exchange components of the folded potential for $\alpha+^{40}$Ca at 141.7 MeV, constructed using the BDM3Y1 interactions based upon either the Reid or more recent Paris nucleon–nucleon forces. The decompositions into direct and exchange components are very different, but their sums are almost identical (from [102]).

5.7. *The Coulomb potential*

At large separations r, where the hadronic forces have become negligible, the Coulomb interaction between two nuclei is usually assumed to be unambiguous and equal to

$$V_C(r) = Z_p Z_t e^2/r\,. \tag{5.29}$$

(This neglects small but long-ranged and complex contributions due to dynamic polarization of the nuclei by the Coulomb force itself [89].) The r^{-1} dependence of (5.29) is no longer valid when the two nuclear surfaces begin to overlap at smaller r. Frequently, the Coulomb potential at small r is represented by the potential felt by a point charge incident upon a uniform charge distribution of radius R_C, following a tradition established in the analysis of proton scattering. Unfortunately this prescription does not tell us what value to use for R_C in a nucleus–nucleus collision. Figs. 5.7 and 5.8 illustrate two choices for $^{16}O + {}^{16}O$, $R_C = 6.8$ and 4.3 fm. (The charge distribution of ^{16}O has an RMS radius of about 2.6 fm, corresponding to a uniform distribution with a radius of 3.4 fm.)

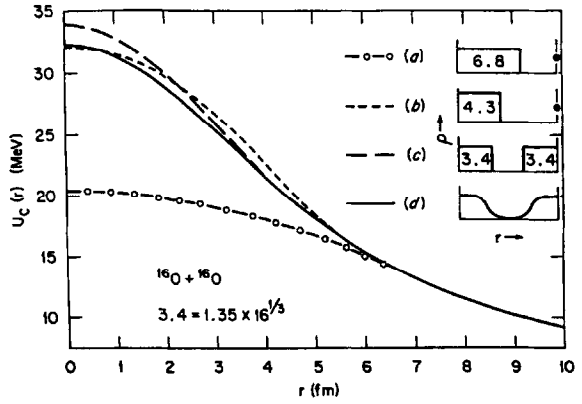

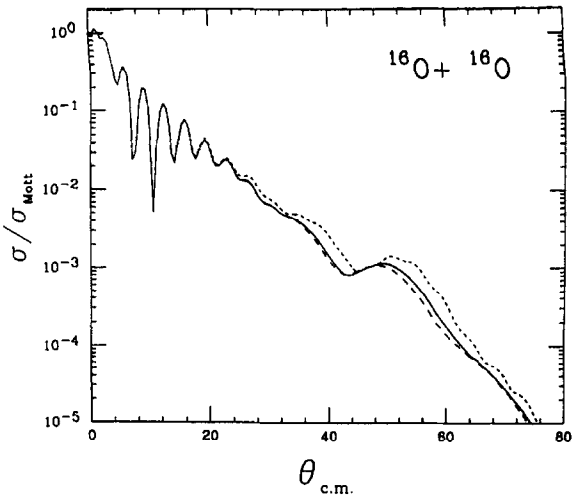

Fig. 5.7. Coulomb potentials for $^{16}O + ^{16}O$ according to various assumptions about the two charge distributions: (a) point + uniform distribution of radius 6.8 fm; (b) point + uniform distribution of radius 4.3 fm; (c) two uniform distributions each with radius 3.4 fm; (d) two rounded (shell model) distributions each with an RMS radius of 2.6 fm. The corresponding charge distributions are shown inset (from [182]).

Fig. 5.8. The angular distributions for $^{16}O + ^{16}O$ scattering at 350 MeV using three of the Coulomb potentials illustrated in Fig. 5.7, but the same nuclear potential. The dotted curve uses charge distribution (a), the dashed curve uses (b), while the solid curve uses (c).

The resulting V_C potentials differ by 60% at $r = 0$. This is a significant difference because $^{16}O + ^{16}O$ is one of the systems reviewed here whose scattering can reveal the strength of the (hadronic plus Coulombic) interaction at small radii. (Unfortunately, published reports of analyses do not always specify what form of V_C was used. The nuclear potentials that optimize the fit to the 350 MeV data may differ up to 6–7 MeV ($\sim$ 4% of their value) at small radii, depending on the choice of 6.8 or 4.3 fm for R_C.)

We should employ a more realistic, folded, Coulomb potential to be consistent with the folding approach to the hadronic interaction (although this still neglects an exchange Coulomb contribution arising from antisymmetrization). There is an analytic expression available [94, 166] when each nucleus is represented by a uniform charge distribution. This choice for $^{16}O + ^{16}O$ is shown as (c) in Fig. 5.7, together with (d), the result of numerically folding over two rounded (shell-model) distributions, each with the same RMS radius of 2.6 fm. These two choices agree quite well, giving V_C that differ only by a few percent even at $r = 0$.

It is also interesting to note that the "point plus uniform distribution" approximation, which is often incorporated in computer programs for scattering problems, requires a radius R_C appreciably smaller than the sum of the radii of the two nuclei in order to give a V_C comparable to the more realistic ones. For example, Fig. 5.7 shows that $R_C \approx 4.3$ fm is needed for $^{16}O + ^{16}O$. In the usual parameterization

$$R_C = r_C[A_p^{1/3} + A_t^{1/3}], \tag{5.30}$$

this would imply $r_C \approx 0.85$ fm when $A_p = A_t = 16$. In general, for two distributions with equal radii $R_1 = R_2$, the Coulomb potential at the centre is always 1.6 times that for a "point plus uniform distribution" approximation with $R_C = R_1 + R_2$.

5.8. The dynamic polarization potential and breakup

5.8.1. Dynamic polarization

The dynamic polarization potential (DPP) was discussed formally in the context of Feshbach's theory [68] in Sections 4.4.2 and 4.4.3, where it was denoted ΔU_E. The absorptive, imaginary part was discussed in Section 4.4.5, but little attention has been paid so far to the real part. This represents a correction to the folded real potential and should be small if the simple folding model is to be a reliable guide to the properties of the real optical potential. The existence of threshold anomalies (Section 4.5 and Fig. 4.1) shows that this is not always so. Such cases occur at relatively low bombarding energies, where the scattering is not particularly sensitive to the detailed shape of the real potential but is determined largely by the value and slope of the potential in the vicinity of some strong absorption radius. Consequently, it is often sufficient to simply renormalize the real folded potential in order to fit the data.

However, it would be very surprising if, in fact, the real part of the DPP had the same radial shape as the folded potential $V_F(r)$. For example, if the virtual excitation of collective surface modes is important, one might expect the DPP to be concentrated near the surface [8, 9, 70].

The overall success of realistic folding models, as indicated by a need for renormalization factors N close to unity (with the exception of threshold anomalies), implies that in most cases the real DPP is relatively weak. One other important exception occurs for the scattering of weakly bound nuclei, and we turn now to this class.

5.8.2. Breakup effects

It was recognized early that the folding model appeared to fail for the scattering of the weakly bound nuclei ^{6,7}Li and ^{9}Be [181]. These data required a substantial renormalization of the real folded potential by factors of $N \sim 0.6$. (Initially [181] the scattering of ^{7}Li seemed to be "normal", but later studies revealed it to be just as "anomalous" as ^{6}Li [185].)

It was natural to associate this failure of the model with the enhanced breakup of the projectile nuclei due to their weak binding. (The ground states of ^{6,7}Li and ^{9}Be are bound by only 1.47, 2.48 and 1.57 MeV, respectively.) Subsequently, the effects of breakup have been investigated in detail, using coupled discretized continuum channels (CDCC) techniques [185]. These studies confirm that including couplings to the breakup channels allows one to fit the elastic data by using the full folded potential without substantial renormalization ($N \approx 1$).

We can expect similar, or even stronger, effects in the scattering of more exotic, weakly bound nuclei close to the nucleon drip lines, such as ^{11}Li [90] which is bound by only about 300 keV.

It is also possible to construct wavefunction-equivalent (or "trivially equivalent") local potentials from the solutions of the coupled equations that will generate exactly the same elastic wavefunctions and the same elastic scattering when used in a one-channel Schrödinger equation (see [89], for example). In other words, these are local representations of the DPP. The price paid for localizing in coordinate space is that these DPP depend upon the angular momentum variables. However, the

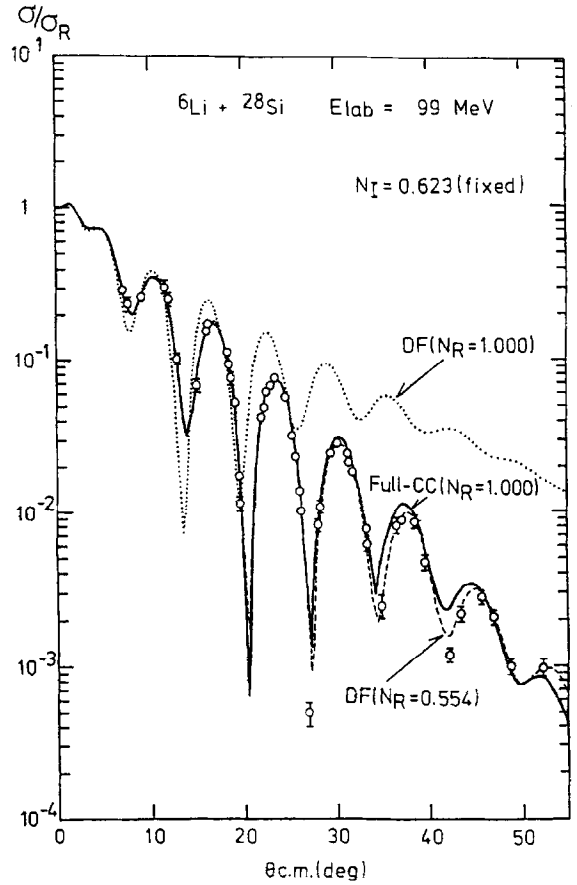

Fig. 5.9. The effect of couplings to breakup channels on the elastic scattering of ^{6}Li + ^{28}Si at 99 MeV. A folded potential obtained from the M3Y interaction was used, multiplied by a complex normalization factor ($N_R + iN_I$). N_I was fixed at 0.623. Without the breakup couplings, the value $N_R = 1.0$ does not reproduce the data (dotted curve), and has to be severely reduced to $N_R = 0.554$ (dashed curve). However, the value $N_R = 1.0$ does give an acceptable fit (solid curve) when the couplings to the breakup channels are included, showing how the breakup effects have an effect mostly on the real potential (from [185]).

dependence of the DPP upon angular momentum is not strong for the important peripheral partial waves or at large radii, so we may expect to learn something about their average behaviour.

5.8.3. The scattering of ^{6}Li

The CDCC techniques have been applied particularly to study the effects of breakup on the scattering of ^{6}Li. The calculations reported in [185] employed the M3Y interaction defined in Section 5.5 for both the real and imaginary potentials. (It would be very interesting to repeat these calculations using what we now think to be the more realistic density-dependent interaction described in Section 5.6. We would not expect the qualitative features to change for cases where the scattering is dominated by peripheral collisions, but differences could occur when the scattering becomes

sensitive to the interior of the potential.) Breakup of ^{6}Li into $\alpha + d$ in relative s-, p-, and d-wave states was taken into account. Bombarding energies of 34–156 MeV, on various targets, were considered. It was found that the scattering predicted by the coupled-channels calculations, using the full M3Y interaction (with $N = 1$), was very similar to that obtained in the one-channel (optical model) calculations with a reduced M3Y interaction ($N \approx 0.6$) for the real potential, as was required to fit the experimental data. Curiously, the same *imaginary* potential could be used in both types of calculation (in practice, in these calculations the same folded M3Y shape was used for the imaginary potentials, reduced in strength by $N_I \approx 0.6$). This implies that breakup has rather little effect on the imaginary potential. Fig. 5.9 illustrates this for ^{6}Li $+^{28}$Si at 99 MeV.

These findings were corroborated when the local potentials equivalent to the coupled equations were examined [185]. The DPP were found to have strongly repulsive real parts in the surface region and weak imaginary parts. This is in contrast to the DPP resulting from couplings to inelastic channels whereby the target is excited to bound vibrational states; there the average DPP is found to be predominantly imaginary [89]. Thus these vibrational couplings have little influence on our judgment of the success of the folding model for the real potential, while the imaginary potential is usually treated phenomenologically anyway.

The characteristics just discussed were found to be sensitive to the nature of the coupling to the nonelastic channels. A largely real coupling, such as is usually assumed for the excitation of low collective states, results in a DPP that is mostly imaginary, while a coupling with a strong imaginary part, such as was used for the breakup reactions, tends to give a DPP that is mostly real and repulsive. For further discussion, the reader may consult the detailed review by Sakuragi et al. [185].

6. Applications to experimental data

A large amount of light heavy-ion data have been successfully analysed with potentials obtained microscopically or by using deep phenomenological potentials. We present the data, the main results from the optical model analyses in relation to the potential themselves and other related quantities such as total reaction cross sections.

Much of the data are obtained for the scattering of two identical nuclei. Hence the differential cross sections are symmetric about 90° in the cm system, thus restricting the angular range that can provide information. In addition, we may see structure near 90° that arises from interference between the unsymmetrised amplitudes for scattering to θ and $\pi - \theta$, which may obscure structure that arises from refractive effects. Despite these possible limitations, most of what we have learnt about refraction in the scattering has come from these identical systems.

6.1. The data

In this section we refer to the elastic scattering data for light heavy-ion systems, mostly ^{12}C + ^{12}C, ^{16}O + ^{12}C and ^{16}O + ^{16}O, at E/A above 6 MeV, where the observation of refractive effects in the angular distributions has permitted the (relatively unambiguous) determination of the nuclear complex potential.

6.1.1. $^{12}C + ^{12}C$

In 1976, Stokstad and collaborators measured rather complete elastic scattering angular distributions of ^{12}C by ^{12}C at 14 laboratory energies between 71 and 127 MeV (E/A between 6 and 10 MeV) [206, 196]. The measurements extended up to 90° and the data displayed a complex oscillatory behaviour with periodic structures of different period at forward angles and those close to 90°. Even though refractive effects could not be easily identified in the data themselves, the conclusions of the optical model analysis were definite in the need for deep real potentials. As was shown years later [144], and will be discussed later here, the techniques of nearside/farside decomposition that were fully developed in the 1980s were indispensable in unravelling the refractive contributions from the diffractive contributions in these relatively low-energy data.

This system has continued to be of great interest and so far (until 1996), the elastic scattering has been measured for angles beyond the diffractive oscillations at laboratory energies of 140 and 159 [121], 240 [18], 289 [50], 300 [17], 360 [42], 1016 MeV [41] (superseding a previous measurement at 1030 MeV [40]), 1450 and 2400 MeV [85]. Fig. 6.1 shows some of the measurements. At 140 and 159 MeV, the differential cross sections were measured up to 90°, and it is possible to guess at the presence of broad Airy maxima (centred at ≈50° at 159 MeV and at ≈62° at 140 MeV), in between the Fraunhofer pattern at forward angles and the oscillations near 90° due to symmetrization. While the data at 240 and 289 MeV did not extend far enough to display the full extent of a nuclear rainbow, the measurements at 360 MeV show the beginning of the exponential falloff of the nuclear rainbow, distinctly evident in the angular distribution beyond $\theta_{cm} \approx 25°$. As E/A approaches 100 MeV and higher, the rainbow moves forward faster than the Fraunhofer oscillations, and the visual identification of its Airy minima in the angular distribution is less clear. Most of the individual optical model analyses of these data have been performed with phenomenological potentials, to which we refer in Section 6.4.

6.1.2. $^{16}O + ^{16}O$

In the 1970s, the elastic scattering excitation function of ^{16}O + ^{16}O was measured around 90° at laboratory energies between 70 and 180 MeV, revealing the presence of regularly spaced broad maxima [83]. The analysis of these data assumed phenomenological optical potentials having shallow real parts similar to those previously derived from lower energy data [194, 131]; these proved to be unable to describe the new observations.

All of the ^{16}O + ^{16}O elastic scattering measurements at intermediate energies, near or above $E/A = 10$ MeV, have been made quite recently either by Bohlen or by Sugiyama, and their colleagues. Very complete and precise measurements exist at laboratory energies of 124 [120], 145 [200, 120], 250 [101], 350 [198, 199], 480 [103] and 704 MeV [12]. These data are a remarkable achievement, involving cross sections as small as 10^{-5} of the Rutherford values. The data below 350 MeV extend up to 90°, displaying the typical Fraunhofer oscillations at forward angles and the symmetrization interference near 90°, with gross structures in between which one could surmise are due to Airy maxima and minima. At 350 MeV and above, an Airy minimum followed by its maximum becomes evident (in a remarkable way at 43° at 350 MeV; see Fig. 2.3) as the diffractive structure moves forward like $1/\sqrt{E}$, while the refractive interference moves forward approximately as $1/E$. The symmetrization oscillations near 90° are left behind.

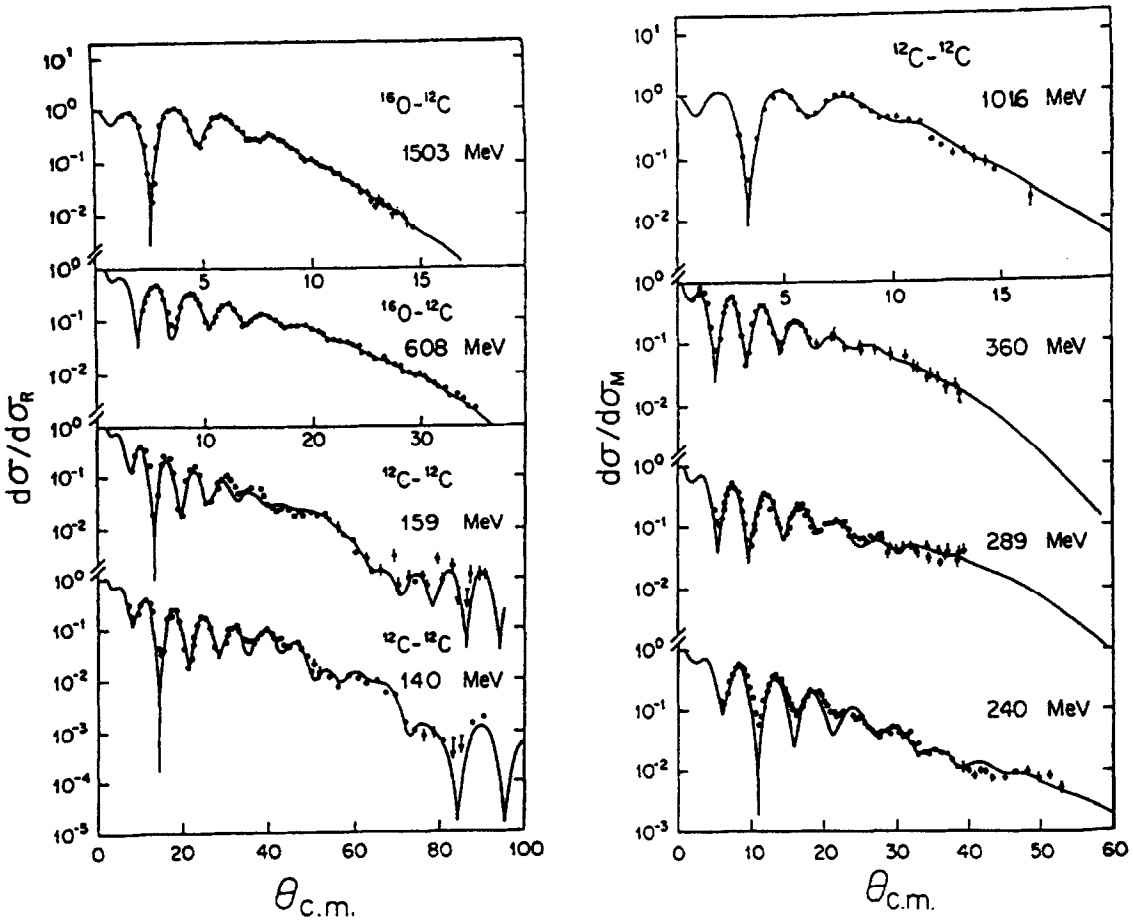

Fig. 6.1. Elastic scattering angular distributions (relative to Rutherford or Mott cross section) for $^{16}O + ^{12}C$ and $^{12}C + ^{12}C$. The curves are calculations with phenomenological potentials given in Table 6.2 (from [27]).

The system $^{16}O + ^{16}O$ is at present the light heavy-ion system for which the most complete elastic scattering angular distributions are known. It is the one that has been subjected to the most numerous and detailed analyses in the last few years and is likely to continue in this role.

6.1.3. $^{16}O + ^{12}C$

The data for this system are neither as numerous nor complete as for the identical systems $^{12}C + ^{12}C$ or $^{16}O + ^{16}O$. Elastic scattering data have been obtained at 139, 216 and 311 MeV [21], 608 [26] and 1503 MeV [175]. The cases at the lowest three energies were not measured far enough in angle to establish the presence of refractive minima or maxima. Fig. 6.1 presents the data at the two highest energies. The results at 608 MeV, that show beyond 18° the structureless falloff which can be attributed to farside dominance, have been extensively analysed and interpreted, and will be referred to later. At 1503 MeV, the Airy structures have moved forward in angle to be superimposed

on the Fraunhofer oscillations; these data have also been the subject of thorough analyses which will be discussed below.

6.1.4. ^{6}Li scattering

The elastic scattering of ^{6}Li has been extensively studied with bombarding energies below 50 MeV [47], and at a few higher energies for several targets: ^{28}Si at 135 [58] and 154 MeV [192], ^{6}Li and ^{40}Ca at 156 MeV [147,52] and ^{14}C at 93 MeV [61]. The target ^{12}C is the most consistently studied, at $E/A = 10$ [16], 16.5 [193] and 26 [52] MeV. A systematic study [154–156] at $E/A = 35$ and 53 MeV of ^{6}Li scattered off ^{12}C and ^{28}Si (and ^{40}Ca, ^{58}Ni, ^{90}Zr and ^{208}Pb at the lower energy) has been performed recently at the National Superconducting Cyclotron Laboratory at MSU. These data, which consisted of cross sections extending down to between 1 and 10 μb/sr, showed the diffractive oscillations to be followed by the exponential falloff of a nuclear rainbow. Thus the experiment permitted the clear observation of refractive effects in the angular distributions for all but the ^{208}Pb targets and analysis was able to determine the potential depths unambiguously. For the lightest targets, the "hump" of the first Airy maximum could be seen in the data.

6.1.5. Other light systems

The elastic scattering has been measured at intermediate energies in many light heavy-ion systems other than the ones already discussed, but in such cases data only exist at a few, sometimes single energies, and the measurements are rather limited in angle, not reaching into regions where refractive effects might appear to their full extent.

Elastic scattering of ^{7}Li off ^{12}C, ^{48}Ca, ^{58}Ni and ^{208}Pb has been measured at a few energies between about 60 and 150 MeV [96,119,197]. In general, these measurements do not extend to sufficiently large angles to observe the disappearance of Fraunhofer oscillations and the possible presence of farside dominance. Recently, the scattering of $E/A = 50$ MeV ^{7}Li+ ^{12}C and ^{28}Si has been measured with great completeness [157]. The data show very clearly the structureless falloff of the cross section beyond about 15° and up to 40°; this feature permits the determination of "unique" potentials solving the discrete ambiguities encountered in previous analyses.

The systems ^{9}Be + ^{12}C, ^{16}O have been studied at $E/A \approx 18$ MeV [183]. Following the Fraunhofer oscillations, the angular distributions show a change of slope followed by a featureless flat region up to the last point that was measured (at about 60°); the description of the data by phenomenological potentials required "refractive" potentials, i.e. deep real parts accompanied by an imaginary term much weaker than the real at small radii. The analysis [183] interpreted the feature at 60° as a weak primary Airy minimum. Since it was strongly damped and scarcely visible, it was referred to as an Airy "ghost".

A measurement [18] of ^{13}C + ^{12}C at E/A equal to 20 MeV showed features similar to those of ^{12}C + ^{12}C at the same E/A. A hint of an Airy minimum was observed in the data and the optical model analysis (phenomenological and folding model using DDM3Y) required potentials similar to those obtained in the systematic study of ^{12}C + ^{12}C.

A beam of ^{14}N at $E/A = 20$ MeV was used to study the scattering off ^{12}C [31]. As in other cases in this energy range, the data displayed the transition between Fraunhofer oscillations and a structureless angular region at larger angles. The results of the optical model analysis were not conclusive, allowing descriptions with either weakly or strongly absorbing potentials.

All systems mentioned so far in Section 6 display in their angular distributions refractive features which range from dominance of farside scattering up to clear signatures of a nuclear rainbow. The main difference among the potentials describing them is the magnitude of the absorption in

the internal region, but, without exception, all these systems allow an interpretation in terms of a weakly absorbing nuclear potential. The system $^{12}C + {}^{20}Ne$ is the lightest system for which data exist at intermediate energies (one set of elastic scattering measurements at $E/A = 20$ MeV [19]) and where a description in terms of a weakly absorbing potential has not been possible. Even though the general appearance of the data is similar to that often described in this section (i.e. Fraunhofer oscillations followed by a rather flat cross section beyond), the original analysis and later attempts to describe the measurements with a weakly absorbing potential have failed.

At $E/A = 94$ MeV, Roussel et al. [175–177] measured the ^{16}O elastic scattering on a variety of targets ranging from ^{12}C, to which we have referred already, up to ^{208}Pb. The $^{16}O + {}^{12}C$ and ^{28}Si scattering were clearly dominated by farside contributions but a phenomenological potential could only be well determined for the lightest target. The measurements for ^{40}Ca, ^{90}Zr and ^{208}Pb were mostly sensitive to the potential in regions about 1–2 fm inside the strong absorption radii.

6.2. Optical model analyses

Elastic scattering angular distribution data are analysed by comparing them to optical model calculations performed using a computer program (PTOLEMY [132] and ECIS [170] are the most commonly used ones for heavy-ion systems). The nuclear complex potential is entered into the code as an input, either point by point or through the parameters of a standard analytical expression. If the analysis assumes a microscopic real part, i.e. it is a *folding model* analysis, the calculated values of $V(r)$ at certain radii are entered, and the code searches on the value of the overall normalization, N, in order to optimize the fit to the data. For the imaginary part, the folding model analyses usually assume a parameterized form, either with the Woods–Saxon (WS) shape raised to some power n (most often $n = 1$), $(WS)^n$, the surface-peaked derivative of the WS form factor (WSD), or a combination of them; the optical model code searches to find the parameter values which optimize the agreement with the data. If the analysis is *phenomenological*, the real and the imaginary part are assumed to have WS, $(WS)^n$ or WSD shapes, or some combination, and all the potential parameters can be searched on. Generally, the goodness of fit is quantified via the χ^2 expression,

$$\chi^2 = \frac{1}{N_\sigma} \sum_{i=1}^{N_\sigma} \frac{(\sigma_{th} - \sigma_{ex})^2}{(\Delta\sigma_{ex})^2}, \tag{6.1}$$

where σ_{th}, σ_{ex}, and $\Delta\sigma_{ex}$ are the theoretical cross sections, experimental cross sections, and uncertainties in the experimental cross sections, respectively. N_σ is the total number of angles at which measurements were made. (Note that N_σ is *not* the number of degrees of freedom N_F, where $N_F = N_\sigma - N_p$ and N_p is the number of parameters varied. N_F and N_σ may differ significantly when the number of parameters becomes large, as for example when using "model independent" potentials defined in terms of splines or Fourier–Bessel series.)

6.3. Applications of the folding model

The 1979 review by Satchler and Love [181] presented the successful application of real potentials calculated via double folding techniques, supplemented by WS imaginary potentials, to "typical" heavy-ion data available up to that date. The effective interaction used was the M3Y of Eq. (5.13), based on a G-matrix constructed from the Reid potential, together with the zero-range pseudopotential (5.17) to account for the knock-on exchange.

6.3.1. $^{12}C + ^{12}C$ scattering

An earlier analysis of $^{12}C + ^{12}C$ [206, 196] at E/A between 6 and 10 MeV had used an essentially equivalent interaction. The resulting folded potential had a depth of about 450 MeV at the centre. The data could be described remarkably well. The required potential renormalizations N were close to unity and only weakly dependent upon the energy. The main conclusion drawn from this analysis was the need for real potentials that were much deeper, at regions near 4–6 fm, than the shallow potentials originally assumed from the fits made to data at much lower energies. The scattering at large angles (up to 90°) was shown to be sensitive to a notch in the real potential centred at radii as small as ≈2 fm, suggesting that the data contained some information about the potential even at such a small internuclear separation. However, an independent work [174] showed that, in spite of the sensitivity to the deeper regions of the potential, discrete ambiguities in the determination of the real part still remained.

An early global analysis [23] of data at the higher energies of 161, 289 [50] and 1030 MeV [40] used an energy-independent microscopic real potential, 380 MeV deep at the centre and calculated with the same effective interaction as in [196]. This work suggested the presence of nuclear rainbow scattering in the $^{12}C + ^{12}C$ system. The claim was based on the overall characteristics of the three sets of data which, when plotted as a function of the parameter $\varepsilon = \theta_{cm}E_{cm}$, showed the structureless falloff that follows a nuclear rainbow at an approximately constant value of ε. This unification of the refractive effects in an angular distribution, valid for a given potential, had been predicted by Knoll and Schaeffer [107]. The renormalization constant N needed to fit the data was found to be energy-dependent, decreasing from about unity at 10 MeV per nucleon to about 0.5 at $E/A = 85$ MeV. The imaginary potential required was found to be weaker than the real one over most of the radial region, a condition that appears to be necessary for the manifestation of refractive scattering. More complete data, however, were needed to definitively establish the presence of this refractive effect.

Even though the analysis in [23] reported sensitivity of the data to the potentials in regions appreciably inside the strong absorption radius, and the need for a very attractive real part which located the rainbow angle in approximately the region where the angular distribution started to fall exponentially, the imaginary term was, in general, about 50 MeV at the centre, probably too strong to permit the observation of the Airy interference essential for the identification of a rainbow. In other words, the data did not necessarily show the clear signs of an Airy minimum, but only the dominance of the farside component in the scattering amplitude. This fact was stressed by McVoy and Satchler [143], who showed that the mechanism producing the exponential falloff in the optical model analyses was the absorption combined with sufficient attraction in the nuclear surface, and not necessarily the dark side of a rainbow. The 240 MeV data measured by Bohlen et al. [18] displayed, for the first time in $^{12}C + ^{12}C$ above 10 MeV/nucleon, a hint of the rise that follows an Airy minimum. The analysis [18], with phenomenological potentials, required relatively weak absorption, $W \approx 22$ MeV at the centre.

6.3.2. Folding with density-dependent interactions

The need for a density dependence in the effective interactions used in folding techniques for heavy-ion potentials at energies close to $E/A = 10$ MeV had been anticipated by Love [130]; over-estimations of 32% in the magnitude of the $^{12}C + ^{12}C$ potential at the strong absorption radius and 76% at $r \approx 0$ could arise if the density-dependence was ignored. Analyses of elastic and inelastic α-particle scattering had been made using a *density-dependent* form of the M3Y interaction [109, 110].

These showed the need for weakening $V(r)$ in the interior for alpha energies above about 100 MeV, where the observations of a nuclear rainbow imposed severe constraints on the internal values of the real potential (see Fig. 5.2). This density-dependent interaction was the DDM3Y of Eq. (5.23), a generalization of the M3Y to have an explicit dependence on the nuclear density that was normalized to the G-matrix calculations of [95] (see Section 5.6.1). The effect of this requirement is to weaken the interaction as the density increases, and results in folded potentials which are less deep near the centre, where the two nuclei overlap strongly, than those calculated from the M3Y force. The applications to α-particle scattering consistently required renormalization factors of $N \approx 1.3$. Folding model analyses using DDM3Y were first applied to a variety of heavy-ion data [64]; the renormalization factors that emerged in that case tended to be *less* rather than greater than unity.

A thorough analysis, using DDM3Y folded potentials, of the recently measured $^{12}C + {}^{12}C$, $^{16}O + {}^{12}C$ and $^{13}C + {}^{12}C$ at energies above $E/A \approx 10$ MeV soon followed [28]. The data thus analysed comprised 13 sets at E/A between 9 and 120 MeV. The imaginary parts of the potential were assumed to have the Woods–Saxon shape (with $n = 1$). Reasonably good fits were obtained at all energies with renormalizations N close to unity, ranging between 0.83 and 1.27, and averaging 1.0 ± 0.1. The value of the real potential at the centre varied from about 250 MeV at $E/A \approx 10$ MeV down to about 100 MeV at $E/A \approx 100$ MeV. Thus, the variation by more than a factor of two in this energy range could be accounted for by the intrinsic energy-dependence of DDM3Y that arose from its normalization to the G-matrix of [95]. This is in contrast to the original, bare M3Y interaction that contains very little energy-dependence. The imaginary parts were more weakly absorptive than had been found in the previous work with M3Y [23], having central depths between about 25 MeV (at $E/A \approx 10$ MeV) and about 15 MeV (at $E/A \approx 100$ MeV). The reduced imaginary radius could be held at a fixed value of $r_{i0} = 1.13$ fm at all energies except $E/A = 120$ MeV (where it was 1.21 fm), without deterioration in the quality of the fit.

A global microscopic analysis using the same DDM3Y interaction applied to $^{12}C + {}^{12}C$ data which included the angular distributions measured by Stokstad at lower energies, did extend these results down to $E/A \approx 6$ MeV [30]. The renormalization N required for the folded real potential was about 1.1 below $E/A = 10$ MeV, slowly decreasing to about 1.0 at $E/A = 120$ MeV. The parameters describing the WS imaginary part displayed a smooth energy dependence. Solid symbols in Fig. 6.2 show the values of the real renormalization parameter N for energies E/A up to 24 MeV. The values represented by the empty symbols are explained in Section 7.2.

The $^{16}O + {}^{16}O$ data at 350 MeV have also been analysed using DDM3Y real folded potentials [33]. The fits were very successful, and required a value of N equal to 1.08; it appears that the imaginary part for this system must include a Woods–Saxon derivative term which peaks near the surface, in addition to the volume term, in order to optimize the fits, whenever a monotonic real part (such as the DDM3Y potential) is used.

In spite of the apparent success of the potentials calculated with the DDM3Y effective interaction in the description of data for α-particle scattering (except for the need for $N \approx 1.3$), and for $^{12}C + {}^{12}C$, $^{16}O + {}^{16}O$, and $^{16}O + {}^{12}C$, both over a wide energy range, the question of the appropriateness of this interaction as an approximation to the NN interaction in the nuclear medium has been pursued further by Khoa and his collaborators [100–103]. They use the same M3Y form, (5.13) or (5.14), but explored the use of a more realistic power-law density-dependence (that in Eq. (5.25)), instead of the exponential dependence (5.20) used in the original DDM3Y model. In addition, they employ a better approximation to the knock-on exchange term that takes account of the finite range of the

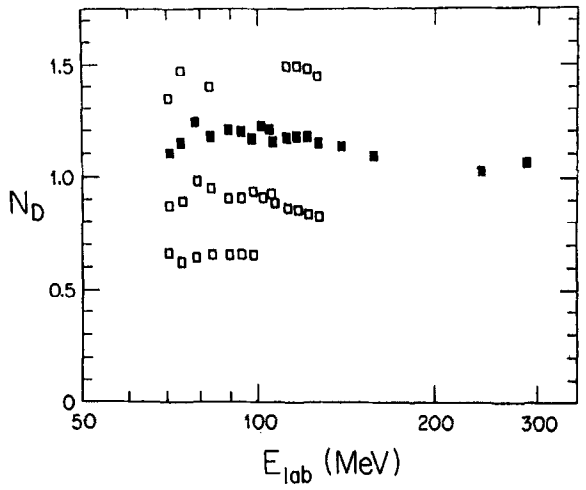

Fig. 6.2. Values of the real potential renormalization which give mimimum χ^2 in the folding model analysis of $^{12}C + ^{12}C$. The effective interaction was the original DDM3Y. The solid symbols indicate the family of solutions which gives a "continuous" description in the complete energy interval (from [30]).

interaction: see Section 5.6.2. The parameters C and α of the power-law density-dependence (5.5) were tuned to reproduce the saturation density and binding energy of normal nuclear matter for each value of the power β [100, 101]. These were called the BDM3Yn interactions, with $n = 0$–3 denoting the power of beta used. In addition, the C, α and β of the exponential form (5.20) were also modified to satisfy the saturation conditions (which the original DDM3Y does not). This was called the DDM3Y1 interaction. These parameter values were not allowed to vary with energy (contrary to the original DDM3Y: see Fig. 5.4).

These new interactions were applied to describe $^{12}C + ^{12}C$, $^{16}O + ^{12}C$, and $^{16}O + ^{16}O$ data at E/A above 10 MeV [100, 101]. All the folding model potentials thus obtained give good agreement with the data at forward angles, which correspond to scattering trajectories that only experience the surface of the potential. This is illustrated by the lower part of Fig. 6.3, which shows the scattering for two of the $^{12}C + ^{12}C$ energies. However, differences appear at the larger angles fed by trajectories which experience the inner parts of the potential. These differences allow us to select the most appropriate among the interactions. This is important, since each corresponds to a different value of the incompressibility of nuclear matter, and provides evidence of the value of this quantity. . The two studies [100, 101] strongly favoured the DDM3Y1 or BDM3Y1 interactions, implying a fairly soft equation of state for nuclear matter.

The renormalization factors N needed for the DDM3Y1 and BDM3Y1 interactions were found to be energy-independent, averaging 0.92 ± 0.05, and 0.93 ± 0.05, respectively, for the 12 data sets analysed. The optimum imaginary potentials have features similar to those found in previous folding model or phenomenological analyses.

Later, the "generalized" folding model of Khoa was applied to study the scattering of $^{16}O + ^{16}O$ at four energies, 145, 250, 350 and 480 MeV, using the Paris version (5.16) of the interaction [103]. Fig. 6.4 shows the different potentials at a single energy. The potentials agree in the surface region and, as was the case with the Reid version, they differ for the largest values of the density, i.e. for

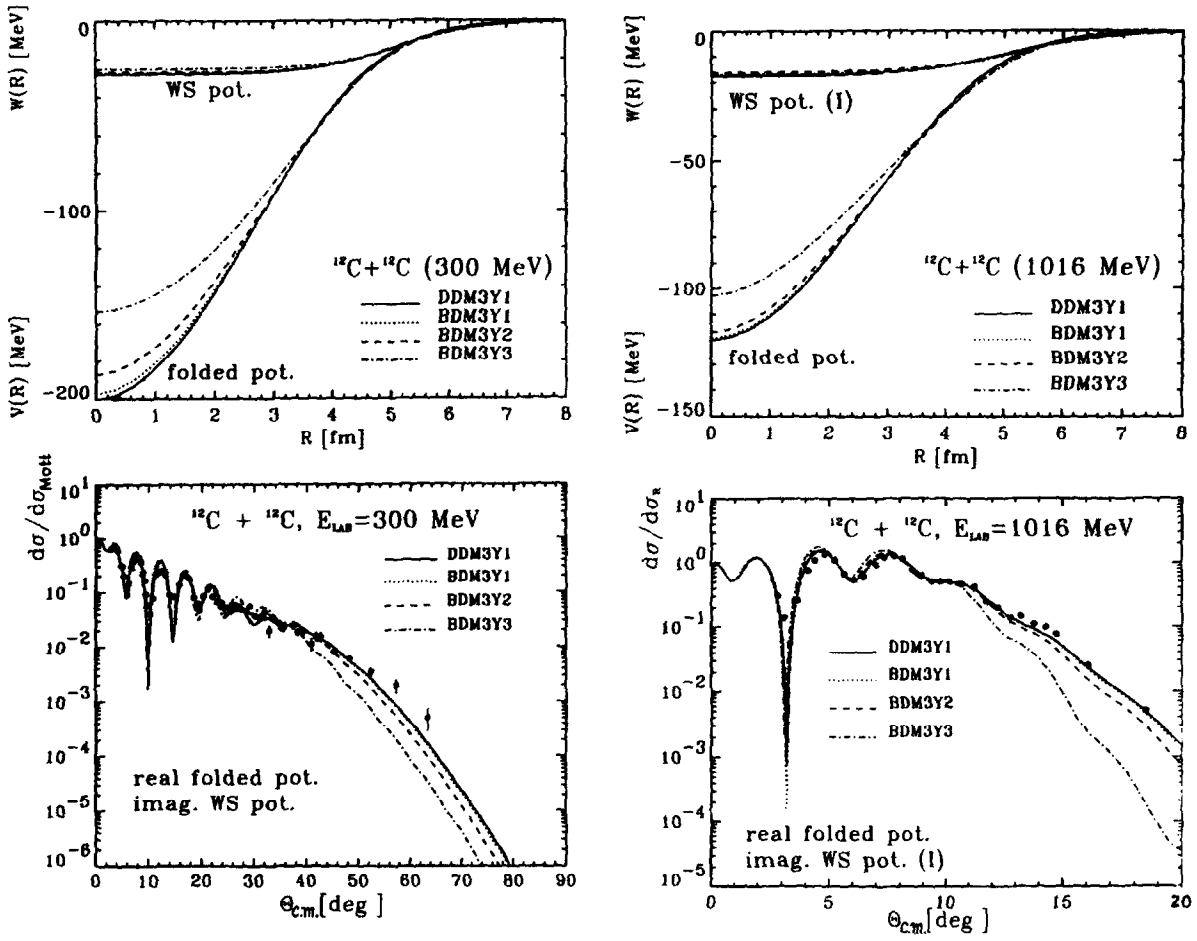

Fig. 6.3. Fits to $^{12}C+^{12}C$ elastic scattering data (lower part) given by folding model real parts (upper part) calculated with different density-dependent effective interactions (from [101]).

the smallest internuclear distances. Fig. 6.5 shows the fits to the $^{16}O+^{16}O$ data: again, the interactions DDM3Y1 and BDM3Y1 are the preferred ones. The renormalization N needed appears to be slightly energy-dependent, going from 0.90 (0.93) at $E/A = 8$ MeV to 0.82 (0.83) at 30 MeV/nucleon, for interaction DDM3Y1 (BDM3Y1). This effect might be due to the opening of inelastic channels as the energy increases [103].

Finally, we should note that the application of these interactions to the scattering of α-particles gave similar results; the rainbow data at large scattering angles established the DDM3Y1 or BDM3Y1 interactions as the physically correct ones [102], but still the α-particle data required renormalization factors N a little larger than unity.

6.3.3. Folding model for the scattering of ^{6}Li

A distinguishing feature of the analyses of ^{6}Li elastic scattering at the lower energies was the "failure" of the folding model, meaning that the attractive, real folded potential obtained using the

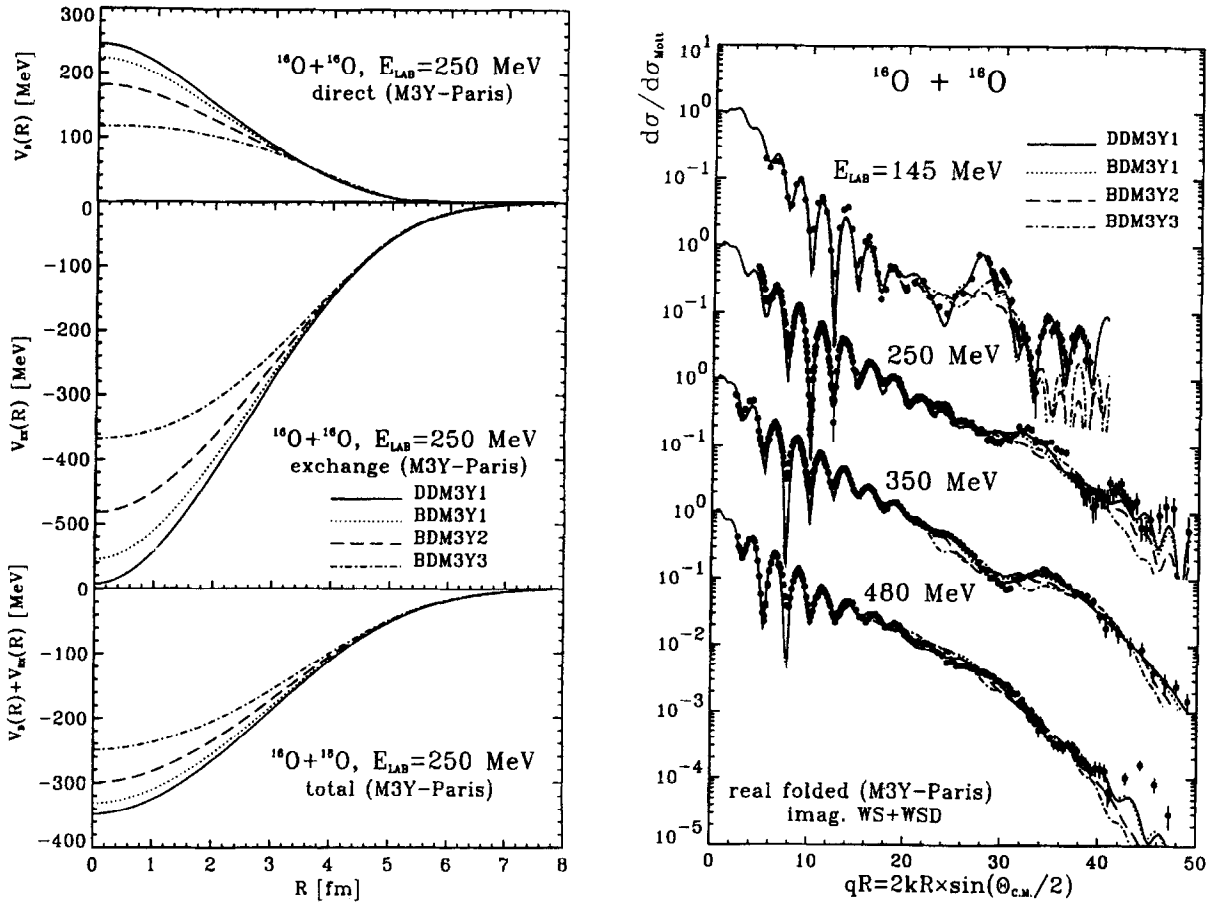

Fig. 6.4. Direct and exchange parts of the total $^{16}O+^{16}O$ folded potentials calculated using different density-dependent interactions (from [103]).

Fig. 6.5. Data and fits to $^{16}O+^{16}O$ elastic scattering measurements at various energies. The optimum fits are those given by the DDM3Y1 and BDM3Y1 real parts. The varaible q is the linear momentum transfer (from [103]).

M3Y interaction (5.13) and (5.17) was too strong and needed to be renormalized by factors typically of $N\sim 0.6$. This was ascribed to the effects of break-up, as discussed in Section 5.8. However, when the more definitive data became available for $^{6}Li + ^{12}C$ and ^{28}Si at $E/A = 35$ and 53 MeV, which allowed a less ambiguous determination of the potential family, it was claimed [156] that they were consistent with the M3Y interaction *without* the considerable renormalization found necessary at lower energies. This result was somewhat surprising because estimates of the break-up effects [185] had indicated that they should still be sizable at these energies.

Upon reanalysis of the ^{12}C data [189], two factors were found to account for the conclusions of [156]. One was that the *optimum* fit to the data (the one to give the lowest χ^2) does require a significant renormalization. The other was that a prescription [78, 53] was used for the strength of the knock-on exchange term in (5.7) that differs appreciably from that of (5.17). The latter has been

regarded as part of the conventional "M3Y model". When the conventional term (5.17) is used, the ^{12}C data at both these energies required a renormalization of the folded potential by $N \sim 0.7$ to obtain the minimum χ^2. Furthermore, a much weaker energy-dependence is predicted for the potential than was deduced in [156].

Later, any argument about which prescription for the strength of the knock-on term was more correct was avoided by using two versions (the DDM3Y1 and the BDM3Y1 based upon the Reid nucleon–nucleon force) of the density-dependent interaction of Khoa, described in Section 5.6.2. This includes an explicit treatment of the knock-on exchange which does not make any zero-range approximation.

These two more realistic interactions gave almost indistinguishable fits to the ^{6}Li + ^{12}C data at $E/A = 35$ and 53 MeV, with renormalization factors a little closer to unity, but with larger χ^2 values than obtained with the original, but renormalized, M3Y interaction. Similar increases in χ^2 were found for other ^{6}Li + ^{12}C data sets at the lower energies of $E/A = 10, 16.5$ and 26 MeV. This was taken to indicate that simply renormalizing the folded potential was not adequate to compensate for the polarization potential due to break-up (Section 5.8); some shape changes had to be taken into account.

To do this, a correction term $\Delta V(r)$ was added to the folded (DDM3Y1 or BDM3Y1) real potential. This $\Delta V(r)$ was defined by its values at certain radial knots in the region $1 < r < 8$ fm, with a cubic spline interpolation between the knots. The values at the knots, together with the imaginary potential parameters, were then adjusted to optimize the fit. The renormalization factor N for the folded potential was kept fixed at unity. Large reductions in χ^2 were obtained in this way at all the energies considered, compared to the use of the renormalized "bare" folded potential. Furthermore, the resulting $\Delta V(r)$ potentials had the characteristic expected for the real polarization potentials due to break-up [185], namely they are repulsive in the surface region, with radii around 4–5 fm, and small elsewhere. Two examples are shown in Fig. 6.6. The largest effects were found at $E/A = 16.5$ MeV, where the total real potential in the surface was reduced by about 40%. At $E/A = 35$ and 53 MeV, the reduction was about 13%. Thus the result in this surface region is to reduce the strength of the total real potential by the same amount as was found necessary when simply renormalizing the "bare" folded potentials (as in Fig. 5.9), but at the same time leaving the strength unchanged at smaller radii. It is in this way that greatly improved fits to the data were obtained.

By successfully explaining a case which at first seemed anomalous, these studies further reinforce the conclusion that the density-dependent DDM3Y1 or BDM3Y1 interactions are promising candidates for use in folding models, including their treatment of the knock-on exchange contributions.

6.4. *Phenomenological potentials*

Phenomenological analyses of the data that concern us were attempted almost simultaneously with the folding model descriptions. One has to remember that the seminal studies of α-particle scattering which gave rise to the concept of refractive effects in nuclear elastic scattering were done using phenomenological potentials. Goldberg, in the 1970s, discovered that, if the exponential falloff following the nuclear rainbow was present in the data, the potential could be determined without the cumbersome discrete ambiguities that had plagued analyses of data which did not display the full rainbow structure [75]. These studies were usually made with WS ($n = 1$) type potentials, although

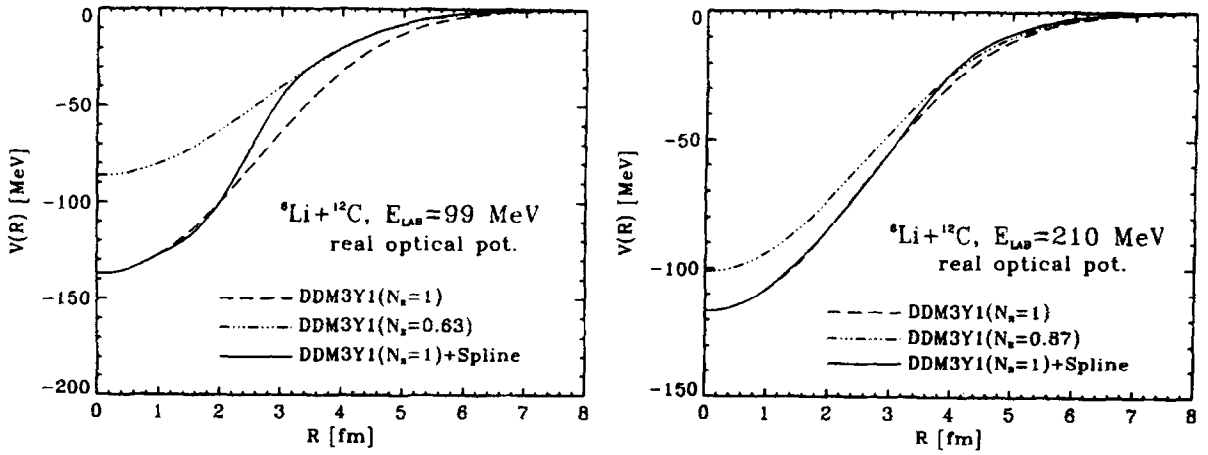

Fig. 6.6. Examples of potentials (solid curves) which fit ^{6}Li + ^{12}C scattering, each of which consists of a folded potential generated from the DDM3Y1 interaction (dashed curves) plus a spline correction term. Also shown (dot-dashed curves) are the folded potentials alone, renormalized by the factor N_R to optimize the fit to the data (from [104]).

Table 2
Optical model parameters[a] for ^{6}Li scattering

Target	E_{lab} (MeV)	V_0 (MeV)	R_V (fm)	a_V (fm)	W_0 (MeV)	R_W (fm)	a_W (fm)	J_V (MeV fm^3)	J_W (MeV fm^3)	Ref.
^{12}C	210	113.5	2.988	0.793	34.2	3.851	0.784	298	160	[155]
^{28}Si	210	125.2	3.945	0.836	31.4	5.171	0.822	276	135	[155]
^{40}Ca	210	145.2	4.313	0.868	31.1	5.797	0.811	284	130	[155]
^{58}Ni	210	174.5	4.397	0.907	32.0	6.220	0.806	253	108	[155]
^{90}Zr	210	170.0	5.297	0.939	31.3	7.291	0.810	257	105	[155]
^{208}Pb	210	224.0	6.541	1.001	35.1	9.640	0.824	258	92	[155]
^{12}C	318	126.9	2.601	0.897	29.3	3.881	0.878	285	150	[156]
^{28}Si	318	117.6	3.923	0.874	40.6	4.843	0.772	264	141	[156]

[a]Woods–Saxon potentials, defined by $U(r) = -V_0 f(x_V)^{v_R} - iW_0 f(x_W)^{v_I} + i4a_D W_D \, df(x_D)/dx$, where $f(x) = (\exp(x)+1)^{-1}$, and $x_i = (r - R_i)/a_i$. For this Table, $v_R = v_I = 1$.

the shape of a folded potential is closer to a WS with $n = 2$. Indeed, Goldberg pointed out [77] that potentials with a WS^2 shape gave slightly better fits to the α-particle data.

The analyses of ^{6}Li scattering by light targets at energies below ~100 MeV resulted in many real potential families, with depths discretely different from each other by certain amounts [51]. However, at $E/A = 35$ and 53 MeV the nuclear rainbow falloff was clearly observed and "unique" potentials free from these discrete ambiguities could be determined [154–156]. The ^{6}Li + ^{12}C, ^{28}Si data, analysed with potentials of Woods–Saxon form (no need for a Woods–Saxon-derivative imaginary term was found), required strongly attractive real parts ($V_0 \approx 110 - 130$ MeV) and a relatively weak imaginary term ($W_0 \approx 30$–40 MeV). Table 2 includes potential parameters for ^{6}Li scattering. The extrapolation of these potentials towards lower energies, assuming a logarithmic energy dependence for the real

Table 3
Optical model parameters for ^{12}C and ^{16}O scattering

E_{lab} (MeV)	v_R	v_I	V_0 (MeV)	R_V (fm)	a_V (fm)	W_0 (MeV)	R_W (fm)	a_W (fm)	W_D (MeV)	R_D (fm)	a_D (fm)	J_V (MeV fm^3)	J_W (MeV fm^3)	Ref.
$^{12}C+^{12}C$														
78.9	1	1	312	2.66	0.852	9.17	6.41	0.324	0.			342	72.3	[30]
102.1	1	1	284	2.75	0.903	14.2	5.49	0.590	0.			351	76.2	[30]
121.6	1	1	287	2.61	0.970	17.0	5.49	0.601	0.			351	91.5	[30]
139.5	1	1	250	2.86	0.900	17.3	5.60	0.485	0.			337	95.1	[27]
158.8	1	1	200	3.22	0.870	25.0	5.08	0.717	0.			334	114	[27]
240.0	1	1	175	3.31	0.839	27.0	5.17	0.650	0.			302	125	[27]
288.6	1	1	175	3.07	0.955	22.0	5.33	0.663	0.			288	111	[27]
360.0	1	1	175	2.87	0.894	25.0	4.87	0.645	0.			235	98.4	[27]
1016	1	1	120	3.01	0.879	25.0	4.41	0.862	0.			175	86.0	[27]
$^{16}O+^{12}C$														
139.2	1	1	275	3.45	0.747	15.0	6.23	0.436	0.			360	82.8	[27]
215.8	1	1	175	3.78	0.849	25.0	5.55	0.601	0.			308	104	[27]
311.4	1	1	175	3.82	0.846	25.0	5.69	0.643	0.			317	113	[27]
608	1	1	175	3.15	0.975	24.7	5.21	0.662	0.			232	88.5	[27]
1503	1	1	80	4.24	0.763	23.1	5.07	0.825	0.			175	82.7	[27]
$^{16}O+^{16}O$														
124	2	2	413	3.97	1.53	16.0	6.86	0.970	0.			337	62.9	[120]
145	2	2	414	3.95	1.49	16.8	6.80	0.883	0.			329	65.2	[120]
350	2	2	400	3.80	1.60	29.7	6.27	1.02	7.63	4.62	0.321	298	98.2	[33]
480	2	2	401	4.17	1.25	51.2	5.43	1.31	9.0[a]	5.17	0.62	250	120	[12]
704	2	2	269	4.41	1.35	53.6	5.50	0.70	2.1[a]	6.34	0.68	280	140	[12]

[a]The surface absorption is assumed to have the shape of the derivative of a $(WS)^2$ form.

part, was suggested as a possible way of selecting among the many solutions that had been found in previous individual analyses. However, a subsequent analysis of the scattering from ^{12}C at these and lower energies [104] has indicated a different, much weaker, energy dependence below $E/A = 25$ MeV (see Section 6.3.3).

The analysis of the $^{7}Li + ^{12}C$ and ^{28}Si measurements at $E/A = 50$ MeV [157] determined Woods–Saxon potentials which are included in Table 2. They are similar to those for the scattering of ^{6}Li at $E/A = 53$ MeV on the same targets. The volume integrals per interacting pair for the two isotopes differ by less than 3% at these two energies.

The [27] global analysis of the then available $^{12}C + ^{12}C$ and $^{16}O + ^{12}C$ elastic scattering data for $10 \leq E/A \leq 100$ MeV assumed WS form factors for both the real and imaginary parts of the potentials. This study concluded that, in order to obtain a consistent description of all the data with a potential whose real and imaginary parts were smooth functions of the energy, the imaginary part *had* to be weakly absorptive. The values of the central absorption ranged between 15 and 27 MeV. The central part was strongly attractive, with $80 \leq V_0 \leq 275$ MeV. The potential parameters from [27]

can be found in Table 3 and the results of the calculations are shown by the curves in Fig. 6.1. It must be pointed out that in [27] the data at 139.5, 158.8, 608 and 1503 MeV were fitted first, thus determining their optimum potential parameters, and the parameters for the other energies were interpolated from these. The most severe constraints on the determination of the potentials in this study came from fitting the 140 and 159 MeV data, whose complicated angular distributions, which contain both Fraunhofer and symmetrization interferences superimposed on broad Airy maxima and minima, could only be reproduced with potentials of the type already described.

The $^{16}O + {}^{16}O$ data have been analysed phenomenologically by many authors, in many ways. In general, for the best fits, this system requires an imaginary part composed of a volume plus a surface term, while the real part has been assumed to have either a WS or a WS^2 form factor. Table 3 contains some of the potential parameters reported. These potentials share the main features already determined for similar light heavy-ion systems, that is a strong real part and a weak absorption. In Table 3 we have selected those potentials that correspond to the so-called family A in [117] and type IV in [200, 120]. As discussed in [101], this is the phenomenological potential family that most closely agrees with the latest microscopic calculations, considering their volume integrals as well as their evolution as a function of incident energy. A discussion about the possible discrete ambiguities for this system can be found in Section 7.2.

6.5. *Volume integrals*

It has been known since many years ago that the volume integral of the nuclear potential may be much better determined by the data than the potential itself [182]. Even in cases of extreme sensitivity of the scattering to the potential, a small readjustment of the various parameters is possible, while keeping the integral a constant. This fact has been of particular relevance to the study of the interaction of light heavy-ions. The relatively weak absorption in these systems permits some sensitivity to the potential interior and therefore the volume integral obtained from fits to the scattering data contains some information from this region. As will be presented in detail in Section 7.2, the role that the volume integral plays as the representative of a given family of potentials has allowed the unambiguous results obtained at high energies, from measurements where the nuclear rainbow falloff and/or the Airy extrema are clearly visible, to be extrapolated towards the lower-energy regime. Alternatively, volume integrals suggested by molecular resonances at low energies have been used to help in selecting among possible potential families at higher energies. In the case of $^{16}O + {}^{16}O$, where both approaches have been used, the results have been internally consistent, as well as in agreement with the systematics observed in similar systems.

The (complex) volume integral of $U_E(r)$ per interacting nucleon pair, $J_U(E)$, is defined as

$$J_U(E) = -\frac{4\pi}{A_p A_t}\int U_E(r) r^2 \, \mathrm{d}r = J_V(E) + \mathrm{i} J_W(E)\,, \tag{6.2}$$

where A_p, A_t are the mass numbers of the projectile and target nuclei, respectively. The minus sign is introduced in the definition (6.2) so that J is positive for attractive (negative) potentials U_E. The value of the integral has been normalized by dividing by $A_p A_t$, the number of interacting pairs of projectile and target nucleons (compare with Eq. (5.3)). Then one would expect the real parts J_V for different systems to be similar if the folding model is valid. The density-dependence of the underlying nucleon–nucleon interaction would then have the consequence that J_V would slowly

become smaller as the ions became heavier (larger) and the weakening of the interior potential began to have relatively more effect on the integral.

At first sight, there is no obvious reason why the imaginary part J_W should show a corresponding independence of the system, except perhaps at high energy where the impulse approximation or Glauber theory begins to have some validity. Then the imaginary part of the potential could also be regarded as the expectation value of a sum of nucleon–nucleon terms [59, 163].

Fig. 6.7 shows the values of J_V and J_W for a variety of potentials that fit the $^{12}C+^{12}C$, $^{16}O+^{12}C$, and $^{16}O+^{16}O$ data discussed earlier in this chapter. Included in the figure are values from the phenomenological potentials in Table 3, from microscopic analyses using the DDM3Y effective interaction, and from recent analyses using Khoa's extended folding model formalism. As can be observed, in the first place, for a given system and energy, the different real potentials all have similar volume integrals per nucleon pair, in some cases being indistinguishable from each other. Secondly, the imaginary potential, which differs in parameterization from one study to the other (WS, WS^2, WSD or their combinations), seems to have its integral J_W even more accurately determined by the data than J_V. Thirdly, for a given E/A there is no substantial difference in J_V or J_W between the three systems, except for J_W being $\approx 20\%$ smaller for $^{16}O+^{16}O$ than $^{12}C+^{12}C$ or $^{16}O+^{12}C$. The relatively weak absorption in $^{16}O+^{16}O$ is probably associated with the doubly closed shell structure of the participating nuclei which reduces the number of open channels available [15]. This manifests itself in the exceptional displays of refractive effects in the elastic scattering for this system.

Phenomenological [154, 156] analyses of $^{6}Li+^{12}C$ have resulted in values for J_V ($\sim$300 and $\sim$285 MeV fm^3 at $E/A=35$ and 53, respectively) that are slightly larger than those for ^{12}C projectiles at the same E/A. The $J_W \sim 160$ and ~ 150 MeV fm^3 for ^{6}Li projectiles at $E/A=35$ and 53 MeV are significantly larger than those for ^{12}C or ^{16}O . We surmise that this reflects the effect of the breakup channels for reactions induced by ^{6}Li projectiles. Folding model analyses [104] gave similar results, although the J_V values were a few percent smaller. These were based upon the DDM3Y1 and BDM3Y1 interactions (with $N=1$), with a supplementary real spline term to represent the effects of coupling to the breakup channels (see Section 6.3.3).

The solid lines in Fig. 6.7 correspond to the application of the dispersion relations (Section 4.5) to the $^{12}C+^{12}C$ volume integrals. The J_W curve is a linear segment parameterization of the experimental values and the J_V curve is the predicted behaviour from expression (4.19). The agreement of the predictions with the values obtained from the optical model analyses is very good, and the conclusion can be drawn that the energy-dependence due to the underlying nonlocality in the potential is weak, since most of the observed energy dependence can be accounted for by the dispersion relation. Qualitatively, the energy-dependences of J_V and J_W observed in Fig. 6.7 are similar to the well known "threshold anomalies" at low energies for heavier systems which are caused by the rapid changes in the absorption as the inelastic channels open up near the Coulomb barrier. The Coulomb barrier is weak and ineffective for a light system like $^{12}C+^{12}C$, but at these energies which are well above the barrier, the evolution of the kinematic matching conditions affects the absorption into nonelastic channels, causing an increase, followed by a levelling off, and finally a weakening of the strength of W as the energy increases. This in turn produces the observed changes in the real part, as required by the dispersion relation.

Fig. 6.8 compares the real and imaginary volume integrals for the system $^{12}C+^{12}C$ with curves that represent J_V and J_W for protons and α-particles scattered off light targets. The proton J_V curve

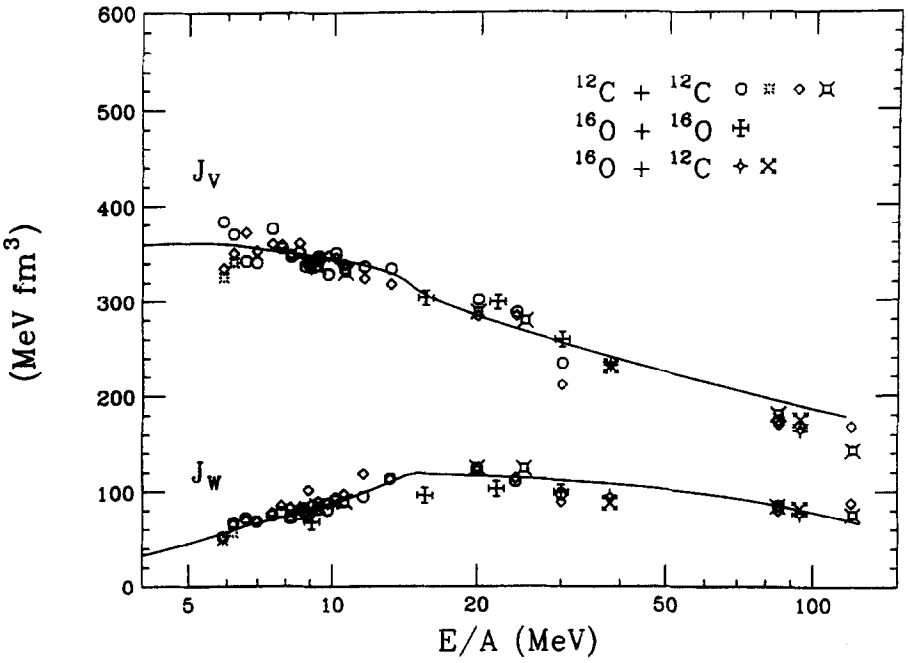

Fig. 6.7. Summary of real and imaginary volume integrals per interacting ion pair as a function of projectile energy per nucleon for three systems. The plotted values are results of various phenomenological and folding model analyses. The curves are dispersion relation predictions for $^{12}C + ^{12}C$ (from [36]).

is a linear parameterization of optical model results for scattering off ^{12}C [159], while the J_W curve represents an average behaviour for the same target [82]. The α-particle real and imaginary volume integrals come from global analyses of scattering by ^{16}O [148, 2]. Studies of α-particles scattered by many targets suggest that J_V should be similar for ^{12}C and ^{16}O, while J_W may be about 40% larger for ^{12}C than for ^{16}O [1]. The overall energy dependence of the real volume integrals is similar for all the represented systems, but there is a systematic decrease in J_V as the mass of the projectile increases up to ^{12}C. This is the behaviour anticipated above, arising from the density-dependence of the effective nucleon–nucleon interaction. It also agrees qualitatively with a phenomenological study of volume integrals for light ions [81].

On the other hand, the value of $J_W \approx 100$ MeV fm^3 reached by the light heavy-ions at intermediate energies is quite similar to those found for proton and α-particle scattering. This might indicate that the impulse approximation or Glauber view is becoming increasingly valid at these energies, so that the scattering can be regarded as a sum of individual nucleon–nucleon collisions. However, as [37] have discussed, the potential assumptions contained in the optical limit of the Glauber approximation strongly overestimate the degree of absorption in the nuclear interior and are in conflict with the systematic evidence obtained from the elastic scattering data (see Section 8). Then, the apparent success of the Glauber view both in the interpretation of imaginary volume integrals as well as in the total reaction cross section predictions to be presented in the following section, may be an indication of the insensitivity of these two calculations to the details of the imaginary potential in the internal region.

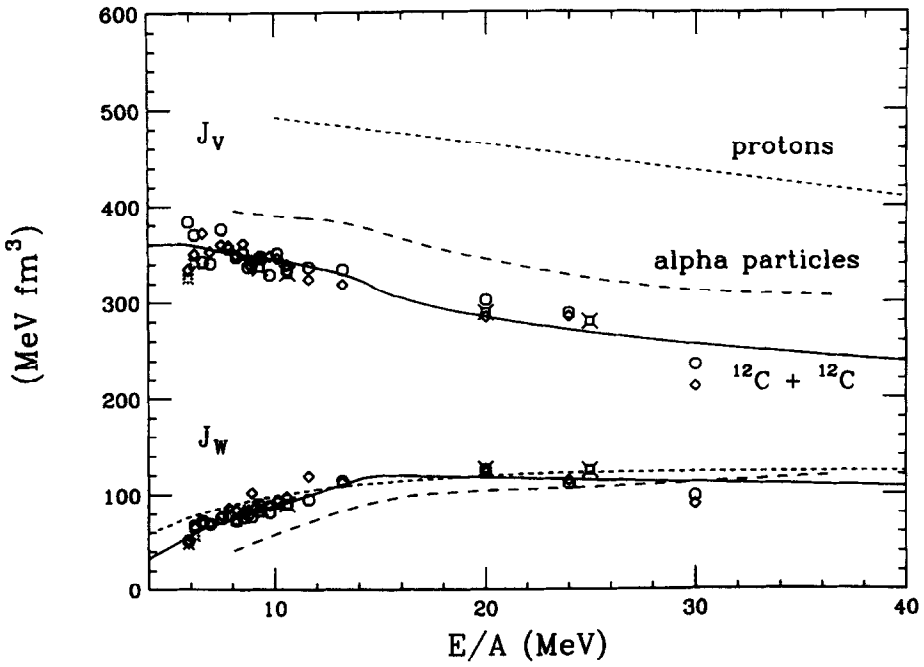

Fig. 6.8. Real and imaginary volume integrals per interacting ion pair for protons on ^{12}C, alpha particles on ^{16}O, and $^{12}C+^{12}C$. Short- and long-dashed curves represent results from phenomenological analyses for protons and alphas, respectively, and solid curves are the dispersion relation predictions for $^{12}C+^{12}C$ shown in Fig. 6.7. The symbols are phenomenological and folding model results for $^{12}C+^{12}C$.

The remarkably smooth behaviour of the volume integrals for light heavy-ions over a range of more than a factor of 10 in energy is one of the stronger arguments in favour of the description of this vast amount of data in terms of weakly absorptive and deeply attractive potentials that furnish a description of the angular distribution structures as the interplay of diffractive and refractive effects. Concerning the results for folded potentials included in Fig. 6.7, it must be recalled that these analyses have all required renormalizations of about unity, thus also implying that the density- and energy-dependence built into the effective interactions (DDM3Y, or the more recent DDM3Y1 and BDM3Y1) agree well with the energy dependence required by the data.

The results for J_V and J_W that have just been described indicate, on one hand, that real potentials calculated from a folding model, using a properly determined density- and energy-dependent interaction, reproduce remarkably well the main features of the scattering for these light heavy-ion systems, and on the other, that the imaginary potential does reflect somewhat the structure of the participating nuclei, requiring therefore a more elaborate microscopic description.

6.6. *Total reaction cross sections*

Studies of the total reaction cross section, σ_R, for heavy-ions has been an active field in the period covered by this review. Direct measurements were performed on a variety of systems [164, 111–113] over wide energy intervals, and in addition "experimental" values have been inferred from the phase

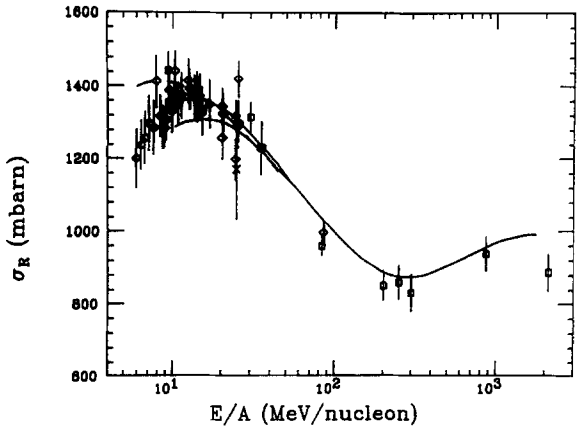

Fig. 6.9. Summary of total reaction cross section data for $^{12}C + ^{12}C$. The solid curves are microscopic calculations using deep (upper) and shallow (lower) real nuclear potentials (from [186]).

shifts obtained from optical model analyses of elastic scattering data [21, 50, 24, 186]. All this interest was triggered largely by the work of DeVries and collaborators [59, 163] who predicted, based on a few observations at very high energies, a rapid energy dependence of σ_R which was a reflection of the energy dependence in the individual nucleon–nucleon interactions. The measurements confirmed the predicted decrease of σ_R to less than the geometrical limit for E/A above some tens of MeV, reaching a minimum near 300 MeV, as Fig. 6.9 shows for $^{12}C + ^{12}C$.

DeVries' original calculations were based on the optical limit of the Glauber approximation, assuming straight-line trajectories for the colliding nuclei. The effect of the nuclear potential was studied [22] and it was found that the effects of a deep real potential (similar to those resulting from folding model calculations) could be observed in the behaviour of σ_R at $E/A \approx 10$ MeV. The two solid curves in Fig. 6.9 correspond to potentials with shallow and deep real parts; the best agreement with the experimental values is obtained with the deep potential assumption [186].

The value of σ_R can be calculated from the transmission coefficients T_l corresponding to the l-wave elastic scattering matrix elements S_l,

$$\sigma_R = \pi\bar{\lambda}^2 \sum_l (2l+1)T_l \,, \tag{6.3}$$

where

$$T_l = 1 - |S_l|^2 \,, \tag{6.4}$$

and where $\bar{\lambda}$ is the reduced wavelength. This expression is only weakly sensitive to the details of the real part of the optical potential. As (6.3) indicates, it is dominated by the behaviour of T_l with l. The $(2l+1)$ weighting means it is most sensitive to the peripheral partial waves, where T_l falls from ≈ 1 to 0. In turn, these are especially sensitive to the diffuseness of the imaginary potential, as has indeed been observed [21, 185]. As an indication of the variation in σ_R for different optical model potentials we find, for example, that for the $^{12}C + ^{12}C$ elastic scattering data at $E_{lab} = 126.7$ MeV, one obtains values ranging from 1330 to 1460 mb, a variation of 10%, depending on the potential

chosen. As observed in Fig. 6.9, the optical model analyses give results consistent with the direct measurements as well as the predictions from nucleon–nucleon cross sections [59, 163].

7. Potential ambiguities

7.1. Continuous ambiguity

The continuous, or Igo, ambiguity [91] for heavy-ion optical potentials refers to the possibility of describing a given set of elastic scattering data with any of an infinite number of potentials which have in common the same exponential tail in the large-r region. The origin of the ambiguity is, of course, the strong absorption that eliminates all sensitivity to the inner parts of the potential [182].

The cases that interest us in this work, are precisely those where the absorption is relatively weak in the interior region. Sensitivity tests have reported sensitivity to small radii well inside the point where a Woods–Saxon potential becomes exponential, and therefore no Igo-type ambiguity can be expected. Fig. 7.1 shows an example of real potentials that reproduce well, *albeit* with differing degrees of goodness, high energy $^{16}O + ^{12}C$ data [114]. The WS curve is the optimum Woods–Saxon potential, while $FOLD + \Delta V$ is the result of adding to a DDM3Y folding-model calculation the sum of two WS derivatives, one attractive (centred near $r \approx 4$ fm) and one repulsive (near 1 fm), so that the total potential has a nonmonotonic behaviour. The imaginary parts of these potentials were weak, about 20 MeV at the centre. The quality of the fits obtained with these two potentials were good, with χ^2 approximately unity. The agreement between these optimum potentials in the region $r \geq 3$ fm suggests, as was independently proven by a notch test, that the sensitivity extends inside the point ($r \approx 4$ fm) where the potentials become purely exponential; therefore, no continuous ambiguity is expected, and indeed none was found. This example is representative of the degree of sensitivity encountered in similar light heavy-ion systems at other intermediate energies.

As will be discussed below, certain sets of measurements can be described in terms of a strongly absorbing potential, as well as by ones which are weakly absorbing. The former potentials do present an Igo-type ambiguity, as was encountered in the original analysis of $^{16}O + ^{12}C$ at 608 MeV.

7.2. Discrete ambiguity in the real part

Discrete ambiguities in the determination of the nuclear potential have been known for light ions since the 1960s [62], and were soon found for the first experimental studies of light heavy-ion elastic scattering. The measurements, on the identical-particle systems $^{12}C + ^{12}C$ and $^{16}O + ^{16}O$, consisted of cross sections taken at a few selected angles and energies between the Coulomb barrier (about 10 MeV) and 60 MeV in the laboratory. The optical model analyses of these data, made using Woods–Saxon potentials [131, 173], showed a variety of ambiguities in the determination of the nuclear potential, in particular the existence of a large number of discrete families of real potentials which fitted equally well the angular distributions and the excitation functions. For simplicity, the one chosen to illustrate the main features of the scattering was the weakest family of potentials, which for $^{16}O + ^{16}O$ had a real part only 17 MeV deep. This choice required no energy-dependence in the potential strength. From then on, such shallow potentials were frequently used in analyses of

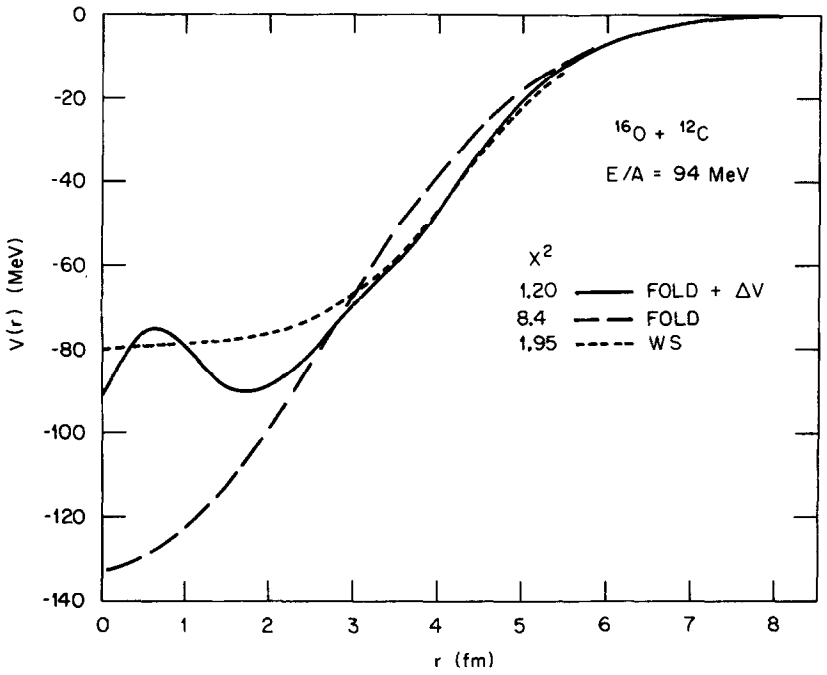

Fig. 7.1. Real parts of optical potentials that fit the scattering of $^{16}O + ^{12}C$ at $E/A = 94$ MeV. The dashed curve represents a folded potential based upon the original DDM3Y interaction and renormalized by the factor $N = 0.99$. The solid curve shows the unrenormalized folded potential plus an optimum spline correction term. The dotted curve indicates a Woods–Saxon potential (from [114]).

heavy-ion scattering measurements, until data at higher energies became available which showed the inadequacy of such a weak attraction at small radii.

The discrete ambiguities in the real potential encountered in the analysis of α-nucleus scattering were resolved by the observation of nuclear rainbows, whose structureless falloff determined uniquely the appropriate potential family [75]. Fig. 7.2 shows an example given by Goldberg to illustrate the power of the refractive effect. The data up to 60° could be described by a number of Woods–Saxon potentials with discretely different real parts. For example, the first one had $V \sim 115$ MeV, and the second had $V \sim 180$ MeV. For the 115 MeV potential, the nuclear rainbow was located at about 60°, and the first Airy minimum forward of the rainbow was located at about 30°. (This may not be obvious to the untrained eye; the nearside/farside decompositions discussed in Section 10.1 permit one to disentangle the Airy structures of the farside amplitude from the diffractive near/far interference.) The optical interpretation of the scattering by the 180 MeV potential is different, since its nuclear rainbow is near 140°, the first Airy minimum appears at 60° and the second Airy minimum is at 30°. Generally, in the presence of a discrete ambiguity, the observed refraction minima will correspond to different orders of Airy minima, as one changes from one potential to the next. In the case shown by Fig. 7.2 the observation of the exponential falloff of the nuclear rainbow well beyond 60° allowed the unique selection of the 115 MeV potential as the appropriate one. This entails the measurement of very small cross sections at energies sufficiently high for the refractive falloff to appear at angles smaller than 180°. (This becomes 90° for identical systems; for example,

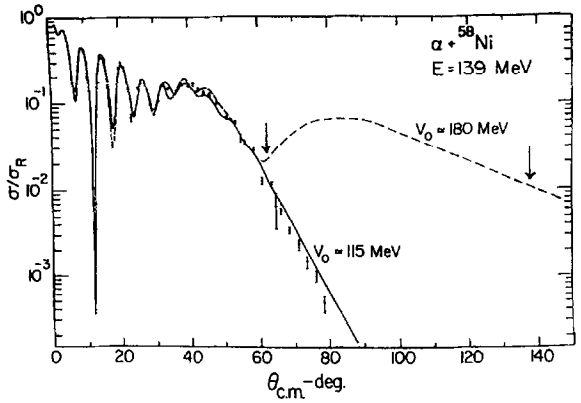

Fig. 7.2. Comparison of cross sections for elastic scattering of α-particles from ^{58}Ni. The arrows indicate the maximum deflection angles calculated using the $V_0 = 115$ MeV ($\approx 60°$) and the $V_0 = 180$ MeV ($\approx 140°$) real potentials that fit the forward angle data (from [76]).

we have estimated [30] that the nuclear rainbow in $^{12}C + {}^{12}C$ will reveal itself forward of 90° at $E_{lab} \geq 200$ MeV.)

For light heavy-ions at $E/A \leq 10$ MeV, a qualitatively similar discrete ambiguity has been observed. Fig. 6.2 illustrates how different "families" of real folded potentials, characterized by their discretely different renormalization factors N, describe equally well the $^{12}C + {}^{12}C$ data below $E/A = 10$ MeV. At higher energies, as the nuclear rainbow falloff moves into the experimentally accessible angular range, the choice becomes unique (indicated by the solid symbols in Fig. 6.2) and the ambiguity can be removed, if consistency between the results for the two energy regions is demanded.

The analysis of the $^{16}O + {}^{16}O$ data at 350 MeV [198, 199] presents an interesting example of the complications that can arise because of the discrete ambiguity. The measurements were performed in two different experiments, the second one extending the original angular range from 61° up to 73°. Fig. 7.3(a) shows the first set of data [198] and three possible descriptions of the original data, with increasingly deep WS^2 real potentials A, B, and C, which lead one to interpret the clearly visible 43° minimum as the first, second and third Airy minimum, respectively. Fig. 7.3(b) shows the manifestation of the discrete ambiguity in the χ^2 vs. V_0 relation; the minima in χ^2 correspond to the central depths of the three potentials shown in Fig. 7.3(a). The initial analysis of these data [198] seemed to indicate that the observed 43° minimum corresponded not to the primary Airy minimum, but to the secondary (as predicted by potential family B), and predicted that the differential cross section would rise up again to display the rainbow maximum at around 70°. Kondō et al., in an independent phenomenological optical model analysis of the original data [117], proposed that the 43° minimum most probably was the primary one. Their argument came from a comparison of the real potential strength (quantified by its volume integral) at 350 MeV and those independently determined from an interpretation of scattering data at much lower energies, near the top of the Coulomb barrier, in terms of "molecular" resonances [115, 116]. At these low energies, the potential must be sufficiently deep so as to sustain quasi-bound states with enough radial nodes to satisfy the Pauli principle (see chapter 12). This condition allowed three potentials whose volume integrals are indicated in Fig. 7.3(c), together with the integrals for the three potentials A, B and C determined from the 350 MeV scattering data. On very general grounds, we expect the strength of the potential

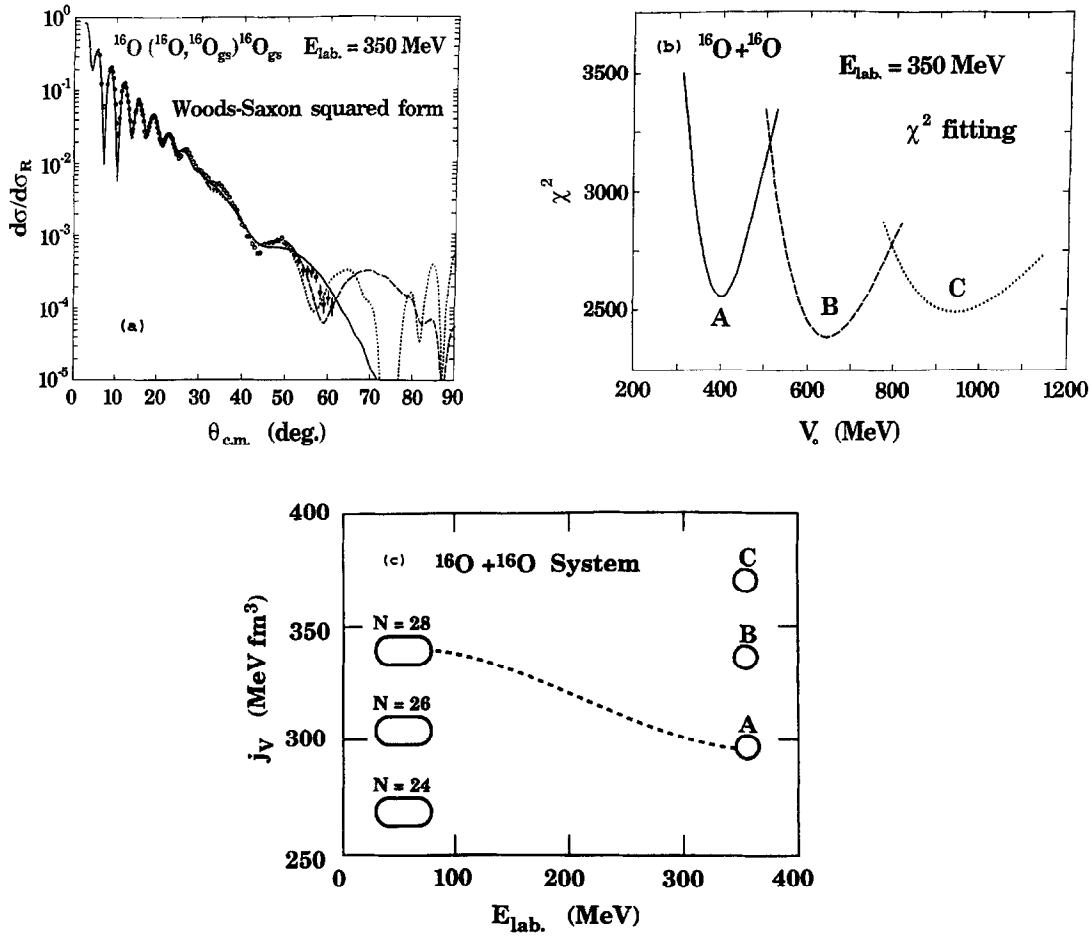

Fig. 7.3. Resolution of the discrete ambiguity in the real potential for $^{16}O + ^{16}O$ at 350 MeV. (a) The original elastic scattering data [198] and calculations with three different potentials: A (solid curve), B (dashed curve) and C (dotted curve). (b) The χ^2 value as a function of the real central depth V shows three minima, one for each of the potential families. (c) The volume integral per interacting ion pair, for two energies. The lower energy values of J_V come from the work of [115]. The potentials that are consistent with the dispersion relation are connected by the dotted curve (from [117]).

to increase as the energy decreases, allowing one to select the pair of potentials joined by the dotted line as the physically realistic ones.

As made evident by Fig. 7.3(a), only the unambiguous observation of the exponential falloff well after the rainbow angle can identify an Airy minimum as being indeed the first, and therefore remove the potential family uncertainty. The measurements were extended further out in angle [199] and no rise was observed beyond 61° (see Fig. 2.3), confirming Kondō's potential choice. However, if nontraditional forms are selected for the potential shapes, some doubts may still remain; details on this subject can be found in Section 9.

If the solution of the discrete ambiguity problem is far from trivial with data of the quality displayed by the $^{16}O + ^{16}O$ measurements at 350 MeV, the situation is even harder at lower energies

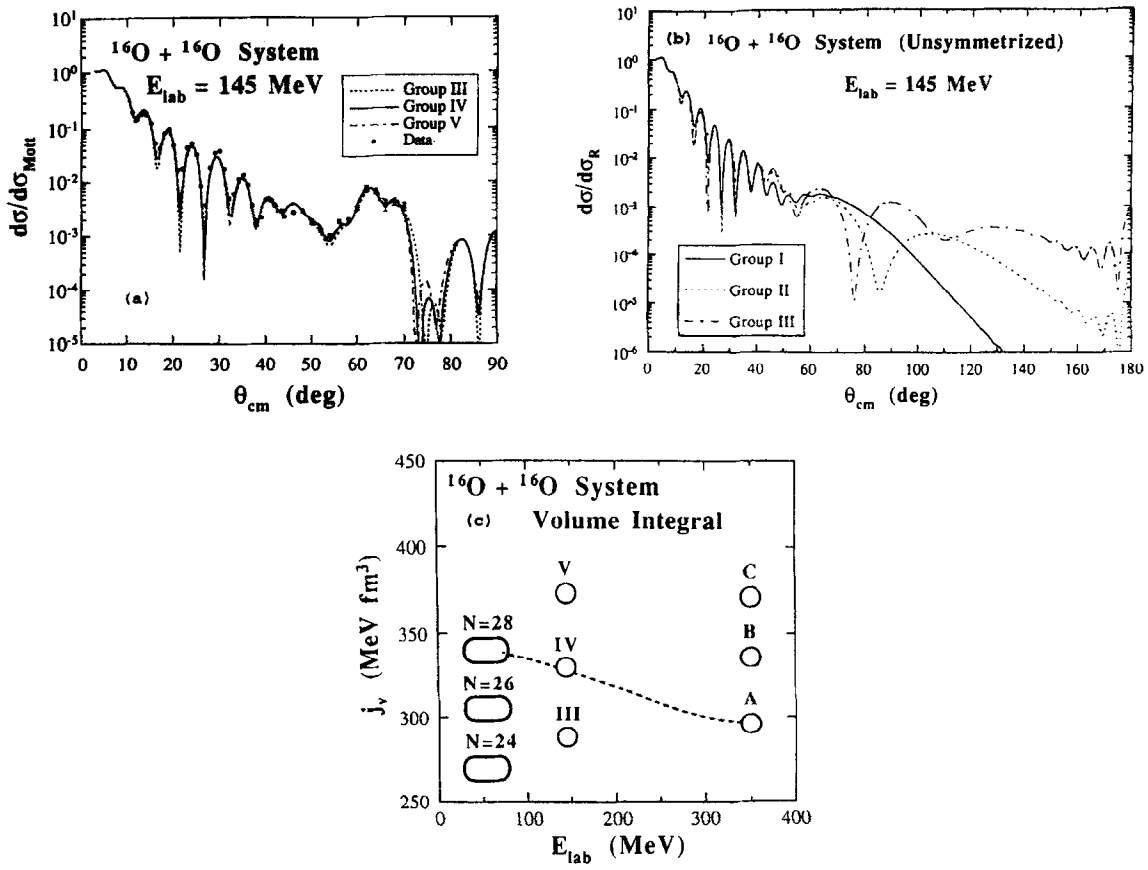

Fig. 7.4. Resolution of the discrete ambiguity in the real potential for $^{16}O + ^{16}O$ at 145 MeV. (a) The data [200] and calculations with three different potentials, called III, IV and V. (b) Unsymmetrized calculations with three potentials that fit the data, illustrating the discrete shift in the Airy minima and maxima as the potential strength increases. (c) Volume integral per interacting ion pair for real potentials III, IV and V, together with results at two other energies. The dashed curve indicates the choice of family IV, since it is the one that follows the energy dependence established in previous studies (from [200]).

where no exponential falloff can be seen in the measured angular range. Fig. 7.4(a) shows measurements for $^{16}O + ^{16}O$ at $E_{lab} = 145$ MeV [200], where a strong minimum can be observed at about 54°. What is shown in Fig. 7.4(b) is the unsymmetrized optical model calculation in order to avoid the (uninteresting in this situation) interference near 90° due to the identity of the nuclei. (This interference extends to more forward angles and becomes more evident as the energy decreases because of the reduction in the slope of the unsymmetrized angular distribution, until it dominates the angular distribution as the energy approaches the top of the Coulomb barrier. Thus it becomes a much more bothersome feature for the interpretation of the data at lower energies. Another example is presented in Section 10.1). The angular distribution for potential I in Fig. 7.4(b), which has $V_0 = 121$ MeV, shows the nuclear rainbow exponential falloff after the 54° minimum, showing that this is its first Airy minimum. This potential predicts no minima beyond this angle. Potential II, with $V_0 = 209$ MeV, places its first Airy minimum at 86°, and the one at 54° becomes the *second* Airy

minimum. For potential III, with $V_0 = 362$ MeV, 54° is the angle of the *third* Airy minimum, while 77° is the angle for the second, and the first is located at about 110°, and so on for the stronger potentials. Since the angular distribution is symmetric with respect to 90°, and within this angular range no exponential falloff is observed in the data (Fig. 7.4(a)), no nuclear rainbow identification may be possible. At higher energies, the angular structures move forward in angle allowing one to observe the rainbow and to choose the appropriate family, as has been done for this system at 350 MeV. Fig. 7.4(c) is an extension of Fig. 7.3(c), and shows that the 145 MeV family IV is consistent with the phenomenological studies at the other energies [120]. The same conclusion is reached after a folding model analysis [101] of the data.[4]

This explanation of the discrete ambiguity for light heavy-ions in terms of an angular shift of the Airy pattern was proposed in 1991 [34], based on an analysis of ^{6}Li+^{58}Ni scattering at $E/A = 35$ MeV, and other lighter systems. Fig. 7.5(a) shows the discrete ambiguity for potential calculations (farside only) that describe equally well data forward of 35°. Starting from the shallowest real potential that describes the 29° minimum ($V_0 = 174$ MeV), the fits deteriorate as the real strength increases because the calculated minimum moves backward, beyond 29°, until the value $V_0 = 266$ MeV is reached. This particular value of V_0 puts the second Airy minimum at 29°, therefore restoring the fit to the data. If one continues increasing the real potential strength, the minima do shift backward until the next Airy minimum falls into place ($V_0 = 360$ MeV) and one recovers an acceptable fit, etc. It is the *semiperiodic* structure of the Airy pattern that causes the discrete ambiguity. The measurements [155] that motivated this analysis reached up to 50° and did show an exponential decay beyond 35°, therefore selecting unambiguously the value of $V_0 = 174$ MeV as the correct one.

In the same work [34], the shift of the Airy pattern in going from one potential to the next was shown to be equivalent to a phase-shift increment by $n\pi$ for the low-partial waves, while no phase change occurs for the peripheral ones. Fig. 7.5(b) shows the phase shifts corresponding to the real potentials in part (a). The deflection function, calculated as in (3.10), indicates that the 29° minimum arises from the interference of the $l \approx 22$ and 40 partial-wave amplitudes. It can be observed in Fig. 7.5(b) that the difference between $\delta(22)$ and $\delta(40)$ changes by an integer number of π between the ambiguous potentials. The reader will probably be reminded of the much earlier proposal by Drisko et al. [62] of a similar explanation for the discrete ambiguities in light nuclear systems. A discussion of the effect of potential resonances in the discrete ambiguity for light ions can be found in [34]. We emphasize that the requirement of some transparency for low-l partial waves (i.e. weak absorption) is essential in order to observe the *discrete* ambiguity. Without it, we would regain the *continuous* ambiguity of Igo [91].

7.3. Shallow- or deep-W ambiguity

The 1988 global analysis of ^{12}C + ^{12}C and ^{16}O + ^{12}C data above 10 MeV per nucleon [27] showed the need for a weak absorptive potential to produce a consistent description of the data at several energies. The key factor in the proposed description was the unambiguous need for shallow imaginary parts, between 15 and 27 MeV at the centre, over the energy range from 10 to 94 MeV/nucleon. These conclusions applied to both phenomenological and microscopic real potentials. Fig. 7.6 shows

[4] This conclusion arises from the similar values of the volume integrals; due to an error in [101], probably typographical, the authors mention potential III as the one consistent with their DDM3Y1 folded potential.

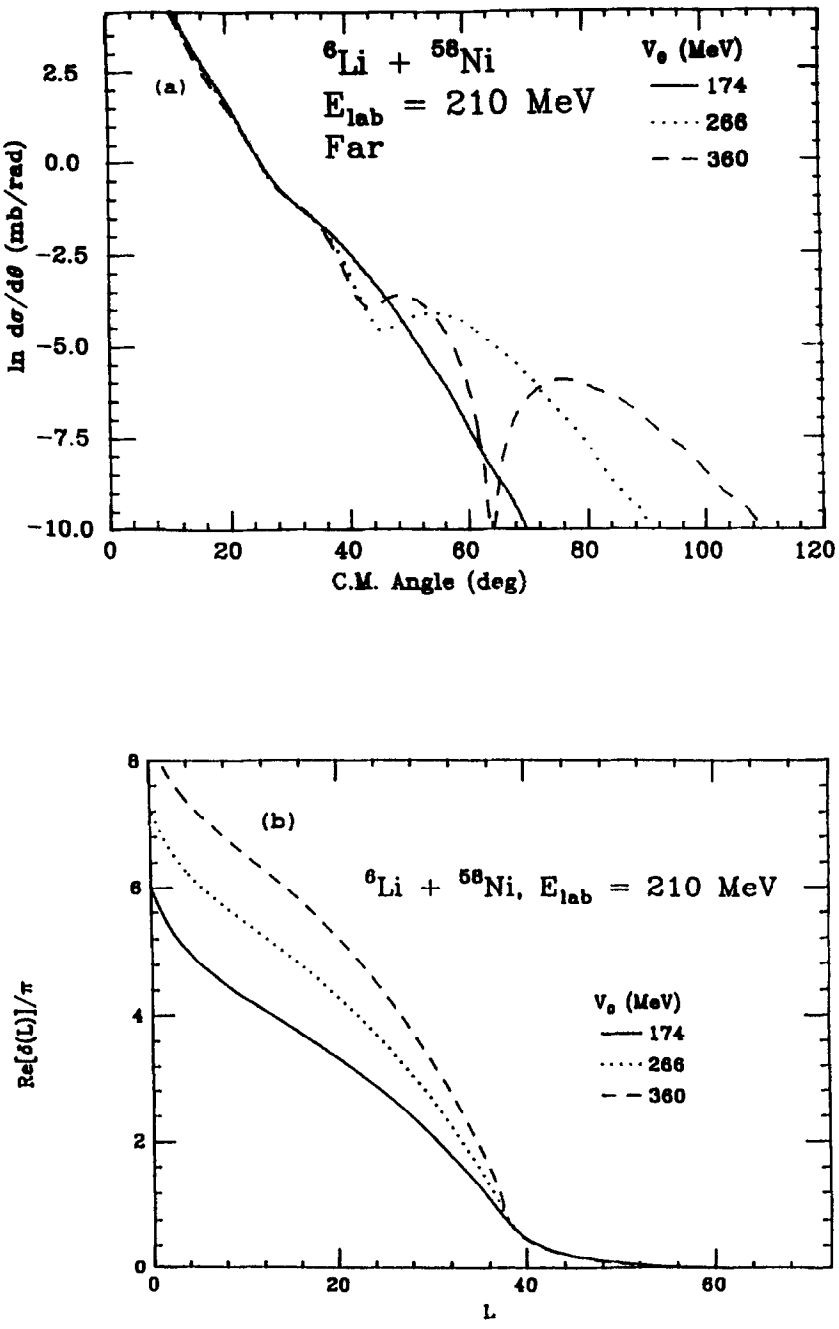

Fig. 7.5. Illustration of the discrete ambiguity in the real potential for ^{6}Li + ^{58}Ni. (a) Farsides calculated with three potentials that fit the data forward of 35°. (b) Phase-shifts for the three potentials, showing increments of $n\pi$ among them. This ambiguity is solved by the data, that extends up to 50°, in favour of the potential having $V_0 = 174$ MeV (from [34]).

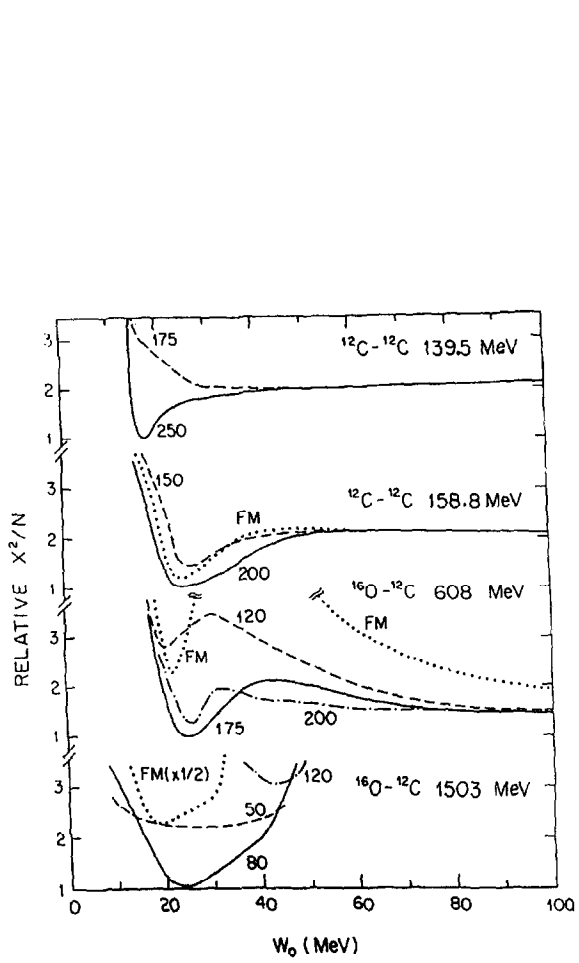

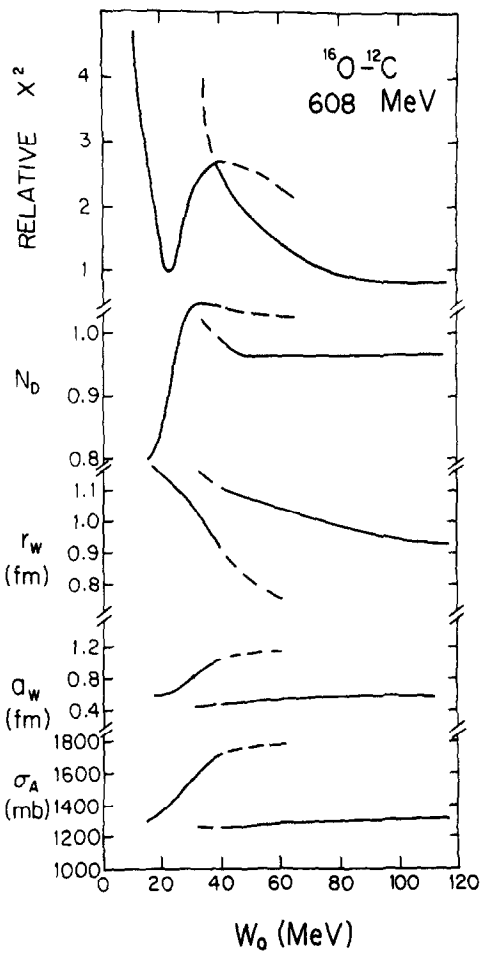

Fig. 7.6. Values of the (relative) χ^2 as a function of the imaginary potential central depth for four sets of elastic scattering data. Dotted curves "FM" correspond to folding model analyses using the original DDM3Y potentials. The other curves are results with phenomenological real parts whose central depths (in MeV) are indicated. All the imaginary parts are treated phenomenologically, with WS shapes (from [27]).

Fig. 7.7. Shallow- or deep-W ambiguity in the scattering of $^{16}O + ^{12}C$ at 608 MeV. The evolution of the three fitted parameters (the renormalization N_D for a DDM3Y folding model real part, the WS reduced imaginary radius r_W and the diffuseness a_W) is shown as a function of the imaginary central depth W_0. The shallow- and the deep-W minima in χ^2 correspond to potentials having different characteristics (from [28]).

the values of the χ^2 function as a function of the central imaginary depth for selected sets of data. As can be seen, only values of W_0 between 15 and 27 MeV allow a description of all the measurements with an optical model potential (in this case, of WS shape) which varies smoothly with energy.

At the same time, this analysis indicated that some of the data sets (such as $^{16}O + ^{12}C$ at 608 MeV in Fig. 7.6) could be described well by potentials with either a shallow or a deep imaginary part. It is the continuity requirement between different energies that led the authors in [27] and [28] to

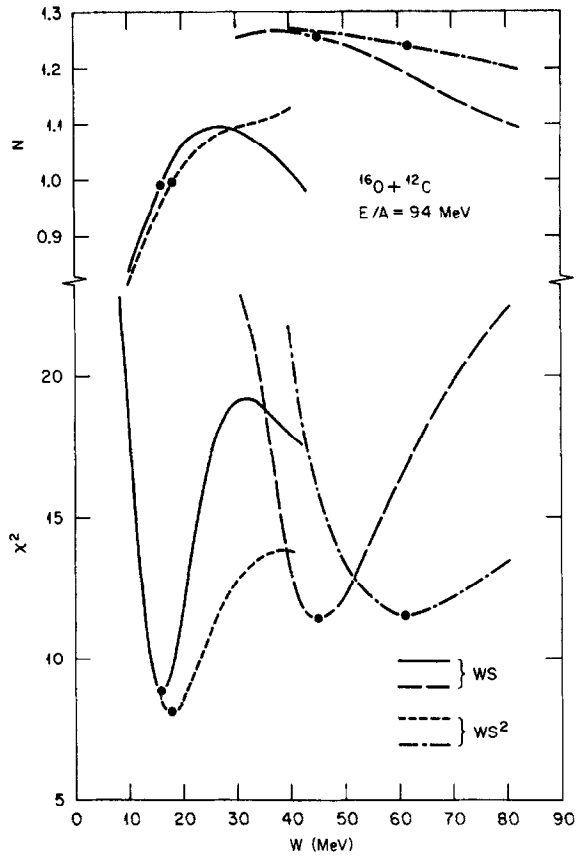

Fig. 7.8. Shallow- or deep-W ambiguity in the scattering of $^{16}O + ^{12}C$ at 1503 MeV. The values of χ^2 and the renormalization N for a DDM3Y folding model real part are shown as a function of the imaginary central depth W. The imaginary part was treated phenomenologically, assuming either WS or WS^2 shapes (from [114]).

choose the weakly absorptive solution as the "correct" one; later studies showed that in some cases the best fit (in terms of giving the minimum χ^2) might actually correspond to the potential with the stronger absorption, indicating that the χ^2 criterion should be treated with caution.

Three of the data sets showing this weak- vs. deep-W ambiguity were studied in detail as part of an analysis using potentials with folding model real parts [28, 114]. Fig. 7.7 shows the evolution of the potential parameters as a function of the imaginary real depth W_0 for the case of $^{16}O + ^{12}C$ at 608 MeV. It can be observed that the parameters do not transform smoothly in going from the weak-W ($W \approx 25$ MeV) to the deep-W ($W \geq 80$ MeV) solutions, but instead they correspond to two discretely different types of potentials. For the case shown in Fig. 7.7, the weak-W potential is relatively well determined, while the deep-W presents a continuous ambiguity (it is possible to obtain fits with similar quality for an infinite number of combinations of imaginary parameters if W_0 is about 80 MeV or larger). This is not exactly the case for $^{16}O + ^{12}C$ at 1503 MeV, as displayed in Fig. 7.8, where besides the weak-W potential that prefers $W \approx 16$ MeV, the deep-W potential shows a preference for a given depth, $W \approx 50 - 60$ MeV, depending on the choice of WS or WS^2 for the

imaginary form factor. Another apparently "unambiguous" deep-W alternative is found in the analysis of another high-energy case, that of $^{12}C+^{12}C$ at 1016 MeV, with minima at $W \approx 30$–40 MeV. An interpretation of this ambiguous description in terms of semiclassical trajectories is presented in Section 10.2.

Besides the cases already mentioned, other W ambiguities have been observed for other heavy-ion systems. For example, $^{16}O+^{28}Si$ at $E/A = 94$ MeV displays two minima in χ^2, qualitatively similar to those in Fig. 7.8, at $W \approx 40$ and 70 MeV. Here no weak-W description has been found [114].

8. General features of the potentials and the WIV systematics

The heavy-ion nuclear potentials discussed are capable of describing a large amount of elastic scattering data over a wide energy interval. So far we have looked directly at the data trying to identify in the measurements those features which could indicate an interpretation in terms of refractive effects. But, which are features in the potentials themselves that signal their "refractive" character? The most obvious of these characteristics are the strengths of the real and the imaginary parts. Real parts must be deep in order to "pull" the farside trajectories sufficiently to negative angles and to locate the maxima and minima of their Airy interference pattern at the angles where the data show them. Since the sub-trajectories of the farside amplitude that produce this interference penetrate into the interior of the potential, the imaginary potential must be shallow for them to survive.

The first and second rows in Fig. 8.1 show the real and imaginary parts of phenomenological potentials that describe $^{12}C+^{12}C$ and $^{16}O+^{16}O$ data at two different energies. Two alternative potentials have been chosen for each case. The selected potentials display the main features found in all data analyses: they depend on the energy, their real parts are deep ($V \sim 100$–350 MeV) and their imaginary parts are relatively shallow ($W \sim 7$–30 MeV). By using a logarithmic scale, the second row in Fig. 8.1 emphasizes the next important feature of these potentials: the shapes of the real and imaginary parts are always different, particularly at the far surface, where the absorption decreases faster than the nuclear matter distribution. The third row in Fig. 8.1 presents the above features summarized in a single function [38]: the ratio of the imaginary and real parts, $W(r)/V(r)$, as a function of radius. The function

$$w(r) \equiv W(r)/V(r)\,, \tag{8.1}$$

has been called [38] a "reduced imaginary potential" since it can be interpreted as the flux removal from the elastic channel $W(r)$ weighted by the inverse of the matter distribution, approximately represented by $V(r)$. This function is remarkably similar for all the potentials, as can be observed in Fig. 8.2, where $^{12}C+^{12}C$ potentials and their ratio are shown for E/A between 7 and 82 MeV. Three characteristics can be seen:

(a) For small r, $W(r)/V(r) \ll 1$, indicating deep elastic interpenetration of target and projectile, a feature required by the appearance of refractive effects in the angular distributions;

(b) For large r, $W(r)/V(r) \ll 1$, implying low reaction rates at the far-surface;

(c) At the surface, $W(r) \approx V(r)$.

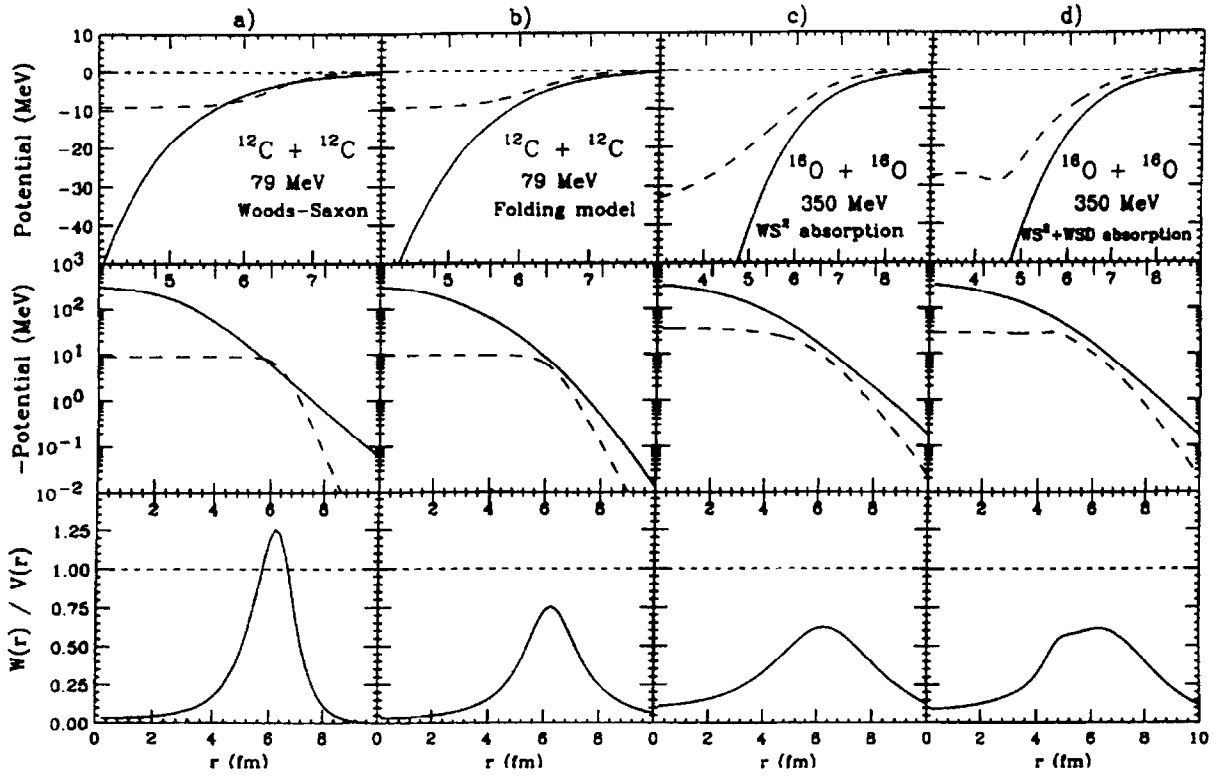

Fig. 8.1. Typical potentials that describe light HI elastic scattering. The solid curves in the top two rows are the real parts and the dashed curves correspond to the imaginary parts. In spite of the different parameterizations, they all show a systematic behaviour for the ratio $W(r)/V(r)$ (from [38]).

For phenomenological potentials with Woods–Saxon shape these features of $W(r)/V(r)$ can be traced back to relations between some of the potential parameters: $W < V$, $R_w > R_v$, and $a_w < a_v$. These are fulfilled by all but one of the potentials listed in Tables 2 and 3 (the exception, at a high bombarding energy, is discussed later). The systematics for different systems at different energies indicates that the maximum of the reduced potential $w(r)$ is located at radii about 1.2–1.4 fm times $(A_p^{1/3} + A_t^{1/3})$ and that this radius decreases as the energy increases. Attempts to relate $w(r)$ to other variables of the scattering have found [38] that the peak in $w(r)$ coincides in location with the apsidal distance for the trajectory with the angular momentum l for which the function $d|S|/dl$ has its maximum. According to Austern and Blair [7] and Frahn [71], this indicates the peripheral region where collective direct reactions originate. Within this formalism, the peak also marks the so-called strong-absorption radius for the system and happens to be slightly larger than the imaginary radius R_w for the light heavy-ion data thus analysed [38].

These $w(r)$ systematics are fulfilled by phenomenological potentials describing α-particle scattering on nuclei from ^{12}C to ^{208}Pb (with the exception of ^{116}Sn), $^{6,7}Li$ scattering by a variety of targets, $^{12,13}C + ^{12}C$, $^{16}O + ^{16}O$, and $^{16}O + ^{12}C$, all for energies E/A greater than about 6 MeV. Fig. 8.3 shows $w(r)$ for potentials that fit some of these data and which fulfill the systematics. The ratio has been plotted against a scaled radius $r_0 = r/(A_p^{1/3} + A_t^{1/3})$ to unify the representation for different systems.

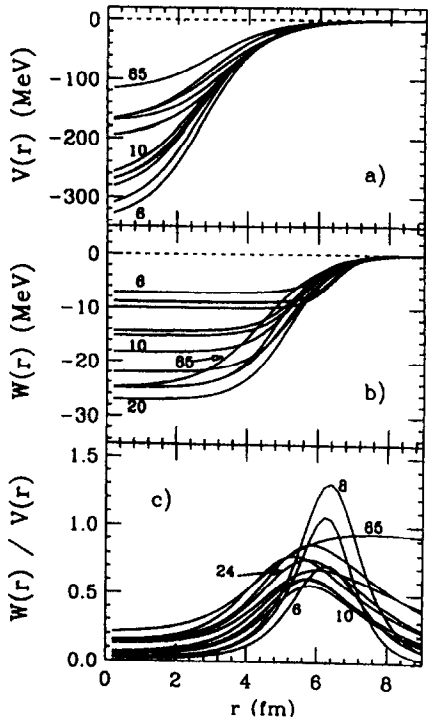

Fig. 8.2. Phenomenological potentials (WS shapes) for $^{12}C + ^{12}C$: real parts are shown in (a), imaginary parts in (b), and the ratios $W(r)/V(r)$ in (c). Numbers indicate E/A, in MeV (from [38]).

The folding model analyses which have been performed on some of these heavy-ion data using the DDM3Y effective interaction, produce potentials which also obey the $w(r)$ systematics at energies $E/A \lesssim 15$ MeV, as the example in Fig. 8.1 shows. Above this energy, the calculated potentials frequently present a far-surface tail that is steeper than that which apparently is required by the data [190], and the ratio W/V does not drop to values less than unity in the external region. Almost all these folded potentials have been constructed using the zero-range pseudo-potential (5.7) for the exchange term, and it might be surmised that this is responsible for the discrepancy just mentioned. It would be interesting to examine this using the more sophisticated approach of Khoa et al. [98, 101] which does not make the zero-range approximation.

Phenomenological potentials which are known not to agree with the $w(r)$ systematics are those for $^{20}Ne + ^{12}C$, $^{14}N + ^{12}C$, $^{9}Be + ^{12}C$ and $^{9}Be + ^{16}O$. All of them are absorptive in their far surface, having $a_v < a_w$, and a $w(r)$ curve which increases continuously, without a maximum. It is not yet clear what there is in the structure of these nuclei that sets them apart from the behaviour observed for the other nuclei, which are mostly "$4n$" or "α-particle" nuclei, but their strong deviation from the $w(r)$ systematics indicates that the detailed structure of target and projectile can influence the absorptive part of their optical potentials.

The dashed curves in Fig. 8.3 correspond to the high energy data $^{12}C + ^{12}C$ at $E/A = 85$ MeV and $^{16}O + ^{12}C$ at 94 MeV. For these two systems, the absorption in the far-surface has increased, relative to that for the lower energy potentials, so that $W(r)/V(r) \gtrsim 1$ and the $w(r)$

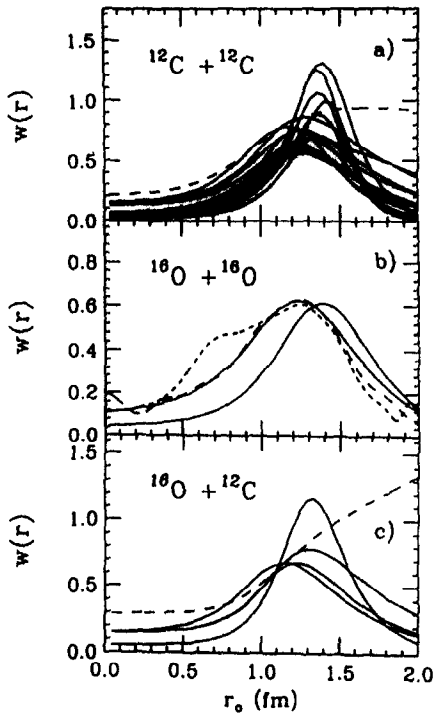

Fig. 8.3. The ratios $w(r)=W(r)/V(r)$ as a function of reduced radius for systems that follow the systematics. In (a), the different curves correspond to WS potentials at different energies. In (b), which corresponds to potentials that fit the 145 and 350 MeV data, the solid curves correspond to phenomenological (WS^2) potentials and the dashed curves are potentials obtained by inversion. In (c), the different curves correspond to WS potentials at different energies (from [38]).

systematics are not fulfilled. An explanation for this apparent evolution of the potentials with energy has been given in [37] based on the application of the double-Glauber approximation to light heavy-ion scattering.

The optical limit of the double-Glauber approximation obtains the scattering phase shifts from a "potential" which is essentially a double-folding potential used for both $V(r)$ and $W(r)$, with complete neglect of suppression due to the Pauli principle. This potential gives the same radial shape for the real and the imaginary part, and at $E/A \approx 100$ MeV, W/V is approximately equal to unity. As the systematics of the phenomenological potentials show, the Glauber approximation grossly overestimates the absorption, except in the few cases at high energies where $w(r) \approx 1$ in the far-surface region. The nucleon density is low in this region, Pauli suppression should be minimal and it is plausible that the increased absorption implied by $w(r) \approx 1$ may be due to an increased probability of nucleon knockout in the far-surface, the only type of absorbing process considered in the Glauber description. At lower energies, where the Glauber assumptions for the absorption strongly disagree with the $w(r)$ systematics, the description of the elastic scattering differential cross section by Glauber theory is bound to be in error. This failure is discussed in detail in [37].

9. How well can one set of data determine the potential?

9.1. Non-standard forms of potential

Once the weak absorption in the scattering of light heavy-ions has been established, allowing for the determination of the potential features in sub-surface regions, the question whether the detailed shape of the optical potential may differ from the standard phenomenological or the folding model form factor becomes tractable, at least in principle.

The $^{16}O + ^{12}C$ data at $E/A = 94$ MeV have been analyzed using optical potentials with more general shapes for the real part [114]. In particular, the DDM3Y folding model potential was taken as a reference, and modifications $\Delta V(r)$ either from a functional form or directly as specified values at fixed radial knots with cubic spline interpolation between them, were added. The potentials that resulted could even present nonmonotonic shapes, as can be observed in Fig. 7.1. The conclusions of the study signaled the possible need for modifications to the folding model potential in order to achieve an optimum fit, particularly an increased attraction at the surface and a reduced attraction at the centre, as curve "FOLD + ΔV" in Fig. 7.1, which is a functional form modification of the DDM3Y potential [114], indicates. The spline analysis produced potentials with a more structured oscillatory pattern than the functional ΔV but no physical significance was attached to the feature. Fits that appeared almost as good as those obtained using the modified folded potentials (although with χ^2 about twice as large) could be obtained with the conventional six-parameter WS or WS^2 forms!

The complete $^{16}O + ^{16}O$ data at 350 MeV [198, 199] have also been studied with optical potentials more general than the standard form factors. The authors of [33] performed optical model analyses of the data exploring the optimum exponents v_R and v_I to which the Woods–Saxon real and imaginary form factors, respectively, had to be raised, as well as the effect of modifying the real and the imaginary parts by a general determination of the potential at certain radial knots, supplemented by spline interpolation in between and exponential extrapolation at large radii. The first result was to detect a slight preference for $v_R = v_I = 2$. When a general spline imaginary potential form was optimized while keeping a WS or WS^2 real form factor, the resulting potential was similar to that obtained from the addition of an imaginary Woods–Saxon derivative WSD term (centred at about 4.6 fm) to the WS (or WS^2) imaginary volume term. Since the analytic option is much simpler to use, it was concluded that the optimum imaginary shape was a sum of WS (or WS^2) and WSD. Concerning a general form for the real potential, exploratory fits indicated that the study could be done assuming $v_I = 1$ and no WSD term, without loss of generality. In Section 7.2 we have discussed the three families of discretely different potentials (types A, B and C; see Fig. 7.3(a)) found by Kondō in his phenomenological analysis of the system. We have found [33] that the optimum spline real potentials were similar to Kondō's type A and type B, as shown by Fig. 9.1. (Spline potential X is too weak to sustain a rainbow, as discussed in [35] and Section 10.2). A DDM3Y folding model real potential for this system (with the optimum renormalization equal to 1.05), is also shown in Fig. 9.1. It proved to be very similar to the real part of the type A spline potential. The quality of the fits is improved by the extra parameters associated with the spline analysis, suggesting in this case, as in the other already discussed in this section, that the folded potential using the DDM3Y (or the similar, more recent, DDM3Y1 or BDM3Y1) interaction is a good first approximation to the real part of the potential.

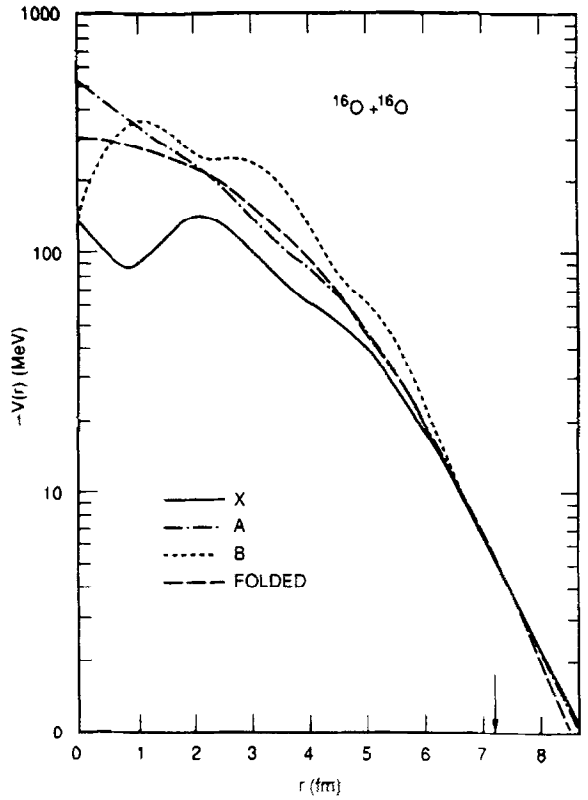

Fig. 9.1. Spline real potentials that fit the scattering of $^{16}O+^{16}O$ at 350 MeV (see Fig. 2.3.). Also shown is a folded potential, based upon the original DDM3Y interaction and renormalized by a factor of $N=1.05$ (from [33]).

More recently, these $^{16}O+^{16}O$ data at 350 MeV, together with others taken at 250, 480 and 704 MeV, were subjected to analysis [12] in which both real and imaginary parts of the optical potentials were represented by a series of Fourier–Bessel (FB) or Laguerre–Gaussian (LG) terms superimposed upon a starting potential with the form of the square of a Woods–Saxon. The LG expansion gave the best description of the data. The resulting fits to the data are shown in Fig. 9.2 and the corresponding potentials, together with their (correlated) uncertainties, are displayed in Fig. 9.3. (The dashed curves in both cases correspond to the results obtained using phenomenological Woods–Saxon potentials whose parameter values are tabulated in [12].) The model-unrestricted real potentials also have characteristics similar to those of the folded ones obtained earlier which used the BDM3Y1 or DDM3Y1 interactions [103].

Another study of the uniqueness of the potentials and phase shifts derived for a single set of elastic scattering data was performed on the $^{16}O+^{12}C$ data at 608 MeV [190]. The need for different noninteger exponents ν_R and ν_I was explored, as well as the addition of a WSD term to the standard volume imaginary term, and the determination of the real part at fixed knots plus spline interpolation. Many different potentials were found, all describing the data with $\chi^2 \approx 1$. The real parts of these potentials are all smooth functions of r, even if some of the spline potentials are nonmonotonic. The central depths of the real potentials are about 100 to 150 MeV, and they all tend to converge toward

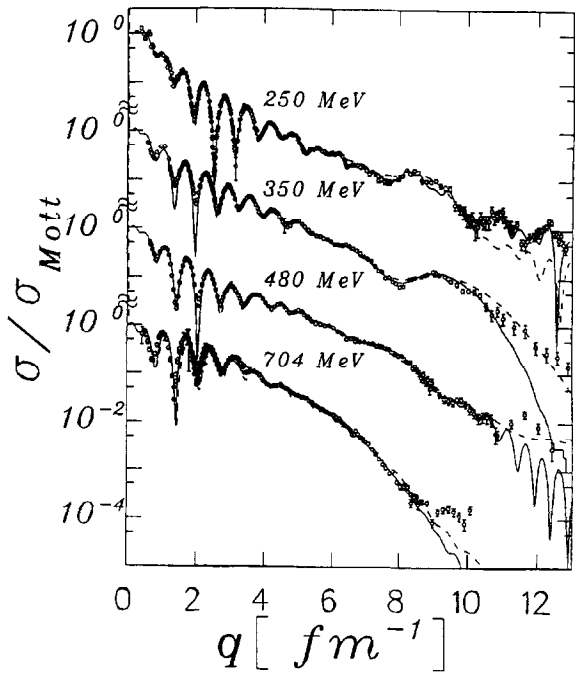

Fig. 9.2. Elastic scattering cross sections, in ratio to the Mott cross section, for $^{16}O + ^{16}O$ at several energies, plotted *vs.* momentum transfer q. The solid curves are fits obtained using model-unrestricted potentials expressed as series of Laguerre–Gaussian functions. The dashed curves represent fits obtained using the squares of Woods–Saxon potentials (from [12]).

$V(r) = -25$ MeV at $r \approx 5$ fm and to be similar at larger radii. Most of the imaginary parts peak near $r = 3$ fm, as shown in Fig. 9.4(a), confirming the need for an additional WSD absorptive term for an accurate phenomenological description of this system. Constraining the spline potential to have the values given by a DDM3Y folding model potential at $r \leq 3$ fm, shown in Fig. 9.4(b), suggests the need for a more diffuse real tail than that given by the DDM3Y prescription. This study also encountered the discrete ambiguity associated with the explanation of the large angle exponential falloff. Fig. 9.5 shows calculations for two potentials, one having a much deeper real part (about 280 MeV at the centre) which predicts the primary Airy minimum to be at 43°, and one that is 173 MeV deep at the centre that indicates that it is the primary rainbow that has been observed so that there are no additional minima to be seen. As in the $^{16}O + ^{16}O$ cases discussed above, a choice between the two could be made based on the systematics known at other energies, and/or similar systems. Of course, a definitive solution would require unambiguous data in the 40°–50° angular region.

We have presented in detail examples of thorough studies at single energies where, in spite of the reduced absorption, no conclusive answer about the fine details of the nuclear potential can be drawn. Furthermore, the chosen cases seem to suggest that the detailed potential structure appropriate for one system is not necessarily the one best suited for the other. This, of course, may be an indication of the limitations of the simple description of the scattering by a local optical model potential. The moral of these exercises seems to be that the optimum knowledge of the optical potential for

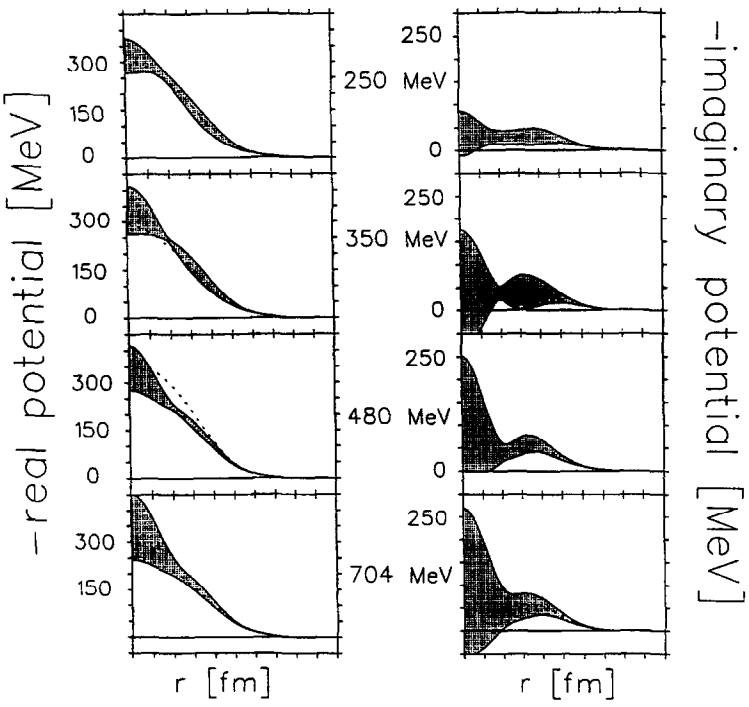

Fig. 9.3. The real and imaginary potentials obtained from the fits shown in Fig. 9.2. The hatched areas show the model-unrestricted LG potentials together with their (correlated) uncertainties. The dotted curves show the Woods–Saxon-squared potentials (from [12]).

a system cannot arise from the analysis of a single set of data. Ideally the scattering at several energies should be measured and studied and, if possible, data for other similar systems should be reasonably well described by a potential containing the same physical characteristics.

In this way we avoid the risk that some idiosyncracy of a particular measurement, rather than a true physical effect, is biassing our conclusions.

9.2. *Potentials obtained by inversion of the scattering cross sections*

With present day techniques and sufficiently precise data, it is possible to do a (complex) phase-shift analysis of a set of differential cross sections and then invert the phase-shifts to obtain an equivalent local potential that will reproduce them. The phase-shift analysis may be done using a parameterized $S(l)$ function, for example of McIntyre form [142], or more flexibly by adding a corrective function to a smooth starting function. The starting function can be optimized by a preliminary fit to the data; it may be of the McIntyre form, or derived from Glauber or other theory, or generated from an optimized model potential, folded or Woods–Saxon, etc. The corrective function then indicates what changes from the starting function are necessary to optimize the fit to the data. This procedure is illustrated by applications to the scattering of $^{16}O+^{12}C$ at 608 MeV [54], $^{12}C+^{12}C$ at energies from 139.5 to 2400 MeV [145] and to $^{16}O+^{16}O$ at 350 MeV [4, 56].

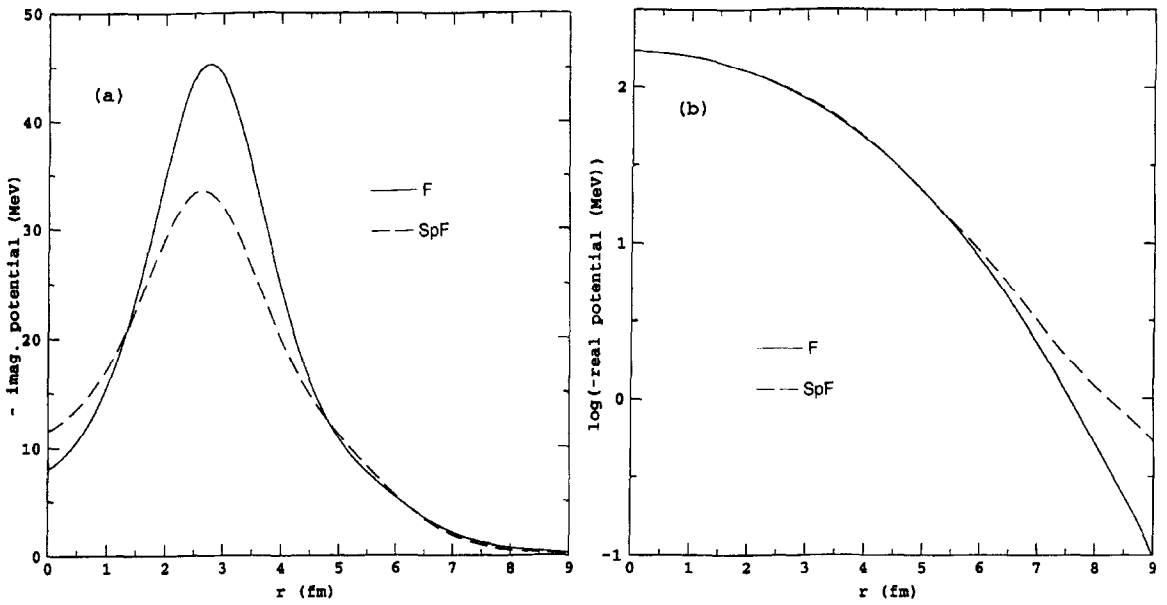

Fig. 9.4. Two examples of optical potentials that give equivalent fits to the scattering of $^{16}O + ^{12}C$ at $E/A = 38$ MeV. (a) Showing that the imaginary parts tend to peak near $r = 3$ fm. (b) The solid curve shows a folded real part constructed from the original DDM3Y interaction, renormalized by a factor $N = 0.845$, while the dashed curve represents a spline potential constrained to have the same value as the folded one for $r \leq 3$ fm. The spline version has a longer tail than the folded one (from [190]).

The determination of the phase-shifts presents a profound ambiguity problem. Although there is no ultimate solution to this problem, there are ways that it can be mitigated [145]. These include imposing some conditions, perhaps not well defined, such as "physical reasonableness", "smoothness" and "continuity with energy".

The S-matrix $S(l)$ that is so obtained, and which now represents the data, may be inverted to give a corresponding local potential. The inversion may be done analytically, in an iterative way, if the S-matrix is represented as a rational function [126]. A very flexible iterative-perturbative (IP) technique has been developed by Cooper and Mackintosh [145] which involves iterating a perturbative correction to a starting potential by determining amplitudes within an inversion basis. The basis may be spline functions, gaussians or Bessel functions, etc. The uniqueness of the resulting inversion potential may be tested by studying its independence of the starting potential and the basis chosen. A careful and detailed discussion of the application of this approach, and some uncertainties associated with it, is given in [145]. One possible interpretation of this procedure follows from adopting some model (such as folding) for the starting potential, then regarding the correction found as a local and l-independent representation of the dynamic polarization potential [141].

These powerful approaches enable one to obtain fits of very high quality to precise and complete sets of data (namely, χ^2 per degree of freedom of order unity, assuming that the experimental "errors" have been estimated realistically). In this sense the inversion potentials may be said to incorporate essentially all the information that is contained in the data. One price paid for this is

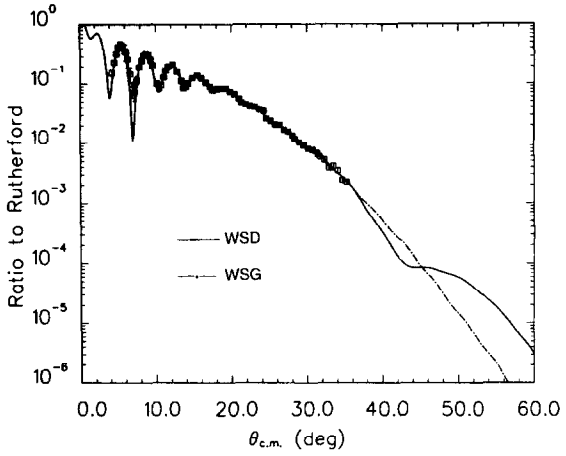

Fig. 9.5. The scattering of $^{16}O+^{12}C$ at $E/A=38$ MeV predicted by two Woods–Saxon potentials which give almost indistinguishable fits to the data in the measured angular range, but which differ markedly at larger angles. The WSD real potential (solid curve) is much deeper in the centre (about 280 MeV) than that for the WSG potential (about 173 MeV). This results in a dip near 43° which is interpreted as the first Airy minimum forward of the primary rainbow, which is predicted to be beyond 50° for this potential. On the other hand, the primary rainbow for the more shallow WSG potential occurs at a more forward angle, about 30°, so we only see the structureless dark side of the rainbow at these larger angles (from [190]).

that the potentials may be nonmonotonic, exhibiting oscillations, although an oscillatory behaviour is not neccessarily unphysical. It may simply reflect an underlying nonlocality, such as an l- or parity-dependence which is averaged over when using typical folding or phenomenological (namely Woods–Saxon) potentials.

It was found in the cases of $^{12}C+^{12}C$ [145] and $^{16}O+^{12}C$ [54] that the real inverted potentials were similar to the (DDM3Y) folded potentials for radii greater than about 5 fm, but were less deep between about 3 and 5 fm. The scattering (as determined by notch tests) was not sensitive to the potential at radii smaller than about 3 or 4 fm (although it must be remembered that the notch test itself gives results that depend upon the particular potential being used). The case of $^{16}O+^{16}O$ at 350 MeV has been examined by two groups [4, 56]. The work of [56] resulted in an inversion potential (see Fig. 9.6) whose real and imaginary parts behave very smoothly with radius, and whose real part seems to be in good agreement with the "realistic" (BDM3Y1 or DDM3Y1) folded one [101]. On the other hand, the potential found by [4] was based upon an S-matrix of the McIntyre form supplemented by six Regge-pole contributions, all but one of which were centred at l-values less than 40. This potential exhibited considerable structure, far from the range of theoretical expectations, although the quality of fit to the experimental data appeared to be comparable to that found by [56]. However, a two-step inversion procedure had previously been shown [55] to exhibit serious ambiguities even for exact fits to very precise data. The results of these two groups appear to present another example of this, and emphasize again the importance of using "prior information" to judge the physical significance of fits to experimental measurements. The "information" in this case includes some theoretical expectations as well as the use of systematics of fits to the scattering of similar systems or the same system at different energies; this leads us to choose the [56] result as the physically significant one.

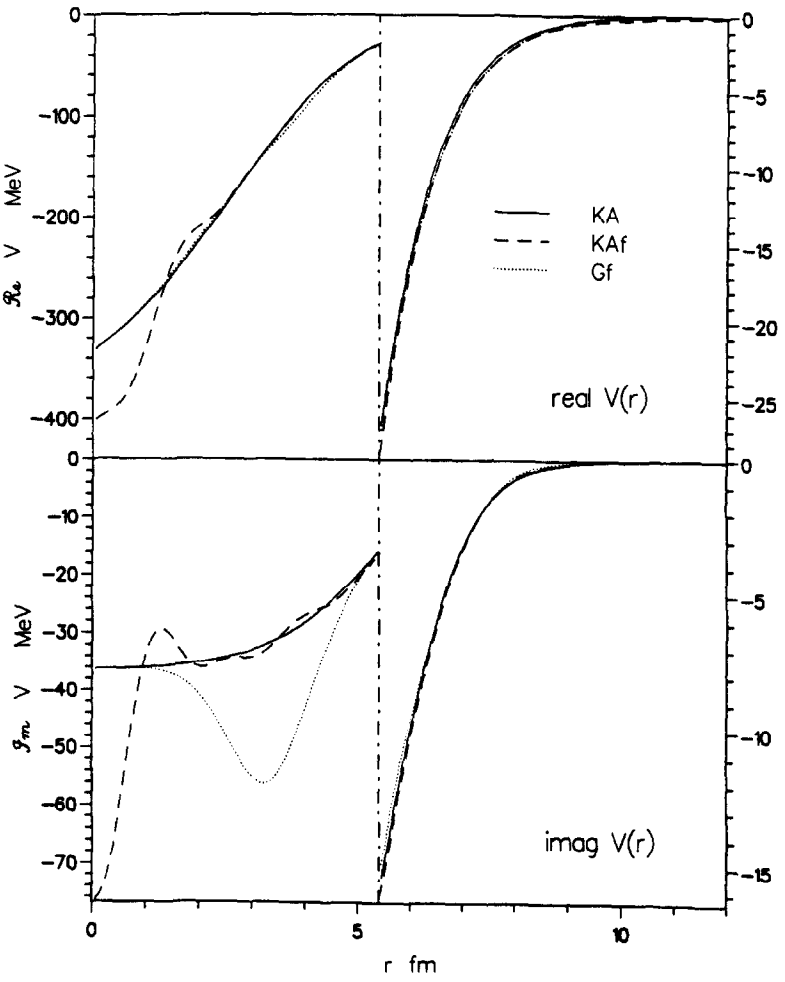

Fig. 9.6. Potentials for $^{16}O + ^{16}O$ scattering at 350 MeV. The solid line ("KA") represents the type-A Woods–Saxon potential from [117], while the broken curves were obtained from inversion of the phase shifts which fit the measured cross sections. The dashed curve ("KAf") started the inversion from the phase shifts generated by the Woods–Saxon potential, while the dotted curve ("Gf") started from the set of phase shifts given by the simplified Glauber model. Note that the values for $r > 5.3$ have been multiplied by a factor of ten (from [56]).

10. Interpretation of the elastic scattering in terms of trajectories

The separation of the scattering amplitude into nearside and farside scattering as well as other decomposition techniques presented in Sections 3.2 and 3.3 have played a significant role in the present understanding of the observed scattering of light heavy-ions. Probably their most practical use has been the identification of Airy structures in the scattering, features which do confirm the refractive character of the interaction. But, also of great importance, they have proven invaluable when trying to understand in optical terms the particular ways in which different potentials give rise

to a given angular distribution. In this section we present examples that illustrate the power of some of these techniques.

10.1. Nearside/farside decomposition applied to the data

The nearside/farside decomposition of the scattering amplitude is based on expressions (3.5) and (3.6) obtained by Fuller [74] and nowadays incorporated in a handful of computer codes. A revision of the formalism can be found in [88] together with many applications envisioned in days when some of the most revealing heavy-ion elastic scattering measurements were yet to be made.

As Fig. 3.2 indicates, the nearside trajectories are sensitive to both the Coulomb potential and the nuclear potential tail. The farside trajectories are mostly affected by the nuclear potential in subsurface and surface regions. The farside trajectories $l_<$ and $l_>$ interfere, producing widely separated Airy maxima and minima in the angular distributions. The interference of the nearside and the farside trajectories gives rise to the rapidly oscillating Fraunhofer pattern at forward angles. Fig. 3.7 displays the decomposition of the $^{12}C + ^{12}C$ scattering at 159 MeV into the nearside and farside components of the scattering amplitude. The symmetrization interference around 90° has been eliminated from the calculation for the sake of simplicity. (The description of the actual data with this potential can be appreciated in Fig. 6.1.) As it is depicted in Fig. 3.7, the forward oscillations are caused by the interference of nearside and farside amplitudes while the minimum near 67° is a minimum in the farside scattering, caused by the interference of the refracted $l_<$ and $l_>$ contributions, i.e. it is an Airy minimum.

Few instances of actual light heavy-ion elastic scattering show refractive structures in such a visible way. Fig. 10.1 is an example of $^{16}O + ^{12}C$ elastic scattering at 608 MeV calculated with the potential in Table 3. The decomposition into nearside and farside amplitudes reveals that the structureless falloff beyond about 20° is a feature of the farside (and one would say that the scattering is "farside-dominated"). In this case, there is no clear evidence of Airy minima in the farside, except for a hint near 15°. If this were in fact an Airy minimum, arising from the interference of the two farside branches of the deflection function, the weakness of the interference probably would be due to the strong absorption of the $l_<$ part relative to the $l_>$ part; if the absorption were reduced (for instance, by decreasing the value of W_0 in the calculation) one would expect the $l_<$ contribution to become strong enough to interfere more efficiently with the $l_>$ contribution, so that the minimum should become deeper. This is indeed the case for the calculation shown in Fig. 10.1, and the enhancement of the 15° minimum caused by the artificially reduced absorption confirms its identification as an Airy minimum. The calculations with reduced W_0 show that the 15° minimum is the first Airy minimum in the angular distribution, i.e., it is the primary one, and the nuclear rainbow angle is then located at about 40°. This last result could also be obtained directly from the deflection function (3.9) by using the calculated phase shifts.

Next is an example of the use of the nearside–farside decomposition technique in a global interpretation of the $^{12}C + ^{12}C$ elastic scattering at energies where the 90° excitation function displays an interesting structure. Fig. 10.2 shows the data and the original (1974) interpretations. The enigma during all these years has been finding an explanation for the origin of the wide structures, particularly the minima between the elephants, and a confirmation of the reality of the proposed third pachyderm. The study [144] of the $^{12}C + ^{12}C$ excitation function was based on a previous optical model analysis [30] of complete angular distributions measured at $35\,\text{MeV} \leq E_{c.m} \leq 63\,\text{MeV}$, an

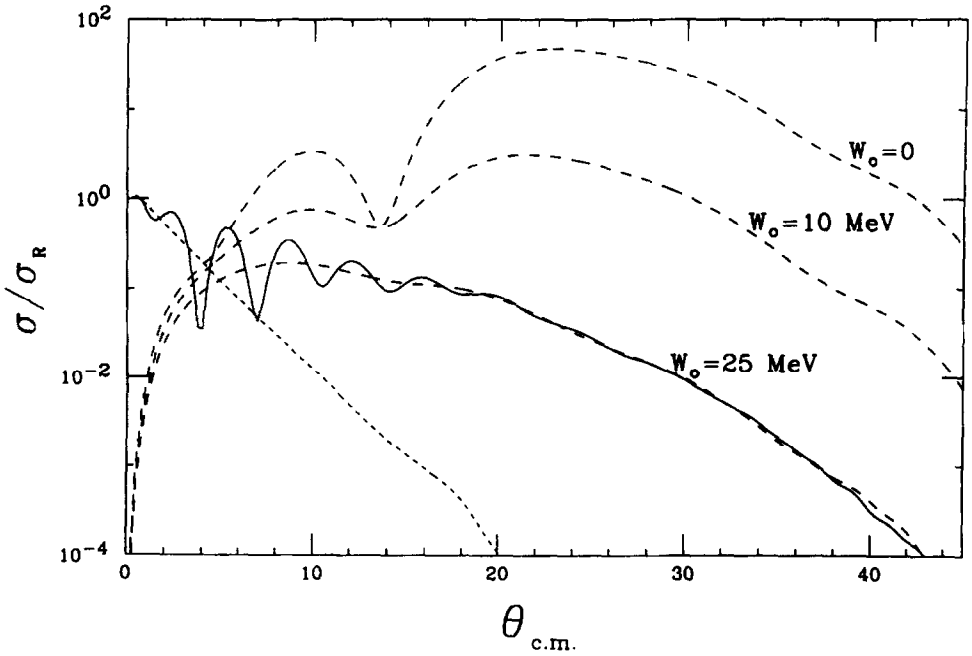

Fig. 10.1. Calculations for $^{16}O + ^{12}C$ scattering at 608 MeV. The solid curve (labelled $W_0 = 25$ MeV) is the differential cross section calculated with the potential that fits the measurements (parameters in Table 3); it has been decomposed into its nearside (dotted) and farside (dashed) contributions. The dashed curves labelled $W_0 = 10$ MeV and 0 show the effect on the farside from an artificial reduction of the absorption. The farside minimum near 14° becomes more evident as the absorption decreases, confirming its identification as an Airy minimum.

energy range which overlaps with the one for the excitation function. Fig. 10.3 shows the optical model fits to the measured angular distributions. In this analysis the potentials have the traditional Woods–Saxon shape and are strongly attractive and weakly absorptive; the parameters can be found in Table 3 for a few representative energies.

The general features of the data in Fig. 10.3 are extremely complex, particularly below about 120 MeV, because the Fraunhofer oscillations are not confined to the most forward angles but they extend over the complete angular range making it impossible to guess at the presence of Airy minima or maxima. Things are further complicated by the interference around 90° due to the identity of projectile and target, which overlaps with the Fraunhofer oscillations. The panorama is clarified when, after removing from the calculations the indistinguishability interference, only the farside is observed, as in Fig. 10.4. The main features in this plot are the sharp minima evolving from one energy to the next. These are higher order Airy minima (see Section 3.6) which move forward as the energy increases.

Since the angular distribution is symmetrical about 90° for identical particle systems, it is not possible from measurements at these energies alone to determine the order of the Airy minima. In particular, it is not possible to elucidate whether the last Airy minima observed near 90° at 126.7 MeV is or is not the primary one. In order to accomplish this one must appeal to the analyses of the data for higher energies and assume continuity. This has been done [30] and we have assigned the primary Airy minimum as the one indicated as A_1 in Fig. 10.4. Then A_2 is the secondary one, which crosses

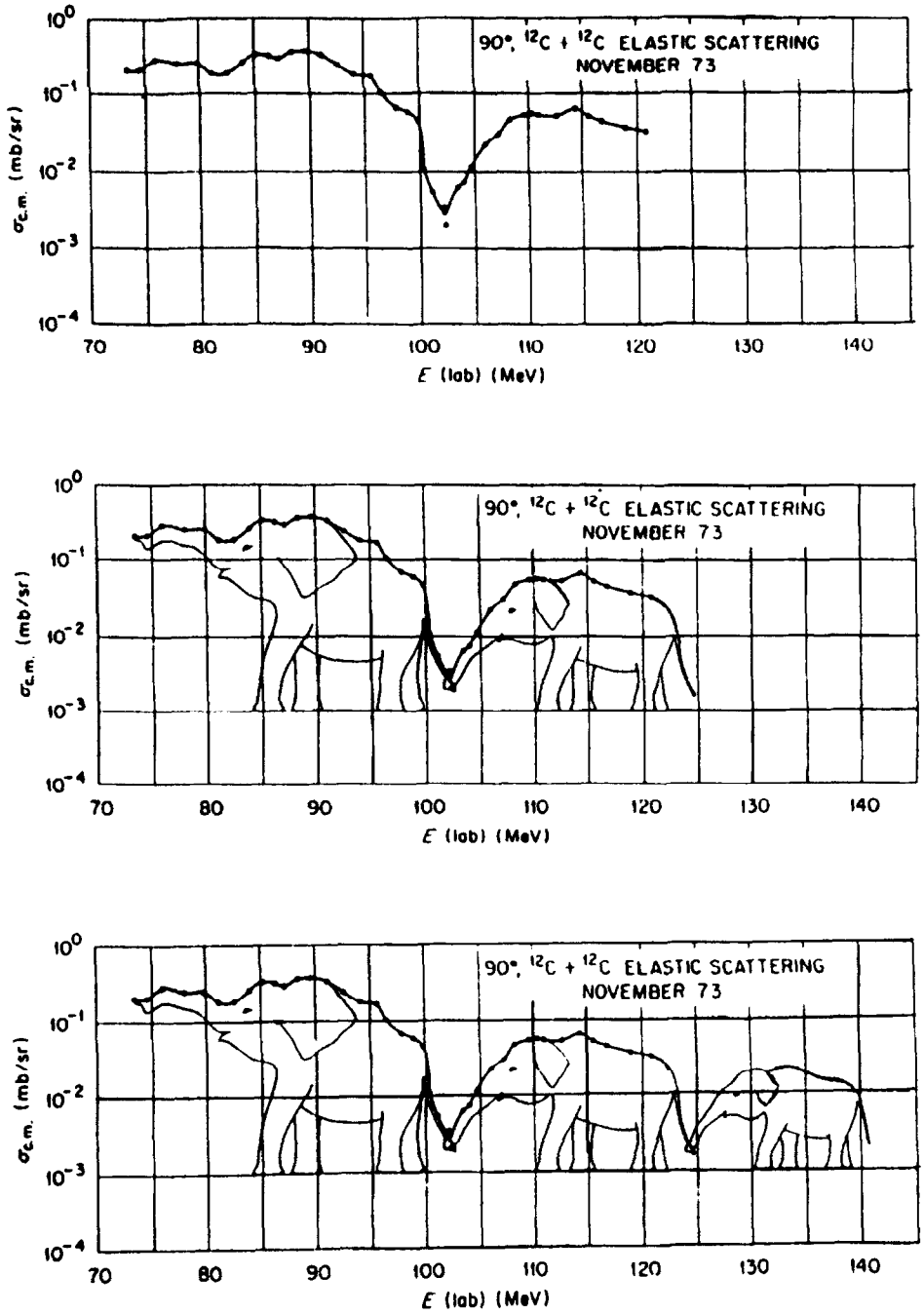

Fig. 10.2. The "elephant interpretation" [169] of the shape of the $^{12}C + ^{12}C$ 90° excitation function (cited in [144]).

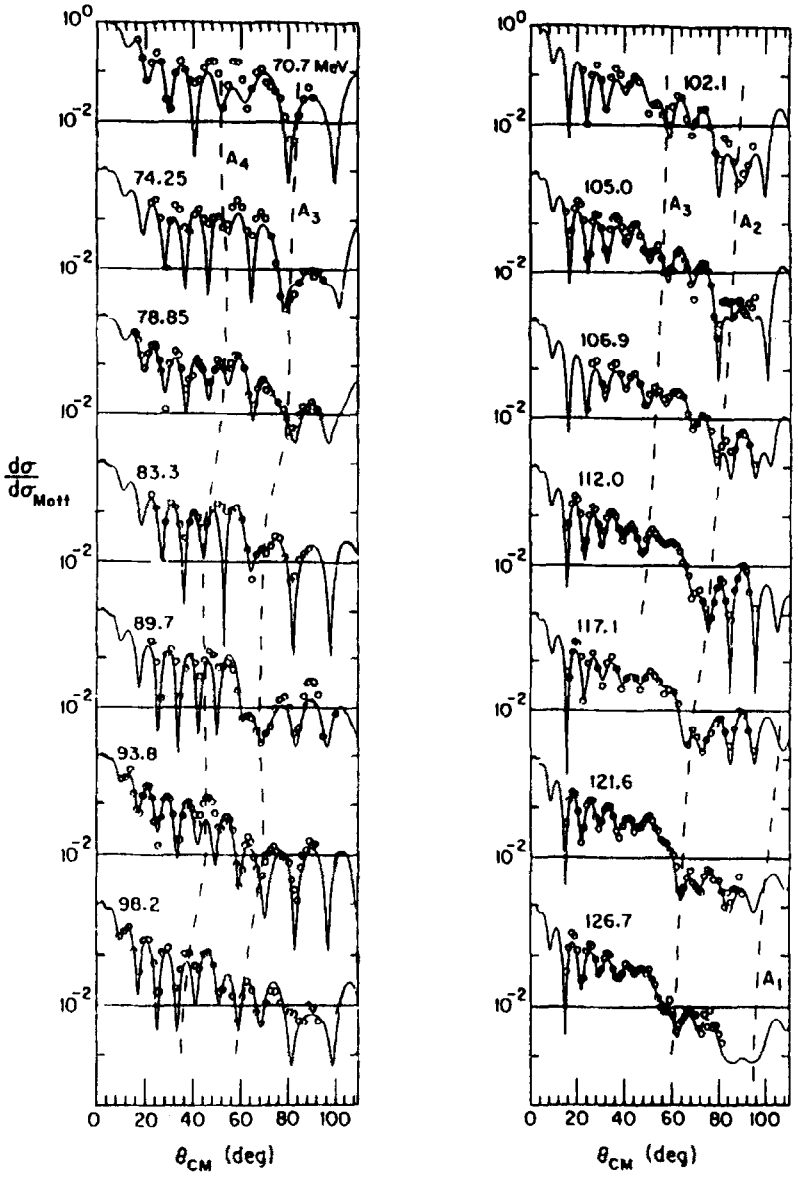

Fig. 10.3. The angular distributions for elastic $^{12}C+^{12}C$ scattering at incident energies between 71 and 127 MeV. The curves are calculations with phenomenological (WS) potentials. The dashed curves trace the angular positions of the Airy minima, identified as A_1 through A_4, being A_n the nth minimum forward of the rainbow angle (from [144]).

90° at about 100 MeV, and so on. Fig. 10.5 shows the observed evolution of the supernumerary minima with energy. Indicated are the ranges of energy and angles where the minima are deep enough to strongly affect the angular distribution.

After reaching this point in the analysis, some of the answers to the old questions concerning Fig. 10.2 should be evident. The gross structures in the excitation function are caused simply by the

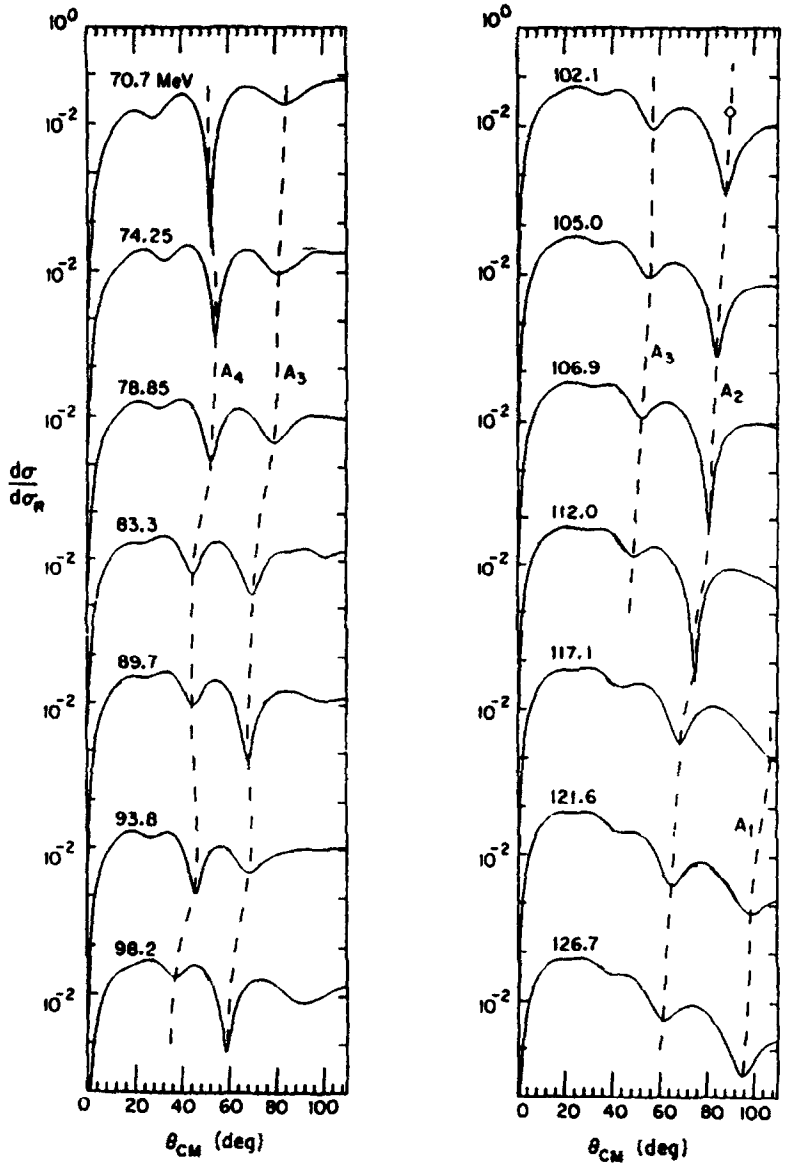

Fig. 10.4. The unsymmetrized farside cross sections produced by the potentials used in the calculations that were shown in Fig. 10.3. As in there, the dashed lines connect corresponding Airy minima (from [144]).

refractive structures passing through 90°, and the sharp minima between the elephants are the different Airy minima drifting by. In fact, at any angle (preferably at the larger angles in order to diminish the importance of the Fraunhofer interferences which also drift with energy) one would observe the same qualitative behaviour of the excitation function as at 90°. A recent series of measurements of the $^{12}C+^{12}C$ excitation function between 44° and 90° in the same energy interval [151] has been, indeed, successfully explained through these arguments [144]. The remaining question concerns

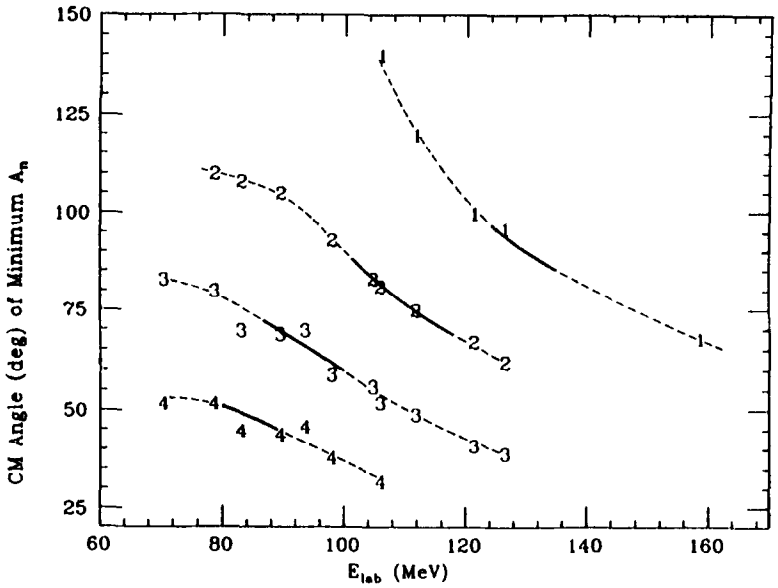

Fig. 10.5. The location of the A_n Airy minima shown in Fig. 10.3 and 10.4. The number indicates the order (n). The solid section in the curves signals the (E, θ) ranges where the minima are deep enough to significantly affect the measured cross section (from [144]).

part (c) in Fig. 10.2: is there a third elephant, not yet observed? The response from this analysis is positive and furthermore, it includes the prediction that there will *not* be a fourth elephant beyond. According to Fig. 10.5, the 90° minimum at about 130 MeV is the primary one, therefore after its passage the cross section should rise once more as the nuclear rainbow goes through, and this should be followed by the exponential falloff into the classically forbidden region. This prediction, inherently tied to the numbering of the minima and therefore to the assignment of a discrete optical potential family as the correct one, awaits its experimental confirmation.

The remarkable manifestation of refractive effects in the $^{12}C + ^{12}C$ elastic scattering channel just discussed is a consequence of the relatively low absorption shown by the system in this energy range. Since this seems to be a common feature for similar systems, such as $^{16}O + ^{16}O$ [120], the same explanation does interpret other well known cases of gross structures in oscillating excitation functions.

10.2. Semiclassical decomposition into subamplitudes

The semiclassical treatment to which we refer next attempts to understand all the structures in an angular distribution as arising from the interference between subamplitudes $f_i(\theta)$ which are smooth functions of θ. The scattering amplitude is therefore decomposed into the sum of components (3.8), whose interference is the cause for the observed oscillations in an angular distribution. The decomposition into nearside and farside scattering is the basic separation [74, 88], and the interference between these two subamplitudes is the origin of the Fraunhofer oscillations observed in all the light heavy-ion elastic scattering. In what follows, the farside component will be further decomposed

into semiclassical subamplitudes (or "trajectories") and the structure observed in the farside component will then be understood as an interference between these trajectories. The semiclassical (WKB) methods were originally elaborated by Knoll and Schaeffer [107] and have been put into practical use by McVoy and his collaborators [29, 73].

As a first example of the analysis we show in Fig. 10.6 the scattering of $^{12}C + ^{12}C$ at 159 MeV [29, 73]. In part (a) we display the unsymmetrized cross section and its decomposition into the nearside and farside amplitudes. For a more convenient visualization of structures in the subamplitudes, it is not $d\sigma/d\Omega$ that is plotted (as in Fig. 3.7), but $\ln(d\sigma/d\theta)$. It can be observed that the nearside and the farside components interfere producing the Fraunhofer oscillations forward of about 50°. Beyond this angle the nearside gets much weaker than the farside, the scattering becomes "farside-dominated" and the cross section is all due to the contributions from the farside. This component shows a dip at about 67° which is interpreted as the interference between farside subamplitudes; this is shown in Fig. 10.6(b), where the complex turning points $D(\theta)$ for the farside trajectories are displayed. Three trajectories are identified: R_-, R_+ and I_+. The first two are refractive trajectories (which for a purely real potential would describe rainbow scattering; that is, they would be the $l_<$ and $l_>$ contributions in the notation of Section 3.6). I_+ is a "diffractive" farside trajectory [72], which in this case is found to make a negligible contribution to the scattering. It can be observed that the rainbow angle (where R_- and R_+ tend to coalesce) is about 120°, and beyond this angle only one trajectory, R_+, is dominant. Fig. 10.6(c) shows the individual R_- and R_+ cross sections. As expected, each of them is a smooth function of θ, and their interference originates the dip at 67° which thus is a refractive (i.e. Airy) minimum. Even if the absorption in this case is relatively low, it suppresses the R_- contribution sufficiently so as to make the Airy minimum appear only weakly. However its appearance in the data (Fig. 6.1) is sufficiently noteworthy that it permitted the unambiguous determination of the potential parameters [27]. Fig. 10.6(b) shows that the R_+ (outer) trajectory explores the radial range between 3.5 and 7.5 fm, while R_- (inner) is significant only beyond about 50° (Fig. 10.6(c)) and therefore sensitive to the potential between 2 and 3 fm.

The next application of this type of decomposition is the already mentioned case of $^{16}O + ^{12}C$ scattering at 608 MeV, where the analysis has encountered severe (but anyhow interesting) ambiguities. As described in Section 7.3, this system shows a particular type of ambiguity since it can be described by a weakly absorbing (shallow-W) potential or by a continuously ambiguous family of strongly absorbing (deep-W) potentials. Fig. 10.7 shows the results of the semiclassical decomposition for the shallow-W potential. In Fig. 10.7(a), the cross section is decomposed into the nearside and farside components, similar to what is shown in Fig. 10.1. In Fig. 10.7(b) the complex turning points indicate that, as in the 159 MeV case, three trajectories contribute to the farside, but in this system *all three* contribute importantly to this amplitude. In Fig. 10.7(c), R_- and R_+ have been combined into one R, which interferes with I_+. The primary Airy minimum is seen in $|R|^2$ at about 14°. However, at this angle I_+ is becoming dominant and manages to interfere with R so as to almost eliminate the Airy minimum from the farside. But then an interference between R_+ and I_+ seems to appear, extremely weak, in the farside cross section at about 24°. For this potential the farside subamplitudes explore the potential over a range of radii from about 2 to 7 fm.

Fig. 10.8 shows similar calculations for a "deep-W" potential. The topology for the turning point space is totally different from that encountered previously with the weakly absorbing potentials in Figs. 10.6 and 10.7. Fig. 10.8(b) shows that the strong absorption has completely suppressed the inner trajectories seen in Fig. 10.7(b) for the "weak-W" case, and the farside is now dominated by

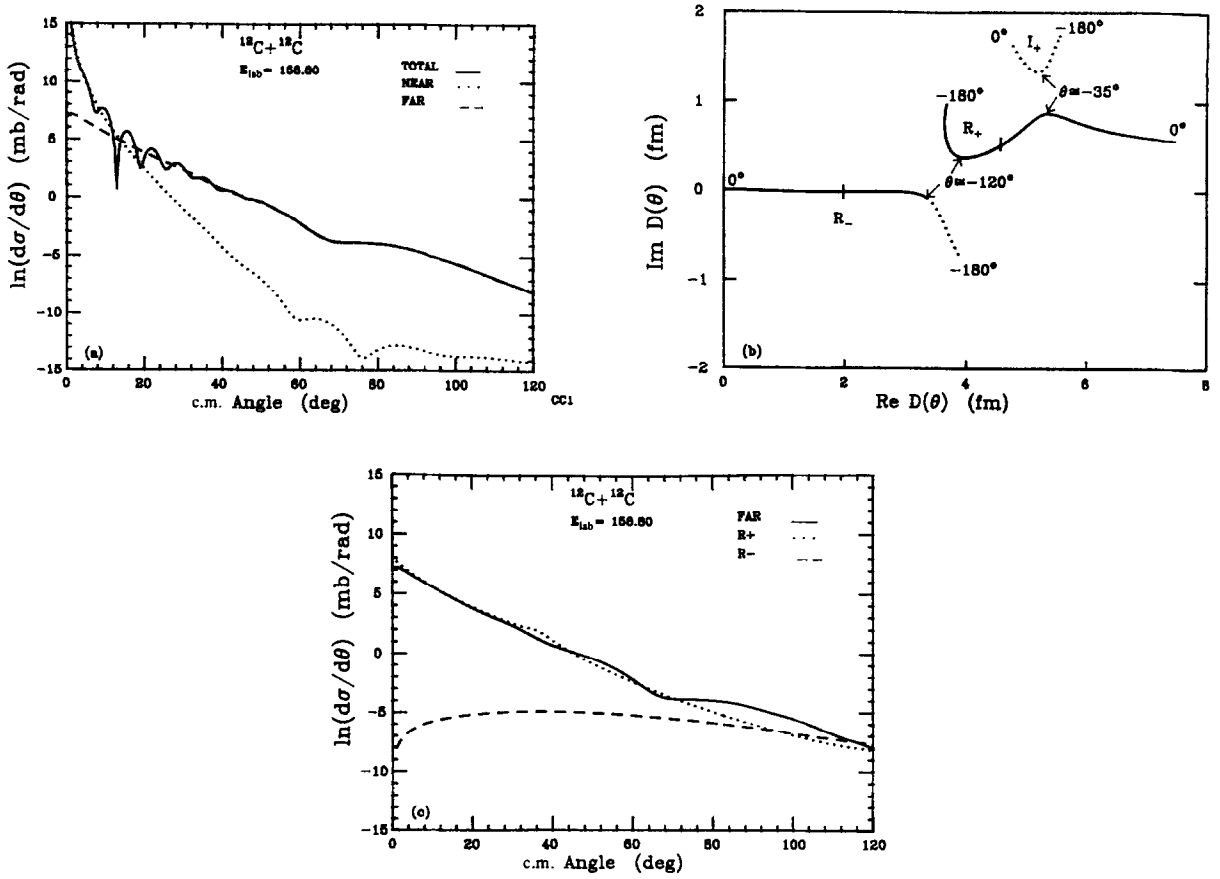

Fig. 10.6. (a) The total, nearside and farside unsymmetrized cross sections for the CC1 potential that fits the $^{12}C+^{12}C$ data at 158.8 MeV. (b) The farside complex turning points for the potential. The dotted lines indicate noncontributing portions of the trajectories. (c) The decomposition of the unsymmetrized farside cross section into contributions from individual subamplitudes (from [73]).

the single diffractive trajectory I_+ that senses the surface radii between 5 and 7 fm. This trajectory is capable of producing a farside amplitude (Fig. 10.8(c)) similar to that produced by the weak-W potential (Fig. 10.7(c)). Since the data display an exponential falloff without any noticeable structure, either description by itself presents an equally acceptable fit to the data.

These analyses have provided an explanation of the shallow- vs. deep-W ambiguity encountered in the optical model analyses of $^{16}O+^{12}C$ at 608 MeV: the weak-W solution is found to be "unique" because it is the result of a delicate balance among trajectories that sense the complete radial range. Conversely, the deep-W solution, sensitive only to the tail of the potential, presents the continuous ambiguity which is a feature in cases of strong absorption where the removal of flux from the inner regions of the potential restricts the sensitivity to the external region of the interaction.

A further example of the use of decomposition techniques is the investigation [35] of a non-monotonic real potential that fits the $^{16}O+^{16}O$ data at 350 MeV. A model-independent analysis (10-parameter-splines for the real part and Woods–Saxon shapes for the imaginary) of these data

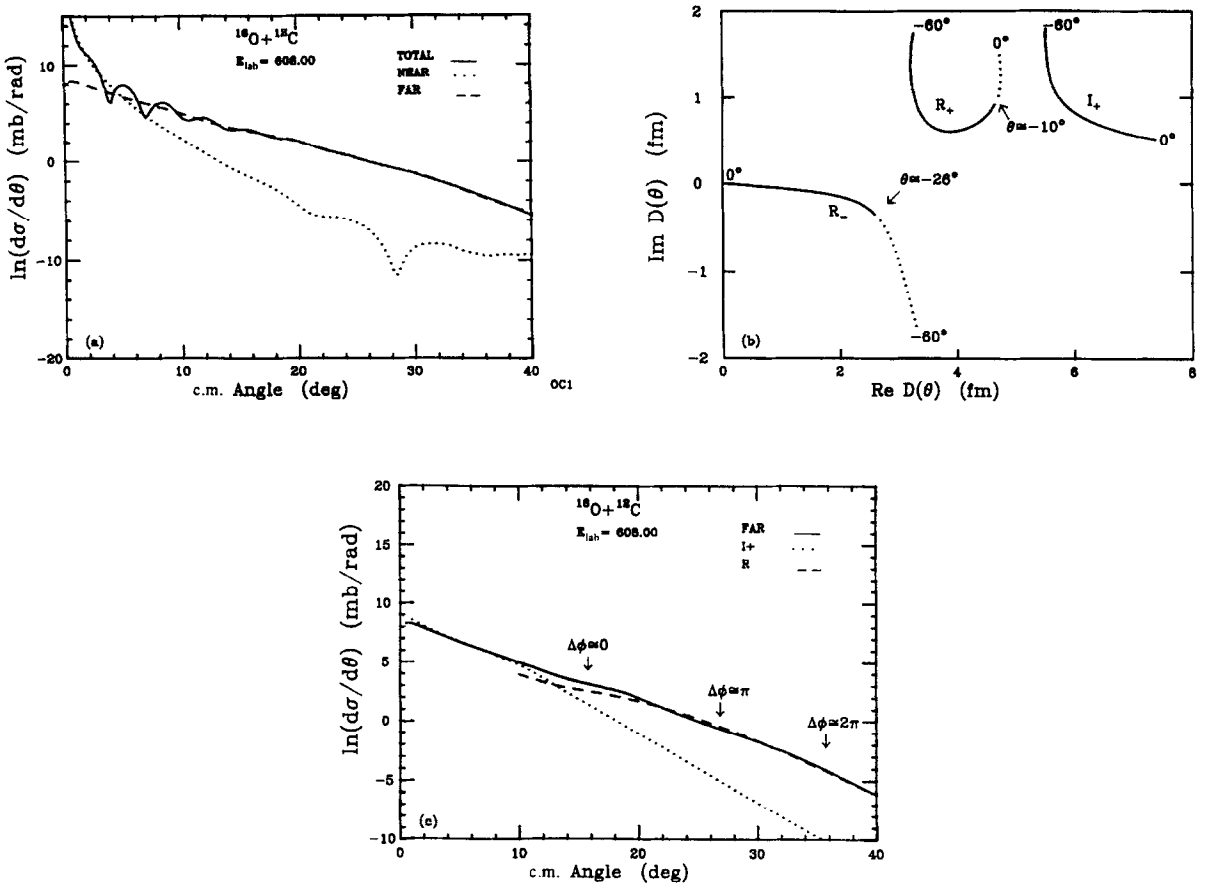

Fig. 10.7. (a) The total, nearside and farside cross sections for the shallow-W potential that fits the $^{16}O+^{12}C$ data at 608 MeV. (b) The farside complex turning points for the potential. The dotted lines indicate noncontributing portions of the trajectories. (c) The decomposition of the farside cross section into contributions from individual subamplitudes (from [73]).

[33] found three general types of real potential: potentials similar to Kondō's families A and B (see Section 7.2) and a shallower potential named "X", all shown in Fig. 9.1. The values of J_V were about 290 and 390 MeV fm^3 for types A and B, respectively, and 218 MeV fm^3 for type X. Potentials of type A put their first Airy minimum at 44° and potentials of type B interpret this minimum as the second Airy minimum. Potential X is too weak to put an Airy minimum at 44°; its own rainbow angle is at ~34°. How does potential X manage to fit the minimum in the data without an Airy minimum? The decomposition of the scattering amplitude into semiclassical trajectories [35] trace the cause to the nonmonotonic character of potential X. It indicates that *the oscillations* of potential X in regions inside $r \approx 3$ fm produce a complicated set of three trajectories which originate an amplitude that interferes with the one produced by the smooth potential at $r \geq 3$ fm, in order to locate a minimum precisely near 44°. The results from this analysis are a reminder that farside minima not of the rainbow type can be generated in complicated ways by unconventional potential shapes.

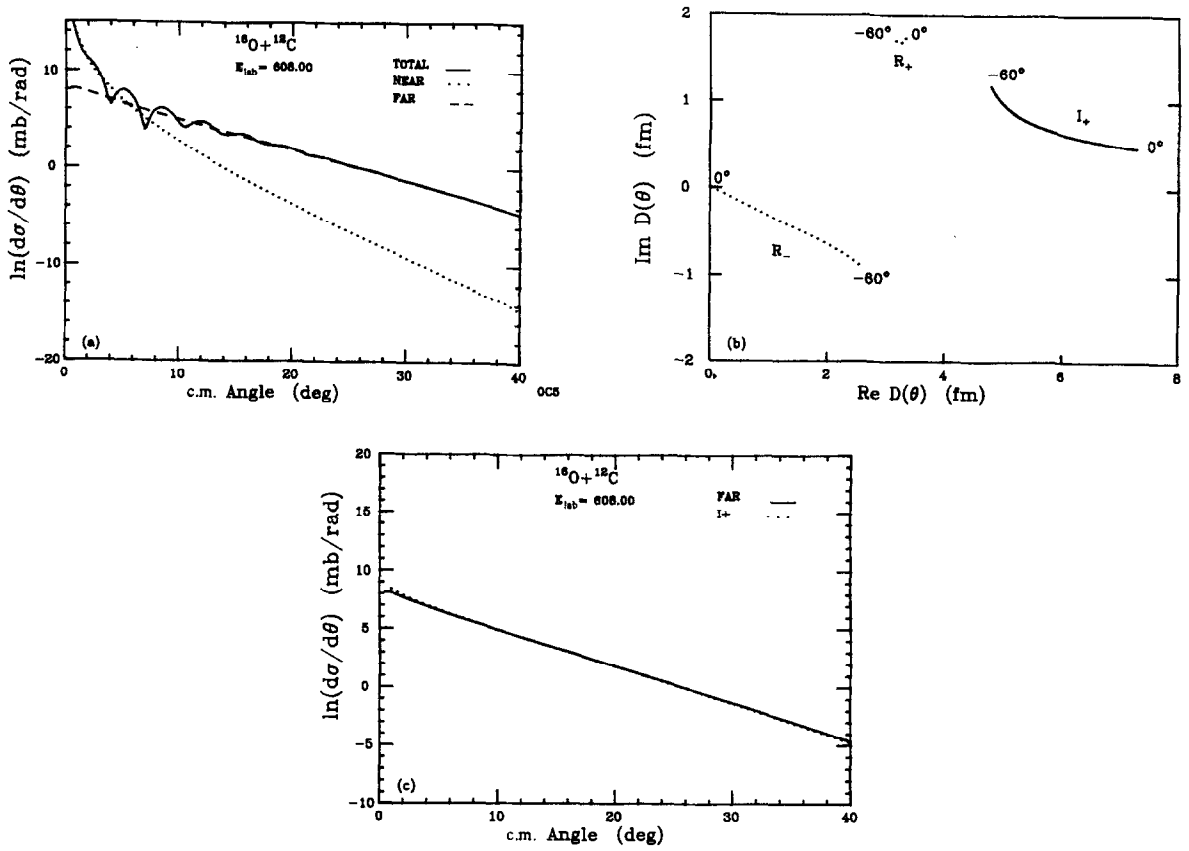

Fig. 10.8. (a) The total, nearside and farside cross sections for the deep-W potential that fits the $^{16}O + ^{12}C$ data at 608 MeV. (b) The farside complex turning points for the potential. The dotted lines indicate noncontributing portions of the trajectories. (c) The decomposition of the farside cross section into contributions from individual subamplitudes showing that the farside is completely dominated by the $I =$ contribution (from [73]).

11. Scattering of light "exotic" nuclei

There is now considerable interest in the scattering of "exotic" light heavy ions, produced as secondary radioactive ion beams (RIB) in new facilities now operational, being built or being planned [201]. As suggested by our use of the term "exotic", these ions introduce some unusual features which arise because they are situated away from the line of stability, which occurs at $N \simeq Z$ for light nuclei. This entails two characteristics: an excess of one kind of nucleon over the other, and a low binding energy. Such nuclei tend to have a few nucleons of one kind that are loosely bound and which may form a "halo" surrounding a more normal "core", as indicated by some density distributions shown in Fig. 11.1 that were calculated by use of a Hartree–Fock approximation [66].

A prototypical case is the isotope ^{11}Li. In the most naive view, two of the excess neutrons may be visualized as occupying the $0p_{1/2}$ shell-model orbit, with a total binding energy of only about 300 keV, compared to the 6 MeV needed to separate a neutron from the ^{9}Li "core". Consequently, the density distribution at large radii is dominated by these two neutrons. This constitutes a neutron

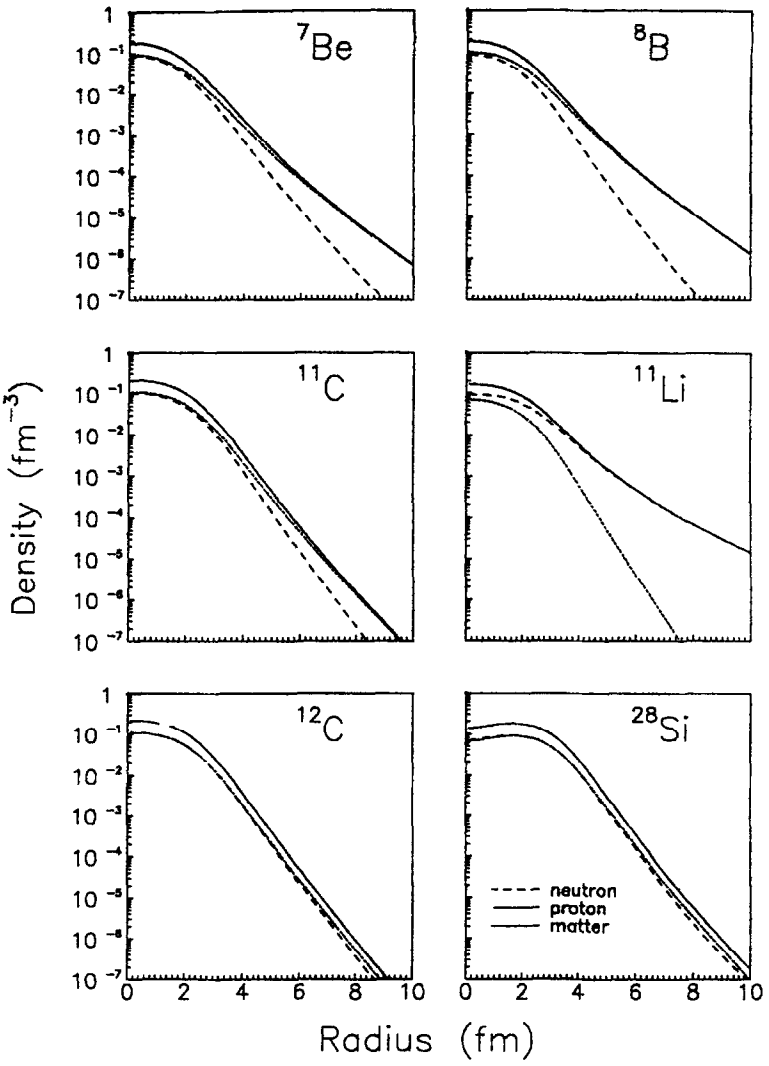

Fig. 11.1. Calculated density distributions [66] for some light nuclei, showing the tendency for a tail, or "halo", of the excess nucleons in the more exotic cases. The solid lines represent the sum of neutrons and protons, the dashed curves are for the neutrons and the dotted curves for the protons (from [66]).

"halo", which is estimated to have an RMS radius of about 6.5 fm, much larger than the radius of about 2.5 fm for the ^{9}Li core nucleus. (One must not be misled by the somewhat picturesque language used; the term "halo" does not mean that the $0p_{1/2}$ wavefunctions are localized at large radii. On the contrary, they are distributed throughout the nucleus but, due to the low binding, have long tails that dominate over the other contributions at large radii: see Fig. 11.1.)

In this review we have established that many light heavy-ion systems exhibit sufficient transparency for the cross sections to be dominated by farside scattering, sometimes with the appearance of a prominent (but damped) nuclear rainbow. The question here is what effect the presence of a halo

has on this transparency. It has been speculated that exotic nuclei like ^{11}Li would be associated with much stronger absorption due to break-up because of the weak binding of the excess nucleons. The scattering would then be diffractive, characteristic of strong absorption. However, this ignores the role of the halo in also enhancing the refractive property of the potential [188]. This question was studied carefully [90] in a comparison of the scattering at $E/A \simeq 60$ MeV of the exotic ^{11}Li and of the more normal ^{11}C by a ^{12}C target, for which some (poorly resolved) data exist [118]. Four, sometimes opposing, effects were identified in the scattering of ^{11}Li which are absent for ^{11}C. These arise from both the real and imaginary parts of (i) the extended tails of the complex folded optical potential due to the halo in the density distribution, and of (ii) the complex polarization potential which embodies the effects of the enhanced break-up of the weakly bound halo. Semiclassical expressions were derived which allow one to make rough estimates of these contributions. The net effect of the halo depends upon the details of the interactions, but it was concluded in this particular case that the scattering of ^{11}Li would not reveal greatly enhanced refraction compared to ^{11}C, and that its elastic scattering cross sections are similar to, and may be smaller than, those for ^{11}C. These conclusions are not in disagreement with analyses of the present quasi-elastic data [191].

There have been many theoretical studies of exotic nuclei, especially directed at their structure and including attempts to explain their above-normal radii. The latter were first deduced from measurements of their reaction cross sections at intermediate energies, using the semiclassical scattering theory of Glauber [201]. These cross sections were found to be significantly larger than those for normal nuclei.

Because of instrumental difficulties, so far there are rather few measurements of elastic scattering differential cross sections and those few tend to be contaminated by inelastic scattering because of the poor energy resolution obtained. This has impeded attempts to extract information on the optical potential, etc. We expect this situation to improve drastically in the near future, giving hope that the kind of information discussed in the rest of this review will become available. (Nonetheless, by their very nature, these measurements are difficult so that it seems unlikely that such experiments will achieve the precision obtained with normal beams.)

The pioneering experiments of Kolata et al. [118], conducted with beams of energy $E/A \simeq 60$ MeV, compared the scattering from a ^{12}C target of ^{11}Li with mean $E = 637$ MeV and of ^{11}C with mean $E = 620$ MeV. The energy resolution that could be achieved was poor so that the "elastic" data included inelastic scattering to a number of excited states. The contamination was least at the most forward angles because of the predominance of the elastic at those angles, but it is estimated to become comparable to, or larger than, the elastic cross section at the larger angles. Consequently, it has been difficult to reach more than qualitative conclusions about the properties of the optical potential, although many attempts have been made, both microscopic (see, for example, [202, 66, 105, 46]), and phenomenological [146] (but see [191]).

One conclusion, however, seems well established. It is that a good description of the ^{11}Li scattering can be obtained by using a folding model for the real potential, based upon the kind of interaction that we have seen to be successful for other, more normal light heavy-ions, provided a realistic density, with a halo tail, is used and some account is taken of the very important dynamic polarization potential (DPP) due to break-up. (This is analogous to the treatment of ^{6}Li scattering described in Section 6.3.3.)

One such treatment [105] was based upon Khoa's BDM3Y1 density-dependent interaction and his treatment of the knock-on exchange. A phenomenological polarization potential, chosen to reproduce

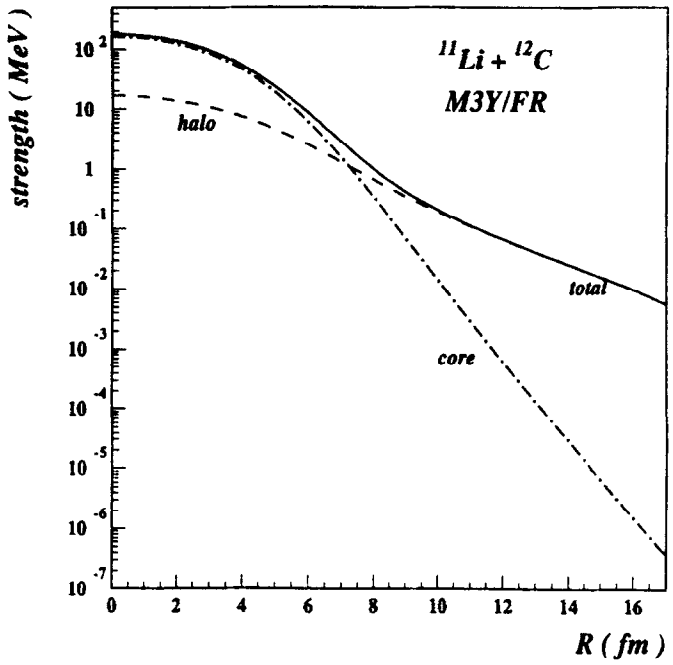

Fig. 11.2. Real folded potential for $^{11}Li + ^{12}C$, also showing the separate contributions from the ^{9}Li "core" nucleus and from the "halo" neutrons (from [46]).

the results of an explicit calculation of break-up effects [207], was added. This had a repulsive real part, and an attractive imaginary part of comparable strength. The main imaginary potential was represented by a Woods–Saxon term in which only the radius was allowed to change. Some measure of the inelastic contribution to the measured cross section was estimated using the DWBA. Good agreement with the data was realised for both ^{11}Li and ^{11}C on ^{12}C.

Another detailed discussion [46] made use of the M3Y interaction with a finite-range treatment of the exchange, as well as one based directly upon the G-matrix calculation of [95], using both real and imaginary parts and a Gaussian form factor. The interaction was checked against other data for α and ^{6}Li scattering from ^{12}C and ^{28}Si at various energies. An example of the real folded potential for $^{11}Li + ^{12}C$ is shown in Fig. 11.2, illustrating the separate contributions from the halo and from the core of ^{11}Li. Fig. 11.3 indicates that this potential gives reasonable agreement with the measurements on $^{11}Li + ^{12}C$ scattering after some estimate of the inelastic scattering was added. Attempts to fit the data for $^{11}Li + ^{28}Si$ at $E/A = 29$ MeV [127] were less successful.

Both analyses just described emphasize (as had been stressed earlier [188]) the important role played by the reaction cross section in helping to determine the optical potential.

One persistent failure appears in all attempts to reproduce these data using conventional potentials. Theoretically a sharp, deep minimum in the angular distribution is always predicted near 3° (see Fig. 11.3, for example) while the measurements indicate a peak near 2.5°. A fit to these forward angle data *can* be obtained, either phenomenologically [146] or by inversion (Section 9.2) [57]. In both cases, it requires a real potential with a surprizingly large and long tail which can affect the scattering to small angles. This is much stronger than the folding models predict even with the density

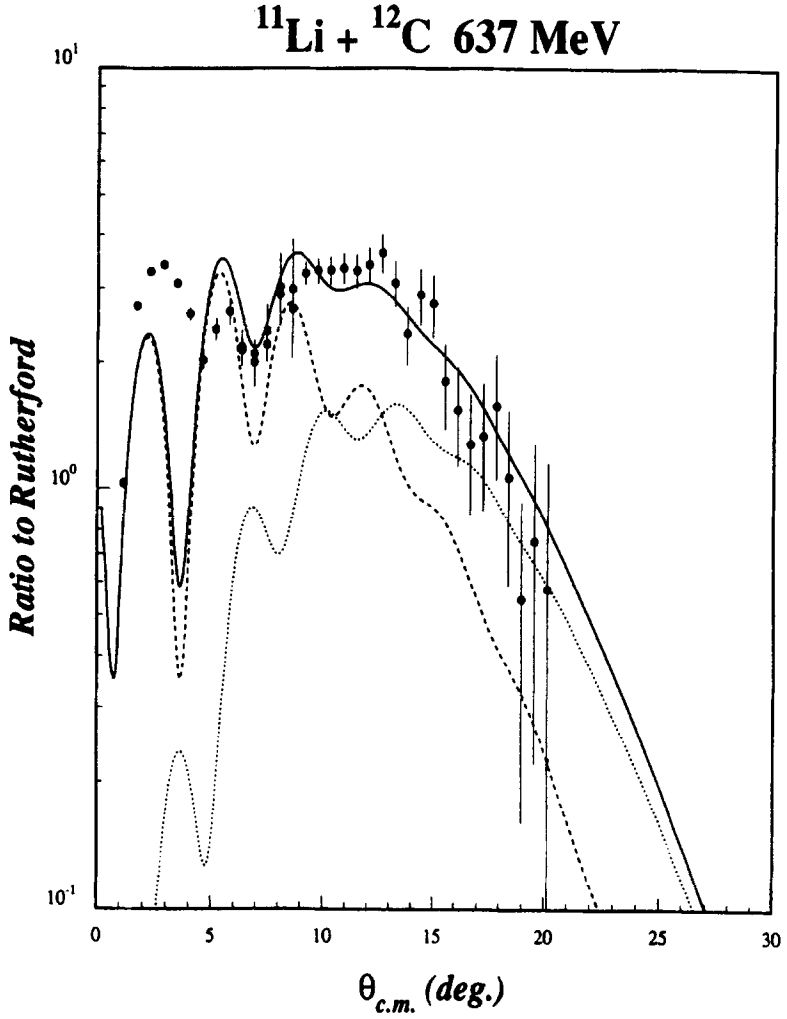

Fig. 11.3. Scattering cross sections produced using the potential shown in Fig. 11.2. The dashed curve represents the true elastic scattering, the dotted curve is an estimate of the inelastic contamination, while the solid curve is their sum, compared to the measured cross sections of [118] (from [46]).

distribution having a neutron halo. However, it seems possible that this apparent discrepancy at small angles is spurious, perhaps because some ^{9}Li ions resulting from break-up have been included at these forward angles where it is more difficult to discriminate against them.

A few other measurements have been reported. A popular target is ^{12}C, which has been used to scatter beams of ^{7}Be and ^{8}B at $E/A = 40$ MeV [165], as well as ^{12,14}Be at $E/A \simeq 57$ MeV [208]. The results in both cases include contamination of the elastic scattering by inelastic events. A folding model has been applied to the first pair of measurements, using realistic Hartree–Fock density distributions folded with the M3Y interaction and taking account of the finite range in the knock-on exchange terms [66]. Only a phenomenological analysis has been applied to the second pair of measurements.

12. Quasi-molecular resonances

The importance of this topic in the present context is that the observation of quasi-molecular resonances in a given l-wave, together with the (l-dependent) requirements imposed by the Pauli principle, demand a minimum number of radial nodes in the relative motion wavefunction. In turn, this requires that the potential be of a certain minimum depth. These depths turn out to correspond to the deep potentials that we have found are needed to describe the scattering at much higher energies, thus linking the two energy regions and providing a unified picture of the nucleus–nucleus interaction. Such a unification of bound states, resonances and continuum scattering has been achieved in a number of cases for α-particle plus target systems (for a recent example of $\alpha + {}^{16}O$, see [2]).

The mean field U_E as defined in the reaction theory of Feshbach (Section 4.4), which we have adopted to provide theoretical underpinning for our more intuitive models, sustains bound states ($E < 0$) as well as scattering states ($E > 0$). Correspondingly, our folded potentials, which represent the real first term of the Feshbach field (4.5), also sustain bound states. Quasi-bound states can be observed with $E > 0$ but will be confined to energies in the vicinity of the top of the (l-dependent) barrier resulting from the combined nuclear plus Coulomb plus centrifugal potentials. Those which have energies significantly below the top of the corresponding barrier, so the barrier penetrability has become very small, have very narrow widths and are not easily observed in the scattering, but those with energies in the vicinity of the barrier top can manifest themselves as resonances. As the energy moves up, these shape resonances rapidly become broad and again are not easily observed.

This part of the interaction only concerns the two nuclei while they remain in their ground states, the χ_{00} part of the wavefunction (4.4). The couplings to other states of the system will manifest themselves in at least providing an imaginary, absorptive potential, part of the dynamic polarization potential. This provides another source of width to the resonances, making them unobservable if the absorption is strong. So we can anticipate seeing them only when the absorption is "weak", which seems to be a characteristic of many of the light systems we are concerned with here, especially at the low energies corresponding to the barrier tops. Furthermore, if the couplings to a few particular excited states are strong, these must be considered explicitly and will result in the resonances having fine structure. In general, one must expect to see a group of resonances with a particular l value arising from each corresponding shape resonance in the bare potential. This l-value will track, within a few units, the peripheral l at a given energy.

Antisymmetrization between the two nuclei plays an important role in determining the form of the relative motion wavefunction of two clusters when bound (or quasi-bound). The number of quanta $Q = 2n + l$, where l is the orbital angular momentum and n is the number of radial nodes (excluding the origin and infinity), must exceed a certain threshold value, otherwise the states are Pauli-forbidden [87]. The allowed quantum numbers Q frequently are quite large. For example, $Q \geq 24$ for the system $^{16}O + {}^{16}O$ with both nuclei in their ground states. Relative motion with such a Q could not be sustained by a shallow potential, but can result from a deep potential of the kind discussed in the present review [116, 117, 149].

An interesting feature of these deep potentials is that the energies of the bound and resonant states are arranged into rotational bands (that is, the energies are proportional to $l(l+1)$), each band characterized by the quantum number Q. An example is shown in Fig. 12.1 from [115], and the origin of this property is discussed in [43].

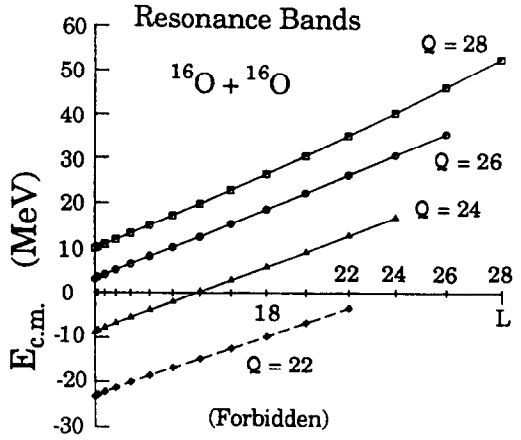

Fig. 12.1. The band structure of resonances and bound states in the real part of a Woods–Saxon-squared potential that is compatible with the low-energy scattering of $^{16}O + ^{16}O$. States with $Q = 22$ or less are forbidden by the Pauli principle (from [115]).

There is a very extensive literature on the subjects of cluster models and quasi-molecular resonances. We shall not even attempt to review this material, but refer the reader to a few recent reviews and conference proceedings [128, 92, 86, 87, 3, 6, 80]. Examples of applications to specific systems may be found in [44] ($^{12}C + ^{12}C$), [152] ($^{16}O + ^{12}C$) and [115] ($^{16}O + ^{16}O$).

13. Summary and discussion: What have we learnt?

During the last decade or so, we have extended considerably our understanding of the potential of interaction between two heavy-ions, especially two light heavy-ions. This progress has been stimulated in no small measure by experimental developments in providing accurate measurements of cross sections that cover large ranges of scattering angles and are often extremely small in magnitude. These have often revealed dramatic refractive characteristics such as nuclear rainbows. At the same time, there has been remarkable progress in our theoretical understanding of these phenomena. This understanding has resulted in our learning about the ion–ion interaction when the two nuclei overlap, and not just when their surfaces touch. In this Report, we have reviewed both the experimental and theoretical achievements.

An appealing physical picture, displaying overall consistency, has emerged. At its core is the concept of the folding model as accounting for the major part of the real potential (with theoretical justification arising from Feshbach's theory of nuclear reactions), together with progress in our understanding of the effective interaction between two nucleons embedded in a nuclear medium. One result of this is to settle the old and oft (perhaps poorly) posed question whether the ion–ion potential is "deep" or "shallow", in favour of the "deep" answer. One also concludes that the correction to the folding model (that is, the real part of the dynamic polarization potential (DPP) that accounts for couplings to other, nonelastic channels) is relatively small in most cases. (One exception occurs for the break-up of loosely bound nuclei like ^{6}Li, where the correction has been shown to be significant.) Progress in understanding the imaginary, absorptive part of the potential

(the imaginary part of the DPP) has been more limited. This is still treated phenomenologically in most cases, although one has discerned clues that it depends more sensitively upon the structural characteristics of individual systems. However, one conclusion is clear; the imaginary potential must be "weak" in some sense, otherwise the important refractive features of the scattering cannot be observed. It is weak if the flux along scattering trajectories that penetrate to the interior of the potential is not completely extinguished by absorption. Then this interior region has some influence upon the scattering, revealed by the observation of the refractive features.

The semiclassical decomposition of the observed angular distributions for elastic scattering has proven to be a powerful tool for understanding the physical characteristics underlying them. The nearside–farside ("Fraunhofer") interference oscillations at forward angles give us information about the potential experienced in peripheral collisions. At larger angles, farside scattering dominates if the absorption is not too strong, corresponding to somewhat closer collisions. If the absorption is sufficiently weak, two trajectories contribute to the farside scattering, which then exhibits rainbow features, namely Airy maxima and minima. These are influenced by the potential in the interior, and, given data of sufficient extent that the order of the Airy pattern can be determined, the potential family can be found without ambiguity.

One consequence of this kind of interpretation is to determine that the effective nucleon–nucleon interaction required for use in a folding model of the potential should be weaker in the nuclear interior than it is in the surface. This property is conveniently represented by making it dependent upon the density of the surrounding nuclear material. The effective, attractive interaction becomes weaker as the density increases, a requirement already anticipated in order for nuclear matter to saturate. The need for such a property was already evident from the analysis of the scattering of medium energy alpha particles which displayed similar rainbow characteristics, and culminated in the construction of effective interactions constrained to reproduce the saturation parameters (binding energy and saturation density) of nuclear matter in a Hartree–Fock calculation. These interactions differed in the degree of density-dependence, and hence in the values of the incompressibility of nuclear matter associated with them. However, they could be further constrained when applied to the scattering of α-particles and light heavy-ions, thus providing evidence for the appropriate value of the incompressibility.

The refractive phenomena just discussed only appear clearly when certian dynamic conditions are met. In particular, there is an energy window. If the energy is too low, the scattering is dominated by the Fraunhofer pattern, and any rainbow features remain in the unphysical region (angles greater than 180°). As the energy is raised, the refractive features move forward where they can be observed. However, if the energy increases too much, they move even further forward and become superimposed on the Fraunhofer pattern, where they become more difficult to interpret. Thus observations in the intermediate region are more likely to be profitable in revealing this kind of information, although careful analysis at lower and higher energies, accompanied by a requirement that the results should how a reasonable continuity in energy, can extend the energy range significantly.

"Continuity" plays an important role in another context, namely that too much weight should not be placed upon results obtained from just one set of data. Besides the possibility that some idiosyncracy of the data may be biassing the analysis, almost inevitably there remains some ambiguity associated with a single set of data. Consequently, we believe that an interpretation based upon data for a range of energies and/or a number of similar nuclear systems may contain more "physical" truth than a very good fit to one specific data set.

The real potentials that have been inferred for these light heavy-ion systems also have about the correct depth to sustain "molecular" bound states and resonances with the proper number of radial nodes to be consistent with the Pauli exclusion principle. Many such quasi-molecular resonances have been observed at low energies. A few applications of the potential model have been made, but much work remains to be done. These deep potentials also describe the low energy elastic scattering and fusion data measured at Yale and Saclay in the 1970s, as well as the more recent measurements at higher energies that have been discussed in this review. Thus we see an example of "continuity" over a wide range of energies for applications of the models discussed here.

The kind of refractive effects discussed here will also have their counterparts in nonelastic reactions. A few applications of these ideas have been made, but we leave those for the future.

Acknowledgements

We are indebted to many colleagues for helpful discussions on this subject during the past many years. In particular, we would like to acknowledge numerous enlightening collaborations with Kirk W. McVoy. We are grateful to Yosio Kondō for carefully reading the whole manuscript. The work at Universidad Nacional Autónoma de México was supported by CONACYT-México, Grant 3173E. Oak Ridge National Laboratory is managed by Lockheed Martin Energy Research Corporation for the US Department of Energy under Contract No. DE-AC05-96OR22464. Theoretical nuclear physics research at the University of Tennessee is supported by the US Department of Energy through Contract Nos. DE-FG05-93ER40770 and DE-FG05-87ER40461.

References

[1] H. Abele et al., Z. Phys. A 326 (1987) 373.
[2] H. Abele and G. Staudt, Phys. Rev. C 47 (1993) 742.
[3] U. Abbondanno and N. Cindro, Int. J. Mod. Phys. E 2 (1993) 1.
[4] L.J. Allen, L. Berge, C. Steward, K. Amos, H. Fiedeldey, H. Leeb, R. Lipperheide and P. Frobrich, Phys. Lett. B 298 (1993) 36.
[5] N. Anantaraman, H. Toki and G.F. Bertsch, Nucl. Phys. A 398 (1983) 269.
[6] G.S. Anagnostatos and W. von Oertzen, Z. Phys. A 349 (1994) 195.
[7] N. Austern and J.S. Blair, Ann. Phys. (NY) 33 (1965) 15.
[8] A.J. Baltz, S.K. Kauffman, N.K. Glendenning and K. Pruess, Phys. Rev. Lett. 40 (1978) 20.
[9] A.J. Baltz, N.K. Glendenning, S.K. Kauffman and K. Pruess, Nucl. Phys. A 327 (1979) 221.
[10] D. Baye, Phys. Rev. Lett. 58 (1987) 2738.
[11] D. Baye, G. Levai and J.-M. Sparenberg, Nucl. Phys. A 599 (1996) 435.
[12] G. Barnitzky, A. Blazevic, H.G. Bohlen, J.M. Casandjian, M. Chartier, H. Clement, B. Gebauer, A. Gillibert, Th. Kirchner, Dao T. Khoa, A. Lepine-Szily, W. Mittig, W. von Oertzen, A.N. Ostrowski, P. Roussel-Chomaz, J. Stiegler, M. Wilpert and Th. Wilpert, Phys. Lett. B 365 (1996) 23.
[13] H.A. Bethe, Ann. Rev. Nucl. Sci. 21 (1971) 93.
[14] G. Bertsch, J. Borysowicz, H. McManus and W.G. Love, Nucl. Phys. A 284 (1977) 399.
[15] C. Beck, Y. Abe, N. Aissaoui, B. Djerroud and F. Haas, Phys. Rev. C 49 (1994) 2618.
[16] H.G. Bingham, M.L. Halbert, D.C. Hensley, E. Newman, K.W. Kemper and L.A. Charlton, Phys. Rev. C 11 (1975) 1913.
[17] H.G. Bohlen, M.R. Clover, G. Ingold, H. Letau and W. von Oertzen, Zeit. Phys. A 308 (1982) 121.

[18] H.G. Bohlen, X.S. Chen, J.G. Cramer, P. Frobich, B. Gebauer, H. Lettau, A. Micziaka, W. von Oertzen, R. Ulrich and T. Wilpwert, Z. Phys. A 322 (1985) 241.
[19] H.G. Bohlen, E. Stiliaris, B. Gebauer, W. von Oertzen, M. Wilpwert, Th. Wilpwert, A. Ostrowski, Dao.T. Khoa, A.S. Demyanova and A.A. Oglobin, Z. Phys. A 346 (1993) 189.
[20] F.A. Brieva, Phys. Lett. B 76 (1978) 533.
[21] M.E. Brandan and A. Menchaca-Rocha, Phys. Rev. C 23 (1981) 1272.
[22] D.M. Brink and G.R. Satchler, J. Phys. G 7 (1981) 43.
[23] M.E. Brandan, Phys. Rev. Lett. 49 (1982) 1132.
[24] M.E. Brandan, J. Phys. G 9 (1983) 197.
[25] D.M. Brink, Semi-Classical Methods for Nucleus–Nucleus Scattering (Cambridge Univ. Press, Cambridge, 1986).
[26] M.E. Brandan, A. Menchaca-Rocha, M. Buenerd, J. Chauvin, P. DeSaintignon, G. Duhamel, D. Lebrun, P. Martin, G. Perrin and J.Y. Hostachy, Phys. Rev. C 34 (1986) 1484.
[27] M.E. Brandan, Phys. Rev. Lett. 60 (1988) 784.
[28] M.E. Brandan and G.R. Satchler, Nucl. Phys. A 487 (1988) 477.
[29] M.E. Brandan, S.H. Fricke and K.W. McVoy, Phys. Rev. C 38 (1988) 673.
[30] M.E. Brandan, M. Rodríguez-Villafuerte and A. Ayala, Phys. Rev. C 41 (1990) 1520.
[31] M.E. Brandan, S. Soberano, E. Belmont-Moreno, A Menchaca-Rocha, M. Gonin, R. Wada and J.B. Natowitz, Phys. Rev. C 42 (1990) 2236.
[32] R.A. Broglia and A. Winther, Heavy-Ion Reactions (Addison-Wesley, Redwood City, 1991).
[33] M.E. Brandan and G.R. Satchler, Phys. Lett. B 256 (1991) 311.
[34] M.E. Brandan and K.W. McVoy, Phys. Rev. C 43 (1991) 1140.
[35] M.E. Brandan, K.W. McVoy and G.R. Satchler, Phys. Lett. B 281 (1992) 185.
[36] M.E. Brandan, in: Low Energy Nuclear Dynamics, eds. Yu. Oganessian, W. von Oertzen and R. Kalpakchieva (World Scientific, Singapore, 1995) p. 399.
[37] M.E. Brandan, H. Chehime and K.W. McVoy, Phys. Rev. C (March 1997), in press.
[38] M.E. Brandan and K.W. McVoy, Phys. Rev. C (March 1997), in press.
[39] B. Buck, H. Friedrich and C. Wheatley, Nucl. Phys. A 275 (1977) 246.
[40] M. Buenerd, J. Pinston, J. Cole, C. Guet, D. Lebrun, J.M. Loiseaux, P. Martin, E. Monnand, J. Mougey, H. Nifenbecker, R. Ost, P. Perrin, Ch. Ristori, P. de Saintignon, F. Schussler, L. Carlen, H.A. Gustafsson, B. Jakobsson, T. Johansson, G. Jonsson, J. Krumlinde, I. Otterlund, H. Ryde, B. Schroder, G. Tibell, J.B. Bondorf and O.B. Nielsen, Phys. Lett. B 102 (1981) 242.
[41] M. Buenerd, P. Martin, R. Bertholet, C. Guet, M. Maurel, J. Mougey, H. Nifenecker, J. Pinston, P. Perrin, F. Schussler, J. Julien, J.P. Bondorf, L. Carlen, H.A. Gustaffson, B. Jacobsson, T. Johansson, P. Kristiansson, O.B. Nielsen, A. Oskarsson, I. Otterlund, H. Ryde, B. Schroder and G. Tibell, Phys. Rev. C 26 (1982) 1299.
[42] M. Buenerd, A. Lounis, J. Chauvin, D. Lebrun, P. Martin, G. Duhamel, J.C. Gondrand and P. De Saintignon, Nucl. Phys. A 424 (1984) 313.
[43] B. Buck, J.A. Spiers and A.C. Merchant, J. Phys. A 22 (1989) 3477.
[44] B. Buck, P.D.B. Hopkins and A.C. Merchant, Nucl. Phys. A 513 (1990) 75.
[45] F. Capuzzi and C. Mahaux, Ann. Phys. (NY) 239 (1995) 57.
[46] F. Carstoiu and M. Lassaut, Nucl. Phys. A 597 (1996) 269.
[47] L.T. Chua, F.D. Becchetti, J. Jänecke and F.L. Milder, Nucl. Phys. A 273 (1976) 243.
[48] J.M. Cornwall and M.A. Ruderman, Phys. Rev. 128 (1962) 1474.
[49] P.W. Coulter and G.R. Satchler, Nucl. Phys. A 293 (1977) 269.
[50] A.J. Cole, W.D.M. Rae, M.E. Brandan, A. Dacal, B.G. Harvey, R. Legrain, M.J. Murphy and R.G. Stokstad, Phys. Rev. Lett. 47 (1981) 1705.
[51] J. Cook, At. Data Nucl. Data Tables 26 (1981) 19.
[52] J. Cook, H.J. Gils, H. Rebel, Z. Majka and H. Klewe-Nebenius, Nucl. Phys. A 388 (1982) 173.
[53] J. Cook and K.W. Kemper, Arabian J. Sci. Eng. 8 (1983) 331.
[54] S.G. Cooper, M.A. McEwan and R.S. Mackintosh, Phys. Rev. C 45 (1992) 770.
[55] S.G. Cooper, M.A. McEwan and R.S. Mackintosh, Nucl. Phys. A 552 (1993) 401.
[56] S.G. Cooper and R.S. Mackintosh, Nucl. Phys. A 576 (1994) 308.
[57] S.G. Cooper and R.S. Mackintosh, Nucl. Phys. A 582 (1995) 283.

[58] R.M. DeVries, D.A. Goldberg, J.W. Watson, M.S. Zisman and J.G. Clover, Phys. Rev. Lett. 39 (1977) 450.
[59] R.M. DeVries and J.C. Peng, Phys. Rev. C 22 (1980) 1055.
[60] H. Dermawan, F. Osterfeld and V.A. Madsen, Phys. Rev. C 25 (1982) 180.
[61] A.C. Demiyanova, V.N. Bragin, A.A. Oglobin, A.L. Lebedev, J.M. Bang, S.A. Goncharov, S.N. Ershov, F.A. Gareev and P.P. Korovin, Phys. Lett. B 184 (1987) 129.
[62] R.M. Drisko, G.R. Satchler and R.H. Bassel, Phys. Lett. 5 (1963) 347.
[63] J.P. Elliott, A.D. Jackson, H.A. Mavromatis, E.A. Sanderson and B. Singh, Nucl. Phys. A 121 (1968) 241.
[64] M. El-Azab Farid and G.R. Satchler, Nucl. Phys. A 438 (1985) 525.
[65] A. Faessler, W.H. Dickoff, M. Trefz and M. Rhoades-Brown, Nucl. Phys. A 428 (1984) 271c.
[66] S.A. Fayans, O.M. Knyazkov, I.N. Kuchtina, Yu.E. Penionzhkevich and N.K. Skobelev, Phys. Lett. B 357 (1995) 509.
[67] H. Feshbach, Ann. Phys. (NY) 5 (1958) 357.
[68] H. Feshbach, Theoretical Nuclear Physics (Wiley, New York, 1992).
[69] H. Friedrich, Phys. Rep. 74 (1981) 209.
[70] M.A. Franey and P.J. Ellis, Phys. Rev. C 23 (1981) 787.
[71] W.E. Frahn, Diffractive Processes in Nuclear Physics (Oxford Univ. Press, Oxford, 1985).
[72] S.H. Fricke and K.W. McVoy, Nucl. Phys. A 467 (1987) 291.
[73] S.H. Fricke, M.E. Brandan and K.W. McVoy, Phys. Rev. C 38 (1988) 682.
[74] R.C. Fuller, Phys. Rev. C 12 (1975) 1561.
[75] D.A. Goldberg and S.M. Smith, Phys. Rev. Lett. 33 (1974) 715.
[76] D.A. Goldberg, S.M. Smith and G.F. Burdzick, Phys. Rev. C 10 (1974) 1362.
[77] D.A. Goldberg, Phys. Lett. B 55 (1975) 59.
[78] M. Golin, F. Petrovich and D. Robson, Phys. Lett. B 64 (1976) 253.
[79] L.J.B. Goldfarb and P. Nagel, Nucl. Phys. A 341 (1980) 494.
[80] W. Greiner, J.Y. Park and W. Scheid, Nuclear Molecules (World Scientific, Singapore, 1995).
[81] S.K. Gupta and K.H.N. Murthy, Z. Phys. A 307 (1982) 187.
[82] S.K. Gupta, S. Kailas, N. Lingappa and A. Shridhar, Phys. Rev. C 31 (1985) 1965.
[83] M.L. Halbert, C.B. Fulmer, S. Raman, M.J. Saltmarsh, A.H. Snell and P.H. Stelson, Phys. Lett. B 51 (1974) 341.
[84] H. Horiuchi, in: Clustering Aspects of Nuclear Structure, eds. J.S. Lilley and M.A. Nagarajan (Reidel, Dordrecht, 1985).
[85] J.Y. Hostachy, M. Buenerd, J. Chauvin, D. Lebrun, Ph. Martin, B. Bonin, G. Bruge, J.C. Lugol, L. Papineau, P. Roussel, J. Arvieux and C. Cerruti, Phys. Lett. B 184 (1987) 139.
[86] H. Horiuchi, Nucl. Phys. A 522 (1991) 257c.
[87] H. Horiuchi, in: Trends in Theoretical Physics, eds. P.J. Ellis and Y.C. Tang (Addison-Wesley, Reading, MA, 1991).
[88] M.S. Hussein and K.W. McVoy, Prog. Part. Nucl. Phys. 12 (1984) 103.
[89] M.S. Hussein, A.J. Baltz and B.V. Carlson, Phys. Rev. 113 (1984) 133.
[90] M.S. Hussein and G.R. Satchler, Nucl. Phys. A 567 (1994) 165.
[91] G. Igo, Phys. Rev. 115 (1959) 1665.
[92] K. Ikeda, K. Katori and Y. Suzuki, eds., Clustering Aspects in Nuclear Systems, J. Phys. Soc. Japan Suppl. 58 (1989).
[93] J.D. Jackson, Classical Electrodynamics (Wiley, New York, 1975) ch. 7.
[94] A.K. Jain, M.C. Gupta and C.S. Shastry, Phys. Rev. C 12 (1975) 801.
[95] J.P. Jeukenne, A. Lejeune and C. Mahaux, Phys. Rev. C 16 (1977) 80.
[96] K. Katori, T. Shimoda, T. Fukuda, S. Shimoura, A. Sakaguchi, M. Tanaka, T. Yamagata, N. Takahashi, H. Ogata, M. Kamimura and Y. Sakuragi, Nucl. Phys. A 480 (1988) 323.
[97] S.B. Khadkikar, L. Rikus, A. Faesser and R. Sartor, Nucl. Phys. A 369 (1981) 495.
[98] Dao Tien Khoa, Nucl. Phys. A 484 (1988) 376.
[99] D.T. Khoa, W. von Oertzen, A. Faessler, M. Ermer and H. Clement, Phys. Lett. B 260 (1991) 278.
[100] Dao T. Khoa and W. von Oertzen, Phys. Lett. B 304 (1993) 8.
[101] Dao T. Khoa, W. von Oertzen and H.G. Bohlen, Phys. Rev. C 49 (1994) 1652.
[102] Dao T. Khoa and W. von Oertzen, Phys. Lett. B 342 (1995) 6.

[103] Dao T. Khoa, W. von Oertzen, H.G. Bohlen, G. Bartnitzky, H. Clement, Y. Sugiyama, B. Gebauer, A.N. Ostrowski, Th. Wilpwert, M. Wilpwert and C. Langner, Phys. Rev. Lett. 74 (1995) 34.
[104] Dao T. Khoa, G.R. Satchler and W. von Oertzen, Phys. Rev. C 51 (1995) 2069.
[105] Dao T. Khoa, G.R. Satchler and W. von Oertzen, Phys. Lett. B 358 (1995) 14.
[106] Dao T. Khoa, W. von Oertzen and A.A. Ogloblin, Nucl. Phys. A 602 (1996) 98.
[107] J. Knoll and R. Schaeffer, Ann. Phys. (NY) 97 (1976) 307.
[108] T. Koeling and R.A. Malfliet, Phys. Rev. C 4 (1975) 181.
[109] A.M. Kobos, B.A. Brown, P.E. Hodgson, G.R. Satchler and A. Budzanowski, Nucl. Phys. A 384 (1982) 65.
[110] A.M. Kobos, B.A. Brown, R. Lindsay and G.R. Satchler, Nucl. Phys. A 425 (1984) 205.
[111] S. Kox, A. Gamp, R. Cherkaoui, A.J. Cole, N. Longequeue, J. Menet, C. Perrin and J.B. Viano, Nucl. Phys. A 420 (1984) 162.
[112] S. Kox, A. Gamp, C. Perrin, J. Arvieux, R. Bertholet, J.F. Braundet, M. Buenerd, Y. El-Masri, N. Longequeue and F. Merchez, Phys. Lett. B 159 (1985) 15.
[113] S. Kox, A. Gamp, C. Perrin, J. Arvieux, R. Bertholet, J.F. Braundet, M. Buenerd, R. Cherkaoui, A.J. Cole, Y. El-Masri, N. Longequeue, J. Menet, F. Merchez and J.B. Viano, Phys. Rev. C 35 (1987) 1678.
[114] A.M. Kobos, M.E. Brandan and G.R. Satchler, Nucl. Phys. A 487 (1988) 457.
[115] Y. Kondō, B.A. Robson and R. Smith, J. Phys. Soc. Japan Suppl. 58 (1989) 597.
[116] Y. Kondō, B.A. Robson and R. Smith, Phys. Lett. B 277 (1989) 310.
[117] Y. Kondō, F. Michel and G. Reidemeister, Phys. Lett. B 242 (1990) 340.
[118] J.J. Kolata, M. Zahar, R. Smith, K. Lamkin, M. Belbot, R. Tighe, B.M. Sherrill, N.A. Orr, J.S. Winfield, J.A. Winger, S.J. Yennello, G.R. Satchler and A.H. Wuosmaa, Phys. Rev. Lett. 69 (1992) 2631.
[119] A.F. Zeller, Y.-W. Lui, R.E. Tribble and D.M. Tanner, Phys. Rev. C 22 (1980) 1534.
[120] Y. Kondō, Y. Sugiyama, Y. Tomita, Y. Yamanouchi, H. Ikezoe, K. Ideno, S. Hamada, T. Sugimitsu, M. Hijiya and H. Fujita, Phys. Lett. B 365 (1996) 17.
[121] S. Kubono, K. Morita, M.H. Tanaka, M. Sugitani, H. Utsonimiya, H. Yonehara, M.-K. Tanaka, S. Shimoura, E. Takada, M. Fukada and K. Takimoto, Phys. Lett. B 127 (1983) 19.
[122] M. Lacombe, B. Loiseau, J.M. Richard, R. Vinh Mau, J. Cote, P. Pires and R. de Tourreil, Phys. Rev. C 21 (1980) 861.
[123] M. Lassaut and N. Vinh Mau, Nucl. Phys. A 391 (1982) 118.
[124] M. LeMere and Y.C. Tang, Phys. Rev. C 19 (1979) 391.
[125] M. LeMere, D.J. Stubeda, H. Horiuchi and Y.C. Tang, Nucl. Phys. A 320 (1979) 449.
[126] H. Leeb, W.A. Schnizer, H. Fieldeldey, S.A. Sofianos and R. Lipperheide, Inv. Prob. 5 (1989) 817.
[127] M. Lewitowicz, C. Borcea, F. Carstoiu, M.G. Saint-Layrent, A. Kordyasz, R. Anne, P. Roussel-Chomaz, R. Bimbot, V.Borrel, S. Dogny, D. Guillemaud-Mueller, A.C. Mueller, F. Pougheon, F.A. Gareev, S.N. Ershov, S. Lukyanov, Yu. Penionzhkevich, N. Skobelev, S. Tretyakova, Z. Dlouhy, L. Nosek and J. Svanda, Nucl. Phys. A 562 (1993) 301.
[128] J.S. Lilley and M.A. Nagarajan, eds., Clustering Aspects of Nuclear Structure (Reidel, Dordrecht, 1985).
[129] W.G. Love and L.W. Owen, Nucl. Phys. A 239 (1975) 74.
[130] W.G. Love, Phys. Lett. B 72 (1977) 4.
[131] J.V. Maher, M.W. Sachs, R.H. Siemssen, A. Weidinger and D.A. Bromley, Phys. Rev. 188 (1969) 1665.
[132] M.H. Macfarlane and S.C. Pieper, Argonne National Laboratory Report No. ANL-76-11 (1978).
[133] C. Mahaux, Microscopic Optical Potentials (Springer, Berlin, 1979) p. 1.
[134] C. Mahaux, The Interaction between Medium-Energy Nucleons in Nuclei (Am. Inst. Phys., New York, 1983) p. 20.
[135] C. Mahaux, H. Ngô and G.R. Satchler, Nucl. Phys. A 449 (1986) 354.
[136] C. Mahaux and R. Sartor, Adv. Nucl. Phys. 20 (1991) 1, and references therein.
[137] C. Mahaux and R. Sartor, Nucl. Phys. A 530 (1991) 303.
[138] C. Mahaux, K.T.R. Davies and G.R. Satchler, Phys. Rep. 224 (1993) 237.
[139] C. Mahaux and G.R. Satchler, Nucl. Phys. A 560 (1993) 5.
[140] V.A. Madsen and G.R. Satchler, Phys. Rev. C 48 (1993) 1221.
[141] R.S. Mackintosh and S.G. Cooper, Phys. Rev. C 47 (1993) 1716.
[142] J.A. McIntyre, K.H. Wang and L.C. Becker, Phys. Rev. 117 (1960) 1337.

[143] K.W. McVoy and G.R. Satchler, Nucl. Phys. A 417 (1984) 157.
[144] K.W. McVoy and M.E. Brandan, Nucl. Phys. A 542 (1992) 295.
[145] M.A. McEwan, S.G. Cooper and R.S. Mackintosh, Nucl. Phys. A 552 (1993) 401.
[146] M.C. Mermaz, Phys. Rev. C 47 (1993) 2213.
[147] S. Micek, Z. Majka, H. Rebel, H.J. Gils and H. Klewe-Nebenius, Nucl. Phys. A 435 (1985) 621.
[148] F. Michel, G. Reidemeister and Y. Kondō, Phys. Rev. C 51 (1995) 3290.
[149] F. Michel and G. Reidemeister, Phys. Rev. C 53 (1996) 3032.
[150] U. Mosel, Part. Nuclei 3 (1972) 297.
[151] A. Morsad, Zeit. Phys. A 338 (1991) 61; Universit'e Louis Pasteur, Strasbourg, Thèse (1986) unpublished.
[152] J.T. Murgatroyd, S.J. Bennett, B.R. Fulton, J.S. Pople, N.S. Jarvis, D.L. Watson, W.D.M. Rae, Y. Chan, D. DiGregorio, J. Scarpaci, J. Suro Perez and R.G. Stokstad, Phys. Rev. C 51 (1995) 2230.
[153] M.A. Nagarajan, C.C. Mahaux and G.R. Satchler, Phys. Rev. Lett. 54 (1985) 1136.
[154] A. Nadasen, M. McMaster, G. Gunderson, A. Judd, S. Villanueva, P. Scwandt, J.S. Winfield, J. van der Plicht, R.E. Warner, F.D. Becchetti and J.W. Janecke, Phys. Rev. C 37 (1988) 132.
[155] A. Nadasen, M. McMaster, M. Fingal, J. Tavormina, J.S. Winfield, R.M. Ronningen, P. Schwandt, F.D. Bechetti, J.W. Jänecke and R.E. Warner, Phys. Rev. C 40 (1989) 1237.
[156] A. Nadasen, T. Stevens, J. Farhat, J. Brusoe, P. Schwandt, J.S. Winfield, G. Yoo, N. Anantaraman, F.D. Becchetti, J. Brown, B. Hotz, J.W. Janecke, D. Roberts and R.E. Warner, Phys. Rev. C 47 (1993) 674.
[157] A. Nadasen, J. Brusoe, J. Farhat, T. Stevens, J. Williams, L. Nieman, J.S. Winfield, R.E. Warner, F.D. Becchetti, J.W. Janecke, T. Annakkage, J. Bajema, D. Roberts and H.S. Govinden, Phys. Rev. C 52 (1995) 1894.
[158] R.G. Newton, Scattering Theory of Waves and Particles (McGraw-Hill, New York, 1966).
[159] W.T.H. Van Oers and H. Haw, Phys. Lett. B 45 (1973) 227.
[160] J.C. Pacheco, B. Bilwes, F. Sanchez, J.A. Ruiz, J. Diaz, J.L. Ferrero and D. Kadi-Hanifi, Nucl. Phys. A 588 (1995) 537.
[161] F. Petrovich, H. McManus, V.A. Madsen and J. Atkinson, Phys. Rev. Lett. 22 (1969) 895.
[162] F. Petrovich, Microscopic Optical Potentials (Springer, Berlin, 1979) p. 155.
[163] J.C. Peng, R.M. DeVries and N.J. DiGiacomo, Phys. Lett. B 98 (1981) 244.
[164] C. Perrin, S. Kox, N. Longequeue, J.B. Viano, M. Buenerd, R. Cherkaoui, A.J. Cole, A. Gamp, J. Menet, R. Ost, R. Bertholet, C. Guet and J. Pinston, Phys. Rev. Lett. 49 (1982) 1905.
[165] I. Pecina, R. Anne, D. Bazin, C. Borcea, V. Borrel, F. Carstoiu, J.M. Corre, Z. Dlouhy, A. Fomitchev, D. Guillemaud-Mueller, H. Kellert, A. Kordyasz, M. Lewitowicz, S. Lukyanov, A.C. Mueller, Yu. Penionzhkevich, P. Roussel-Chomaz, M.G. Saint-Laurent, N. Skobelev, O. Sorlin and O. Tarasov, preprint GANIL P94-22.
[166] J.E. Poling, E. Norbeck and R.R. Carlson, Phys. Rev. C 13 (1976) 648.
[167] L.W. Put and A.M.J. Paans, Nucl. Phys. A 291 (1977) 93.
[168] C.L. Rao, M. Reeves and G.R. Satchler, Nucl. Phys. A 207 (1973) 182.
[169] S. Raman, C.B. Fulmer, M.L. Halbert, M.J. Saltmarsh, A.H. Snell and P.H. Stelson, Int. Conf. on Reactions Between Complex Nuclei, Nashville, TN, contributed papers (1974) 2.
[170] J. Raynal, Phys. Rev. C 23 (1981) 2571.
[171] R. Reid, Ann. Phys. 50 (1968) 411.
[172] M. Reeves, Microscopic analysis for elastic scattering of deuterons and alpha particles, Computer Technology Center (Oak Ridge) report CTC-32 (1970).
[173] W. Reilly, R. Wieland, A. Gobbi, M.W. Sachs and D.A. Bromley, Il Nuovo Cimento A 13 (1973) 897.
[174] N. Rowley, H. Doubre and C. Marty, Phys. Lett. B 69 (1977) 147.
[175] P. Roussel, N. Alamanos, F. Auger, J. Barrette, B. Berthier, B. Fernandez and L. Papineau, Phys. Rev. Lett. 54 (1985) 1779.
[176] P. Roussel, J. Barrette, F. Auger, B. Berthier, B. Fernandez, J. Gastebois, A. Gillibert, L. Papineau, W. Mittig, D. Disdier, B. Lott, V. Rauch, F. Scheibling, C. Stephan and L. Tassan-Got, Phys. Lett. B 185 (1987) 29.
[177] P. Roussel, N. Alamanos, F. Auger, J. Barrette, B. Berthier, B. Fernandez L. Papineau, H. Doubre and W. Mittig, Nucl. Phys. A 477 (1988) 345.
[178] G.R. Satchler and W.G. Love, Phys. Lett. B 65 (1976) 415.
[179] G.R. Satchler, Nucl. Phys. A 279 (1977) 493.
[180] D.A. Saloner and C. Toepffer, Nucl. Phys. A 283 (1977) 108.

[181] G.R. Satchler and W.G. Love, Phys. Rep. 55 (1979) 183.
[182] G.R. Satchler, Direct Nuclear Reactions (Oxford Univ. Press, Oxford, 1983).
[183] G.R. Satchler, C.B. Fulmer, R.L. Auble, J.B. Ball, F.E. Bertrand, K.A. Erb, E.E. Gross and D.C. Hensley, Phys. Lett. B 128 (1983) 147.
[184] G.R. Satchler, Nucl. Phys. A 409 (1983) 3c.
[185] Y. Sakuragi, M. Yahiro and M. Kamimura, Prog. Theor. Phys. Supp. 89 (1986) 136.
[186] C.-C. Sahm, T. Murakami, J.G. Cramer, A.J. Lazzarini, D.D. Leach, D.R. Tieger, R.A. Loveman, W.G. Lynch, M.B. Tsang and J. Van der Plicht, Phys. Rev. C 34 (1986) 2165.
[187] G.R. Satchler, Phys. Rep. 199 (1991) 147.
[188] G.R. Satchler, K.W. McVoy and M.S. Hussein, Nucl. Phys. A 522 (1991) 621.
[189] G.R. Satchler and W.G. Love, Phys. Rev. C 49 (1994) 2254.
[190] G.R. Satchler, Nucl. Phys. A 574 (1994) 575.
[191] G.R. Satchler and M.S. Hussein, Phys. Rev. C 49 (1994) 3350.
[192] P. Schwandt, S. Kailas, W.W. Jacobs, M.D. Kaitchuck, W. Ploughe and P.P. Singh, Phys. Rev. C 21 (1980) 1656.
[193] P. Schwandt, W.W. Jacobs, M.D. Kaitchuck, P.P. Singh, W.D. Ploughe, F.D. Bechetti and J.W. Jänecke, Phys. Rev. C 24 (1981) 1522.
[194] R.H. Siemssen, J.V. Maher, A. Weidinger and D.A. Bromley, Phys. Rev. Lett. 20 (1968) 175.
[195] D.K. Srivastava, Phys. Lett. B 122 (1983) 18.
[196] R.G. Stokstad, R.M. Wieland, G.R. Satchler, C.B. Fulmer, D.C. Hensley, S. Raman, L.D. Rickertsen, A.H. Snell and P.H. Stelson, Phys. Rev. C 20 (1979) 655.
[197] M.F. Steeden, J. Coopersmith, S.J. Cartwright, M.D. Cohler, N.M. Clarke and R.J. Griffiths, J. Phys. G 6 (1980) 501.
[198] E. Stiliaris, H.G. Bohlen, P. Fröbrich, B. Gebauer, D. Kolbert, W. von Oertzen, M. Wilpert and Th. Wilpert, Phys. Lett. B 223 (1989) 91.
[199] E. Stiliaris, H.G. Bohlen, P. Frobich, B. Gebauer, D. Kolbert, W. von Oertzen, M. Wilpert and Th. Wilpert, HMI Annual Report 1989, HMI-B-482 (1990) 50; the data appeared later in Ref. [19].
[200] Y. Sugiyama, Y. Tomita, H. Ikezoe, Y. Yamamuchi, K. Ideno, S. Hamada, T. Sugimitsu, M. Hijiya and Y. Kondō, Phys. Lett. B 312 (1993) 35.
[201] I. Tanihata, J. Phys. G 22 (1996) 157.
[202] I.J. Thompson, J.S. Al-Khalili, J.A. Tostevin and J.M. Bang, Phys. Rev. C 47 (1993) R1364.
[203] N. Vinh Mau and A. Boussy, Nucl. Phys. A 257 (1976) 189.
[204] N. Vinh Mau, Phys. Lett. B 71 (1977) 5.
[205] N. Vinh Mau, Nucl. Phys. A 457 (1986) 413.
[206] R.M. Wieland, R.G. Stokstad, G.R. Satchler and L.D. Rickertsen, Phys. Rev. Lett. 37 (1976) 1458.
[207] K. Yabana, Y. Ogawa and Y. Suzuki, Phys. Rev. C 45 (1992) 2909; Nucl. Phys. A 539 (1992) 295.
[208] M. Zahar, M. Belbot, J.J. Kolata, K. Lamkin, R. Thompson, J.H. Kelley, R.A. Kryger, D.J. Morrissey, N.A. Orr, B.M. Sherrill, J.S. Winfield, J.A. Winger and A.H. Wuosmaa, Phys. Rev. C 49 (1994) 1540.